Effects of a local topographic variation on confined, non-wetting droplets in a microfluidic channel

Margaux Kerdraon

THÈSE DE DOCTORAT

de l'Université de recherche Paris Sciences et Lettres
PSL Research University

Préparée à l'École Supérieure de Physique et de Chimie Industrielles de la Ville de Paris

Effects of a local topographic variation on confined, non-wetting droplets in a microfluidic channel.

Ecole doctorale n°391

SCIENCES MÉCANIQUES, ACOUSTIQUE, ELECTRONIQUE ROBOTIQUE DE PARIS

Spécialité Mécanique

Soutenue par Margaux KERDRAON
le 09 octobre 2018

Dirigée par **Marie-Caroline JULLIEN**
Et Stéphanie DESCROIX

COMPOSITION DU JURY :

M. Lequeux François
ESPCI (Paris), Président du jury

M. Dalnoki-Veress Kari
McMaster University, Rapporteur

M. Bodiguel Hugues
Liphy (Univ. Grenoble), Rapporteur

Mme Rio Emmanuelle
Paris Sud Orsay, Examinatrice

M. Bartolo Denis
ENS Lyon, Examinateur

Mme Jullien Marie-Caroline
ESPCI, Directrice de thèse

Mme Descroix Stéphanie
Institut Curie, Invitée

ESPCI PARIS

PSL RESEARCH UNIVERSITY PARIS

Contributions

On the droplet deformation study

Albane Théry contributed to the droplet deformation study during her internship. She successfully implemented the calculation of the droplet surface minimization and the time reconstruction of the droplet deformation. Lastly, she carried out all the Surface evolver simulations that are referred to in this chapter.

On the droplet relaxation study

Joshua D. McGraw contributed to the self-similar analysis of the interface profile of the droplet during the relaxation process and to the model.

Benjamin Dollet contributed to the model of the droplet relaxation within the Brinkman approximation and helped us to better understand the hydrodynamics in this study.

Aniello Linguori worked on the implementation of a laser to replace the resistances in the thermomechanical actuation. He showed that the droplet deformation could be induced by a laser similarly to the heating resistances. These results are not displayed in this report but will likely be the object of a publication.

Emilien Dilly worked on the model of the droplet deformation induced by both the Marangoni and the mechanical effects. His results helped us to better understand the contribution of both effects on the droplet.

Thomas Robert worked on the merging of droplets with the thermomechanical actuation that we never managed to prove experimentally. These results are not shown here.

Remerciements

Je remercie ...

- Kari Dalnoki-Veress, Hugues Bodiguel, François Lequeux, Emmanuelle Rio et Denis Bartolo pour la relecture de mon manuscrit et pour leurs commentaires pertinents et constructifs. L'attention qu'ils ont portée à mes travaux est une grande récompense,
- mes directrices de thèse, Marie-Caroline Jullien et Stéphanie Descroix, pour leur soutien, leur bienveillance et leur regard critique,
- Joshua McGraw pour sa grande pédagogie. Sa curiosité et sa rigueur scientifique m'ont guidée sur une bonne partie de ma thèse,
- Benjamin Dollet pour les échanges que nous avons eu, toujours très enrichissants,
- Albane, Emilien, Thomas et Aniello pour leurs multiples contributions. C'était très plaisant de travailler avec eux,
- Patrick Tabeling pour son accueil, son ouverture d'esprit et pour toutes les opportunités qu'il m'a offertes,
- Elizabeth Bouchaud pour sa générosité et sa culture. Pouvoir jouer dans son théâtre a été pour nous une immense chance,
- Guillaume, Oliver et Nawel pour leur patience et leur soutien technique.

Enfin, j'ai immensément apprécié évoluer aux côtés de Marc, Alex, Lorène, Pierre, Etienne, Hubert, Benjamin, Elian, Charles, Manon, Joshua, Gustavo, Ilham, Maria, Cécile et Marjan. Leur créativité, leur humour et leur bonne humeur contagieuse m'ont marquée pour la vie.

Avec une mention très spéciale pour Marine, évidemment...

Contents

Part I

Introduction

1 Motivations

This PhD work investigates the effects of confinement on the hydrodynamics of micrometric biphasic systems. *More precisely, this manuscript studies the response of a micrometric oil droplet in water, confined in a rectangular channel, to a variation of the channel topography.* We believe that this study indirectly finds applications in petroleum engineering and in droplet-based microfluidics that is thriving in biotechnologies.

Petroleum engineering

Petroleum engineering involves three steps of oil extraction [1]. The primary oil recovery step relies on the oil extraction out of the well bore as the result of the natural pressure in the reservoir. During this process, only 10 to 20 % of oil is extracted from the deposit. Then, petroleum engineers proceed to a second oil extraction step that involves the injection of water or steam to drive the oil out of the porous rock. After this second process, the average oil recovery rate is comprised in between 20 to 40 % [2]. Lastly, a third recovery step can be launched that involves the injection of chemical compounds like surfactants and polymers to match the viscosities of the water and oil - to decrease capillary instabilities and to improve the oil mobility - [3, 4]. This third step is very expensive and can only be developed if the market oil prize is sufficiently high to make the extraction of the last (~ 60 %) percent of oil that is trapped profitable. Given the significant loss of hydrocarbons that remain trapped in the deposit, the petroleum industry is eager to improve their understanding of the physical mechanisms that promote oil mobility in the porous media during these recovery phases. The present study may be of interest to understand specific mechanisms of oil mobility in the second step.

During this second phase, it is known that the interface between oil and water can destabilize due to the growing of capillary instabilities like viscous fingering [5, 6], to fragmentation [7, 8] or to gradients of confinement [9, 10, 11]. This destabilization results in the formation of a water/oil emulsions that has to flow through the confined porous media.

Droplet-based microfluidics

Emulsions flowing through pores of the same scale are also present in droplet-based microfluidics applications [12, 13]. The microfluidic field has thrived over the last decades with the promise of miniaturizing chemical and biological assays to reduce their costs and enhance their throughput [14, 15, 16]. Droplet-based microfluidics platforms are composed of a network of micrometric channels in which water-in-oil droplets are generated [11, 17, 18] and used as biochemical reactors, alternatively to microtitre plates [19]. These droplets constitute cargoes for reagants and can be driven to any location of the platform [20, 21, 22]. To trigger the biochemical assay, the droplets that contain the different components of the reaction, are forced to merge [23, 24]. In order to synchronize at best the biochemical reactions that are carried out in microfluidic devices, the droplets speed needs to be finely monitored [25], which requires to investigate the droplet mobility when the latter is confined in a pore/channel. Interestingly, microfluidic systems made of poly(dimethyl)siloxane or glass are often used as models to understand the flow of bi-phasic systems in porous media as these models are transparent. These ideal systems allow to link the emulsion flow pattern to external parameters (pressure drop, dispersed phase velocity, extracted liquid fraction...).

As a whole, understanding the mobility of two phase systems in micrometer size channels finds application in a wide range of domains from microfluidics applications up to oil recovery.

To understand the mobility of these emulsions through the pores of the media, many fundamental studies have developed ideal systems based on a complex network of channels [26] or on an isolated droplet that moves in a simply modelled-geometry: in a capillary tube [27] or in a Hele-Shaw cell [28, 29, 30]. To predict the mobility of the droplet, one has to consider the viscous dissipation that counters the pressure-driven motion. These studies prove that when the droplet is wetting, this viscous dissipation is localized near contact lines [31]. When the droplet is non-wetting, this viscous dissipation is localized near the dynamical meniscus that is defined as the transition region in the between the lubricating flat film and the spherical meniscus of the droplet [32]. Under some conditions, dissipation may also occur in the flat film [33]. The description of this viscous dissipation is complex and results from the balance between viscous stresses and surface tension, the viscous stresses being intrinsically dependent on the viscosity ratio in between both phases, the degree of confinement [10] and the boundary conditions at the interface [29].

All the ideal systems that are mentioned above (Hele-Shaw cells, capillary tube) do not capture the genuine geometry of the pores that droplets can encounter in a rocky soil or in a microfluidic device. In this manuscript, we want to take a step further

in the understanding of droplet mobility in tortuous porous media by investigating the dynamical response of an isolated confined droplet to a sudden change in the topography of an ideal microfluidic channel. We are interested in predicting the variation of the droplet shape and the dynamics of the droplet deformation. Our work is limited to the case of a droplet that is static in the channel. By "static", we mean that the droplet does not travel in the pore but can be deformed by the constraints exerted by the channel walls.

In the studied system, the channel topography is modified on demand with a reversible thermomechanical actuation [34]. The latter relies on the heating of a micropatterned resistance that induces a local dilation of the channel walls. A gradient of confinement is then imposed on the droplet such that the latter deforms on the length scale of the gradient and a reservoir of water is trapped in the vicinity of the resistance, see figure 1 for an illustration. This process is called the droplet deformation. When the resistance is switched off, the channel dilation disappears and the droplet relaxes to its initial plug-like shape. The reservoir of water drains towards the droplet extremities. This process is called the droplet relaxation.

2 General outline

This manuscript investigates the effects of confinement on a biphasic system through the relaxation of a droplet that is initially set out-of-equilibrium by a change in the channel topography. It is divided into four chapters:

1. The first chapter introduces general concepts on the hydrodynamics of biphasic systems and on the effect of confinement on these systems. In the next chapters, these concepts will be used to understand and to model our experimental observations.

2. The second chapter describes the experimental set-up and the thermo-mechanical actuation device. The thermal and the mechanical effects that are induced on the droplet as a result of the heating of a micropatterned resistance are experimentally characterized.

3. The third chapter demonstrates the effects of the local modification of the channel geometry induced by the thermo-mechanical device on the droplet. The experimental observations show that a localized tilt of only few degrees in the cavity, giving rise to a deformation of only 15 % of the channel height, can have striking effects on the deformation of the droplet and can even lead to break up. A model based on the surface minimization of the droplet, that takes into account the topography of the channel, manages to capture the deformed shape of the droplet and to predict its break-up. In addition, a power balance between the viscous dissipation and the capillary-driven motion recovers the dynamics of the droplet deformation. We show that our model can be reversibly used to extrapolate the topography of the channel.

4. The last chapter investigates the relaxation of a droplet that has been initially deformed by a local modification of the channel geometry. The droplet relaxation is driven by surface tension and is mediated by viscous dissipation. Interestingly, the dynamics of the droplet relaxation is very different from the one of the droplet deformation. A model based on scaling arguments that takes into account the sublinear viscous dissipation in the droplet menisci allows to capture the dynamical features of the droplet relaxation process. This last study evidences the critical contribution of the droplet menisci in such a confined geometry.

3 Overview of the characteristic variables of the studied system

In the majority of the experiments described in this work, a mineral oil droplet in water is confined in the rectangular channel of a microfluidic system. By "confined", we mean that the radius of the unconfined droplet at equilibrium, i.e. when the droplet takes a spherical shape at constant volume, would be much larger than any of the dimensions of the channel cross section. The channel walls are exposed to oxygen plasma, rendering the channel surface hydrophilic, such that the droplet is non-wetting [35]. It means that the droplet interface is always separated from the walls by a lubricating water film. A meniscus runs along the contour of the droplet, and gutters are formed at the four corners of the channel.

Figure 1 illustrates the droplet geometry and the typical experimental observations that we consider in this manuscript. The interface has a pocket-type profile composed of a reservoir followed by what could be considered as a thin film in the observation plane, and finally by the menisci at the droplet extremities.

The snapshots shown in figure 1b, illustrates an example of the droplet relaxation. The orders of magnitude of the dimensions that describe the system are

1. for the typical length, 10^{-5} to 10^{-4} m
2. for the typical velocity 10^{-5} m.s^{-1}
3. for the interfacial tension, 10^{-3} N.m^{-1}
4. for the viscosity, 10^{-3} Pa.s^{-1}
5. the viscosity ratio between the inner and the outer phase is 25.

Figure 1 defines the equatorial plane of the droplet, at $z = 0$, as the "in-plane" and shows a cross-sectional scheme of the droplet in the plane (y, z). Geometrical characteristics of the system are illustrated on the figure; h_∞ is the lubricating films thickness, $e/2$ is the radius of the droplet spherical menisci and δ is the typical size of the gutters. Lastly, the in-plane distance in between the droplet interface and the side channel wall is described by the function $h(x, t)$ in the reservoir.

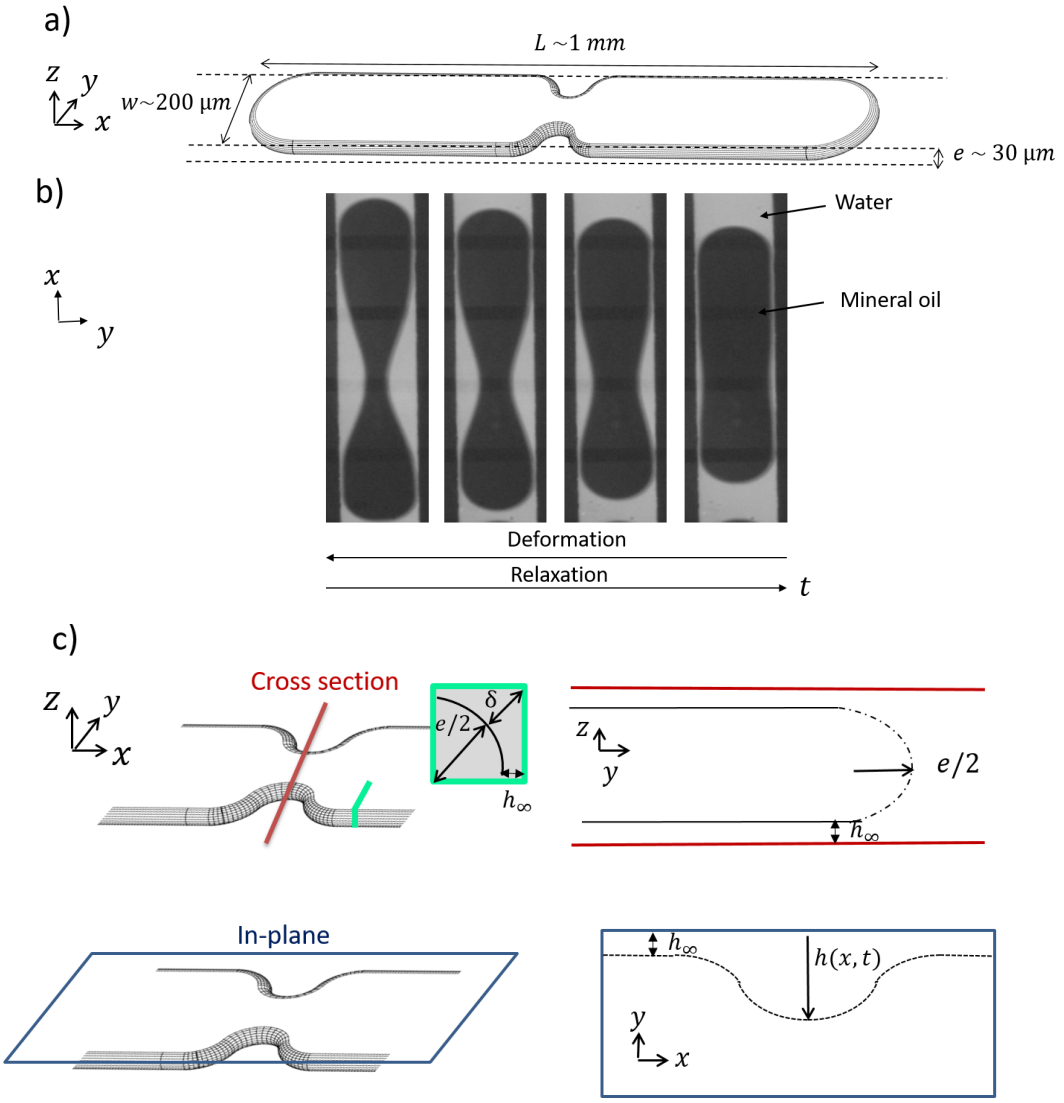

Figure 1: a) 3D shape of the droplet set out of equilibrium with typical orders of magnitude of the droplet and channel geometries. b) Snapshot of a droplet relaxation that is typically observed in the system. The observations are made in the equatorial plane ($z = 0$) for a frame of reference located at the center of the channel cross-section. c) Description of the geometry of the droplet in the rectangular channel in a cross-section plane (y, z) and in an equatorial plane $z = 0$ defined as the "in-plane". The radius of the droplet meniscus is $e/2$. The lubricating film thickness between the droplet and the wall is h_∞. The interface profile of the droplet in the "in-plane" is described by $h(x, t)$. δ is the typical size of the **gutters** at the fours corners of the channel.

4 Introduction to the physics of the studied biphasic system

The studied system, composed of an oil droplet in water, constitutes a biphasic system. In this section, we introduce some general features of the hydrodynamics of biphasic systems that build the background of the further interpretation of our experimental results.

4.1 Surface tension

4.1.1 Definition of the interfacial tension

A biphasic system is composed of two fluids 1 and 2 that are not miscible. In each of these fluids, an internal attractive force maintains the cohesion of molecules. At the interface between 1 and 2, the molecules of fluid 1 are partly surrounded by molecules of fluid 2 which means that they have lost some of their neighboring molecules (of fluid 1). As a result, the forces exerted by molecules 1 at the interface are no longer completely compensated by their neighbors. This absence of compensation is at the origin of the surface tension that makes the creation of an interface energetically unfavorable to the system. Indeed, a biphasic system always tends to minimize its interfacial area given the external constraints that apply on the system (ex: gravity, pressure, geometrical...). Without any of these constraints, the minimum interface that can be adopted by a dispersed phase is spheric [36, 37].

The work that is required to add an element of interface dA to a biphasic system, $\partial W = \gamma dA$, defines the value of the surface tension of the system γ. This value depends on the nature of the forces at play in the fluids (Van der Waals attractions, hydrogen bonds, etc.) [38]

Example: When oil is poured in a glass of water, mechanical work is added to the biphasic system and a emulsion composed of oil drops in water is formed (fig. 2a). However, this emulsion is not stable and leads to a separation of phases by a succession of droplet coalescence (fig. 2b). This final configuration minimizes the interfacial area between oil and water given the gravity that applies on the system and the value of the surface tension between both oil and water with the glass. Oil lays on top of water since it is the less dense phase.

a)  b) 

Figure 2: a) Emulsion of oil in water created by the mechanical energy added by the pouring process. b) Oil laying on top of water in a glass. Copyright @ https://chemistscorner.com.

4.1.2 Near a solid boundary: wetting and non-wetting properties

To determine if a drop of phase 1 surrounded by a fluid 2 wets or not on a solid surface, we compare the interfacial energy of the wall surrounded by fluid 1 to the interfacial energy of the wall surrounded by fluid 2. We define γ_{s1} as the surface tension between fluid 1 and the wall, γ_{s2} between the fluid 2 and the wall and γ_{12} as the surface tension between 1 and 2.

The spreading parameter defined as $S = \gamma_{s1} - \gamma_{s2} - \gamma_{12}$ compares these quantities. If $S > 0$, the liquid 2 wets the wall (configuration b, figure 4). On the other hand, if the S is negative, the presence of a film of phase 2 near the wall is more favorable and the droplet is non-wetting (configuration a, figure 4) [36].

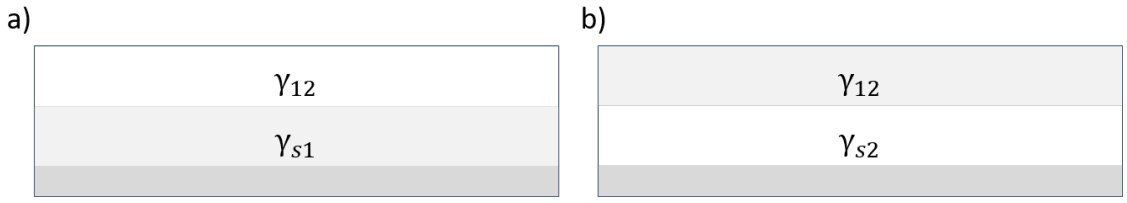

Figure 3: a) Fluid 1 wets the wall. b) Fluid 2 wets the wall.

4.1.3 Surface active agents

In order to stabilize an emulsion, surface active agents can be added to the external phase to stabilize droplets and prevent them from merging. This agent is called surfactant and is amphiphilic, see figure 4. The polar head of surfactants is more stable in the aqueous phases while its aliphatic tail (often made of CH2 radicals) has more affinity with oil phases. Surfactants adsorb at the interface between the two immiscible liquids. When they are adsorbed at the interface, the creation of new interfaces costs less energy [36]. Thus, surface tension decreases with the concentration of surfactants until it reaches the micellar concentration at which surfactant

molecules start to form gather in micelles [39, 40]. Beyond this point, surface tension remains constant as the surfactant concentration increases, see figure 4.

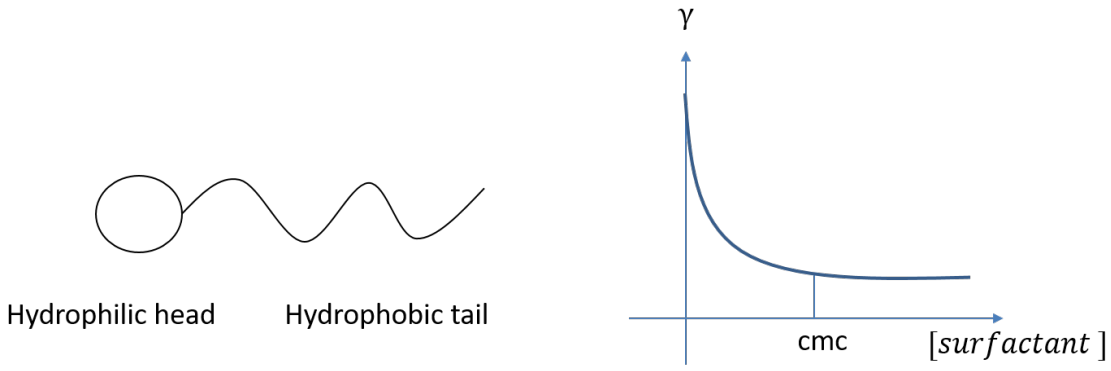

Figure 4: a) Surfactant configuration b) Typical evolution of the surface tension with the concentration of surfactants.

At rest, the stability and the thickness of the film separating two droplets interfaces is set by the disjoining pressure stemming from a combination of several repulsive or attractive potentials [38, 41]. In the DLVO theory the disjoining pressure is decomposed into structural (Π_s), van der Waals (Π_{VdW}), and electrostatic interactions (Π_{el}). When surfactants populate the droplets interfaces, the disjoining pressure increases in the films that separate them, playing mostly on the electrostatic repulsion [42]. The resulting exponential decay of the disjoining pressure with the film thickness leads to the existence of a stable film between the two interfaces. In section 6.2, we show that surfactants can also significantly affect the mobility of liquids near interfaces.

In the studied system

The surface active agent that is used is sodium dodecyl sulfate (SDS). SDS is an anionic molecule that is soluble in the external water phase. SDS is added to the system to prevent oil droplets from merging. In the majority of the experiments that are presented in this thesis, the concentration of SDS is set to a constant equal to $[SDS] = 2$ cmc$= 1.610^{-2}$ mol.L^{-1} at 25°C. The molecular structure of SDS is presented in figure 5.

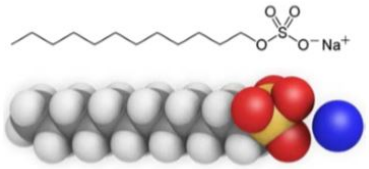

Figure 5: Sodium Dodecylsulfate structure.[43]

The surface tension in between mineral oil and water mixed with SDS at 2 cmc has been characterized and is equal to $\gamma = 11 \pm 1$ mN.m^1[44].

4.2 The Laplace pressure

Laplace has shown that the presence of an interface introduces a pressure drop that is proportional to the surface tension of the biphasic system and to the curvature of the interface. This pressure drop writes

$$\Delta P = \gamma \left(\frac{1}{R} + \frac{1}{R'} \right) = \gamma \mathcal{C} \tag{1}$$

where R and R' are defined as the radii of curvature of the interface in the two orthogonal planes normal to the interface. $\mathcal{C}$ is defined as the mean curvature of the interface [37].

In the absence of external constraints, an mean curvature or a surface tension that is not constant at a fluid/fluid interface can give rise to a surface stress along the interface. This surface stress induces "capillary-driven" flows that are critical in this study and that are described in the section 6.1.

5 The effects of confinement on the geometry of biphasic systems

When a non-wetting drop of radius R is squeezed in between two plates separated by a distance e, the drop adopts at equilibrium, a pancake-like shape. Park and

Homsy have shown that the mean curvature along the droplet interface is constant and verifies [6],[45]:

$$\mathcal{C} = \frac{2}{e} + \frac{\pi}{4R} \tag{2}$$

where R is the equatorial in-plane curvature of the squeezed droplet. The calculation of $\mathcal{C}$ that recovers this expression is complex and is not explained in this manuscript. If we consider that the radius of the droplet R is much larger that the cavity height e, the mean curvature simplifies as $\mathcal{C} \sim \frac{2}{e}$.

When the droplet is static in the cavity, the height of the flat film that is separating the non-wetting droplet from the walls can be calculated by balancing the capillary pressure in the droplet $P_{conf} \sim \frac{2\gamma}{e}$ with the disjoining pressure in the film that accounts for the molecular interactions (electrostatic, Van der Waals and steric) between the liquid/liquid interface and the solid boundary.

Figure 6 illustrates the evolution of the disjoining pressure as a function of the distance h between the two interfaces. The equation that balances the capillary pressure in the droplet with the disjoining pressure in the film $\Pi_{disj} \sim P_{conf}$ gives a stable solution for the height of the lubrication film h_∞. This height is typically tens of nanometers as observed by Huerre *et al.* with interferometric measurements [28].

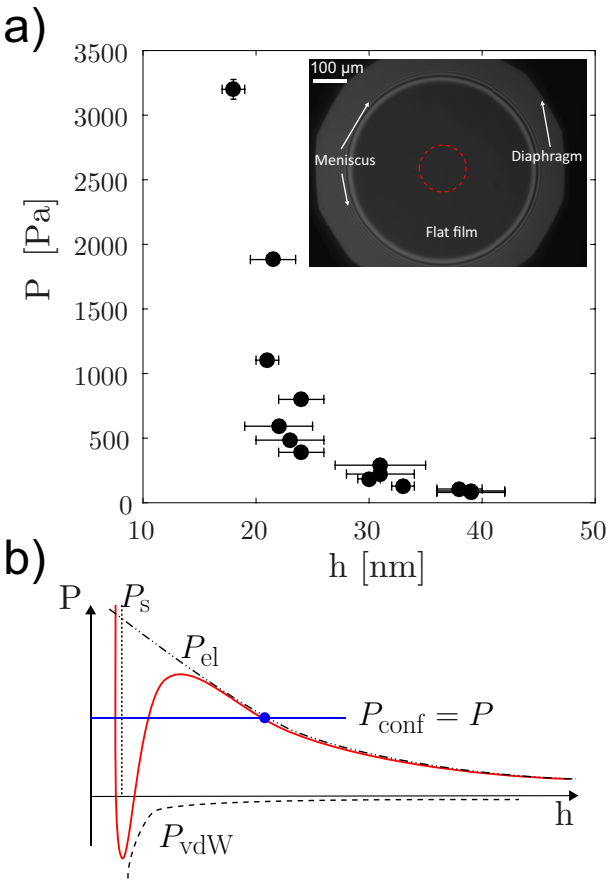

Figure 6: Evolution of the disjoining pressure $P = \Pi_{disj}$ with the thickness of the lubricating film: a) Experimental calibration of P as a function of h with interferometric measurements (see inset box) b) Typical evolution of the disjoining pressure that combines the electrostatic pressure P_{el}, the steric pressure PS and the Van der Waals pressure P_{VdW}. The solution for the film thickness results from the electrostatic contribution to the disjoining pressure [28]. The figure is adapted from [41]

In the studied system

In the rectangular cross-section of the channel, we distinguish the "free" surfaces from the "confined" surfaces. The first ones are not confined by a solid boundaries while the second ones are. The "confined" surfaces are typically at the level the lubricating films at the top and bottom interfaces of the droplet as well as the contact films at the side walls in the equatorial plane (the film is probably reduced to a line in this plane). The thickness of these lubricating films has been measured for a mineral oil droplet in water mixed with SDS at 2 cmc and is approximately 20 nm [41].
The "free" surfaces concern all the droplet menisci that are not confined by a wall. They are located in the gutters and at the extremities of the droplet. Near these menisci, the capillary pressure writes

$$P = \gamma \mathcal{C}, \tag{3}$$

the mean curvature of the droplet menisci being,

- at the extremities of the droplet,

$$\mathcal{C} = \frac{2}{w} + \frac{2}{e} \tag{4}$$

  where w is the channel width,

- in the gutters (see figure 1),

$$\mathcal{C} = \frac{2}{e} \tag{5}$$

When the droplet is deformed, its menisci at the level of the deformation (in the pocket region) is curved both in the (y, z) and in the (x, y) plane. We recall that, in this region, $h(x, t)$ defines the in-plane distance in between the droplet interface and the channel wall, see figure 1. Thus, the mean curvature of these menisci writes

$$\mathcal{C} = \frac{\partial_x^2 h}{\sqrt{1 + (\partial_x h)^{3/2}}} + \frac{2}{e}. \tag{6}$$

The term $\frac{\partial_x^2 h}{\sqrt{1+(\partial_x h)^{3/2}}}$ accounts for the curvature of the menisci in the plane (x, y) while the term $\frac{2}{e}$ accounts for the curvature of the menisci in the plane (y, z).

6 Hydrodynamics of biphasic systems

6.1 The Navier-Stokes equation

Our work deals with a biphasic system composed of incompressible newtonian liquids: water and mineral oil. Both phases can be described by the Navier-Stokes equation coupled to a boundary condition. This equation derives from the Newton's second law of motion applied to the dynamics of an element of fluid. Per unit of volume, the Navier-Stokes equation that describes the motion of fluids in each phase can be written as:

$$\rho\frac{\partial \mathbf{v}}{\partial t} + \rho(\mathbf{v}.\nabla)\mathbf{v} = \rho\mathbf{f} - \nabla p + \eta\nabla^{\mathbf{2}}\mathbf{v} \tag{7}$$

In this equation, ρ is the density of the liquid, $\mathbf{v}$ is the velocity field in the liquid, t is the time, p the pressure in the fluid, η the viscosity and $\mathbf{f}$ the external forces that apply on the liquid per unit of volume. We assume that fluids are incompressible so, by mass conservation, $\nabla.\mathbf{v} = 0$. Boundary counditions are required to solve this equation and to get the expression of the velocity field $\mathbf{v}(r,t)$. If we note σ the tensor of stresses at the interface, the boundary conditions write that

- the velocities projected normally to the interface are equal $\mathbf{v_o}.\mathbf{n} = \mathbf{v_w}.\mathbf{n}$
- the normal stresses at a curved liquid/liquid interface are discontinuous: $([\sigma]_w.\mathbf{n}).\mathbf{n} - ([\sigma]_o.\mathbf{n}).\mathbf{n} = \gamma\mathcal{C}$
- the tangential stresses at the interface are continuous: $([\sigma]_w.\mathbf{n}).\mathbf{t} = ([\sigma]_w.\mathbf{n}).\mathbf{t}$

where $\mathbf{n}$ is the vector normal to the interface and $\mathbf{t}$ is the vector tangential to the interface, $_w$ is the index for the water phase and $_o$ is the index for the oil phase. At the solid boundaries, we define a no-slip condition: $\mathbf{v} = 0$. The normal stresses at the interface are commonly the pressure and the tangential stresses are typically the viscous stresses.

Dimensionless parameters

From the Navier-Stokes equation, we can define typical forces that apply on a liquid element:

- the inertial forces deriving from the term $\rho(\mathbf{v}.\nabla)\mathbf{v}$ that is integrated over the volume of the fluid gives a force that scales as ρU^2R^2,
- similarly, the term $\eta\nabla^{\mathbf{2}}\mathbf{v}$ gives a viscous force that scales as ηUR,
- the term ∇p gives a capillary force that scales as γR, by considering only the Laplace pressure and

- the term $\rho \mathbf{f}$ times the volume of the liquid gives a volumic force like gravity that scales as gR^3.

To compare all these forces, dimensionless numbers are commonly used:

- the Weber number: $W_e = \frac{\rho U^2 R}{\gamma}$ that compares inertia to surface tension effects
- the Reynolds number: $R_e = \frac{\rho U R}{\eta}$ that compares inertia to viscous stresses
- the Bond number: $B_o = \frac{\rho g R^2}{\gamma}$ that compares gravity to capillarity
- the Capillary number: $C_a = \frac{\eta U}{\gamma}$ that compares viscous stresses to capillarity

Example:

As an illustration, if we consider a rain drop that is falling in the air, we can compare the orders of magnitude of these forces to extract the physical mechanisms that prevail in the drop motion. A snapshot of a raining drop during its fall has been captured by Villermaux *et al.* [46], see figure 7. On theses images, we observe that the 1 mm size drop adopts a large variety of shapes: from a coin to filaments to the burst in droplets. The water drop falls under the gravity force $\sim \rho g R^3$ while it is deformed by the drag force that scales as $\rho U^2 R^2$. During its fall, extreme deformation rates are achieved since capillary forces γR and viscous forces $\eta U R$ are weak compared to the inertial forces applied to millimeter-sized raindrops falling at several meter per second $W_e = \frac{\rho U^2 R}{\gamma} \sim 10^3 * 10^{-3} * 10^2 >> 1$ and $Re = \frac{\rho U R}{\eta} \sim 10^3 * 10^{-3} * 10^3 >> 1$.

Figure 7: Snapshot of falling raindrops captured by Villermaux *et al.* [46].

After the break-up process, droplets are much smaller ($R \downarrow$) such that $W_e \downarrow$ and $R_e \downarrow$. While droplets are getting smaller and smaller, viscous forces start to compete with inertial forces ($R_e \sim 1$). When viscous forces overcome inertia, droplets velocity obeys $\eta R U \sim \rho g R^3$. In this regime, Reyssat *et al.* [47] have observed that the diameter of droplets R is around 40 µm and the velocity U decreases down to hundreds of $\mu m.s^{-1}$. As a result, the capillary number that weighs viscous drag versus capillarity $Ca \sim \frac{\eta U}{\gamma} \sim 10^{-3} 10^{-5} 10^2 \sim 10^{-6}$ gets smaller than 1 and droplets are more spheric.

In the studied system

In order to estimate which effects prevail in our micro-system, we estimate the value of all the dimensionless numbers that are mentioned above. Knowing that in our experiments, the typical length is 10^{-5} m, the typical velocity is 10^{-5} m.s^{-1}, the surface tension equals to 10^{-2} N.m^{-1}, and the viscosity is at minimum 10^{-3} Pa.s^{-1}, we get:

- $W_e = \frac{\rho U^2 R}{\gamma} \sim \frac{10^3 10^{-10} 10^{-5}}{10^{-2}} \sim 10^{-10} << 1$
- $R_e = \frac{\rho U R}{\eta} \sim \frac{10^3 10^{-5} 10^{-5}}{10^{-3}} \sim 10^{-4} << 1$
- $B_o = \frac{\rho g R^2}{\gamma} \sim \frac{10^3 10 10^{-10}}{10^{-2}} \sim 10^{-4} << 1$
- $C_a = \frac{\eta U}{\gamma} \sim \frac{10^{-3} 10^{-5}}{10^{-2}} \sim 10^{-6} << 1.$

As a result, we deduce that inertia and gravity are overwhelmed by viscous effects and capillarity. The dimensionless number that is the most relevant for the system is thus the capillary number C_a.

Stokes approximation

When viscous and capillary effects prevail, the Navier-Stokes equation simplifies as:

$$0 = -\nabla p + \eta \mathbf{\Delta v}. \tag{8}$$

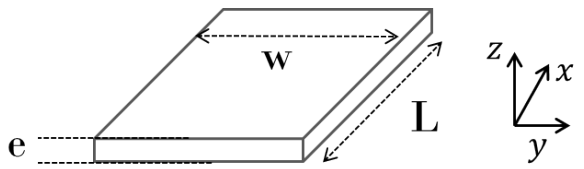

Figure 8: Scheme of a rectangular channel the dimensions of which are $w \times e \times L$

In our experiments, droplets are confined in the rectangular channel of a microfluidic system of dimensions $w \times e \times L$ where the cavity height e is much smaller than the typical lengths L and w over which fluids flow ($e <<\min(L, w)$).

Mass is conserved in the system such that the velocity field $\mathbf{v}$ verifies $\frac{\partial v_x}{\partial x} + \frac{\partial v_y}{\partial y} + \frac{\partial v_z}{\partial z} = 0$. Since the length scale in the direction of confinement z is small relatively to those in the $x - y$ plane, the component v_z is negligible: $v_z \sim e/\min(L, w) v_{x,y} << v_{x,y}$. Therefore, flows are considered as nearly parallel in the plane $x - y$.

In the Stokes equation, the viscous stress writes $\eta \Delta v$ where $\Delta v = \frac{\partial^2 v_{x,y}}{\partial x^2} + \frac{\partial^2 v_{x,y}}{\partial y^2} + \frac{\partial^2 v_{x,y}}{\partial z^2}$. Since $e <<\min(L, w)$, $\frac{v_{x,y}}{e^2} >> \frac{v_{x,y}}{L^2}$ and $\frac{v_{x,y}}{e^2} >> \frac{v_{x,y}}{w^2}$. Thus, the shear stress reduces to $\eta \frac{\partial^2 V}{\partial z^2}$.

After all these simplifications (called the lubrication approximation), the Stokes equation writes [37]

$$\eta \frac{\partial^2 v_{x,y}}{\partial z^2} = \nabla p. \tag{9}$$

As explained in the last section, the pressure gradient ∇p that prevails is the capillary pressure gradient in the x-direction that writes

$$\partial_x p = \gamma \frac{\partial}{\partial_x} \left(\frac{\partial_x^2 h}{\sqrt{1 + (\partial_x h)^{3/2}}} + \frac{2}{e} \right). \tag{10}$$

We assume that the typical scale of variation of h in the x-direction is L while h varies from 0 to w along the y-axis. Thus, $\partial_x h \sim w/L << 1$ and the capillary pressure gradient simplifies in the lubrication approximation as

$$\partial_x p \sim \gamma \partial_x^3 h. \tag{11}$$

To fully determine the velocity profile from the Stokes equation (9), the following boundary conditions

- $\mathbf{v} = 0$ if we consider no-slip at the channel walls
- $\eta_o \frac{\partial v^{(o)}}{\partial n} = \eta_w \frac{\partial v^{(w)}}{\partial n}$ at the droplet interface

are considered, where (o) identifies the oil phase and (w) the water phase.

6.2 Interfacial rheology

Up to now, we considered ideal interfaces as no stress is applied to them apart from the shear stress in both phases. However, a variation of surface tension can set a stress at the interface. For example, this variation can stem from a thermal gradient since surface tension is known to vary with temperature. If we consider the thermal gradient is set along the x-axis, the stress that is generated at the interface writes $\frac{d\gamma}{dx} = \frac{d\gamma}{dT}\frac{dT}{dx}$. This stress creates flows from low surface tension to high surface tension [48] and modifies the continuity of the viscous stresses at the interface as follows

$$\eta_o \frac{\partial v^{(o)}}{\partial n} - \eta_w \frac{\partial v^{(w)}}{\partial n} = \frac{d\gamma}{dx} \tag{12}$$

where (o) identifies the oil phase and (w) the water phase.

A variation of surface tension can also stem a gradient of concentration of the chemical compounds at the interface. For instance, a gradient of surface concentration of surfactants (Γ) sets a stress $\frac{d\gamma}{dx}$ that is equal to $\frac{d\gamma}{d\Gamma}\frac{d\Gamma}{dx}$. This gradient can occur when the interface is convected by pressure-driven flows in both phases. To estimate

the value of $\frac{d\Gamma}{dx}$, one has to compare the adsorption dynamics of surfactants to the interface with the typical convection time of the interface.

The behavior of surfactants at the interface relies on two mechanisms. First, surfactants diffuse through the bulk to reach the subsurface, which is the region near the interface. Then, the surfactants have to overcome an energetic barrier to adsorb to the interface [49]. If the time of desorption and adsorption of surfactants is smaller than the typical convection time of the interface figure 9a), we can consider that the surfactants are constantly exchanged between the interface and the bulk. In this case, the surface concentration of surfactants at the interface is constant. On the other hand, if the time of desorption of surfactants is much larger than the typical convection time of the interface figure 9b), surfactants are advected by the flow and end up being unevenly distributed at the interface. The resulting gradient of surfactants surface concentration $\frac{d\Gamma}{dx}$ creates a surface stress that counters the convection [50] and that rigifies the interface. This stress, known as the Gibbs-Marangoni stress, can significantly reduce the mean velocity of flows in both phases [51]. The behavior of surfactants typically depends on their solubility in both phases, from soluble, to poorly soluble up to non soluble for adsorption/desorption times that are much greater than the convection time [52]. In the two extreme cases, we say that the interface is "rigid" (insoluble case) or "mobile" (soluble case).

Remark:

The presence of surfactants at the interface can also induce a surface viscosity (both in dilatation and in shear). However, this viscosity is disregarded in our experiments since the surfactant that is used, SDS, is known to add almost no viscosity at interfaces [53].

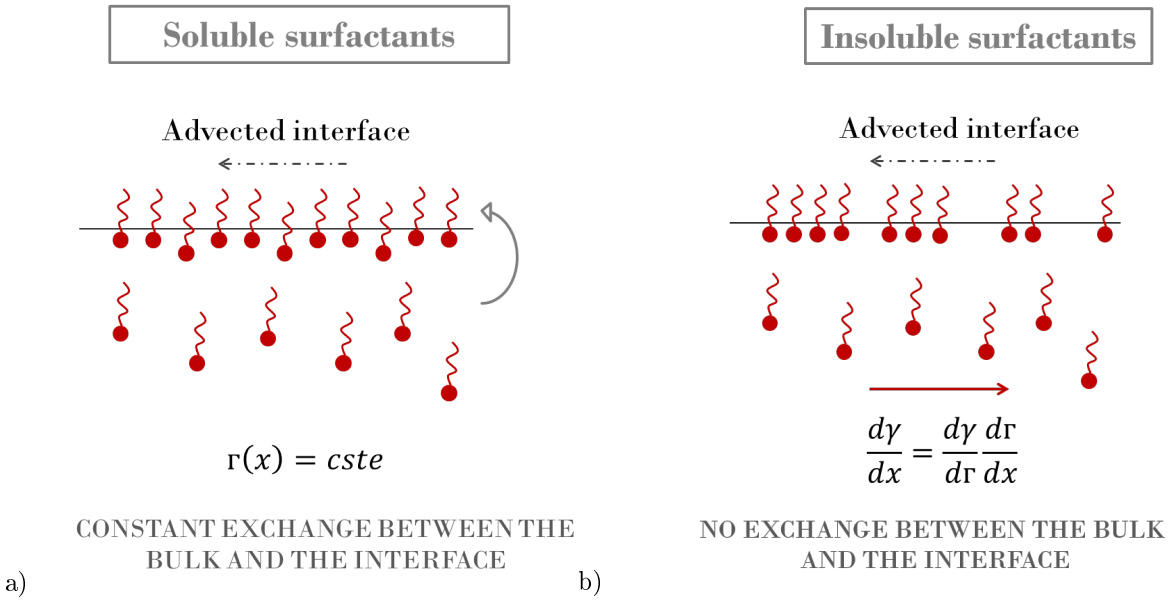

Figure 9: a) Scheme of the behavior of soluble surfactants at an advected interface. The quick ability of surfactants to populate and depopulate the interface allows to maintain a homogeneous concentration of agents at the interface. b) Extreme case of insoluble surfactants where the typical time of desorption is much larger than the time of convection of the surfactants along the interface. The unability of surfactants to desorb from the interface during its typical time of convection sets a gradient of surface tension at the interface.

In the studied system

The variation of surface tension can come from the gradient of temperature that is imposed in the channel and from a uneven distribution of surfactants at the interface:

$$\eta_o \frac{\partial v^{(o)}}{\partial n} - \eta_w \frac{\partial v^{(w)}}{\partial n} = \frac{d\gamma}{dT}\frac{dT}{dx} + \frac{d\gamma}{d\Gamma}\frac{d\Gamma}{dx} \tag{13}$$

SDS is an anionic surfactant soluble in water. Its adsorption/desorption typical timescale is around 1 ms which is much smaller than the typical convection time of flows in our experiments which is approximately $L/U \sim 10^{-3}10^{5} \sim 100$ s. That is why we consider that the interfaces are fully mobile in the studied system (Γ constant along the interface and no surface viscosity).

As a conclusion to this section, the tangential stresses at the interface writes

$$\eta_o \frac{\partial v^{(o)}}{\partial n} = \eta_w \frac{\partial v^{(w)}}{\partial n} \tag{14}$$

when no temperature gradient is imposed at the interface and

$$\eta_o \frac{\partial v^{(o)}}{\partial n} - \eta_w \frac{\partial v^{(w)}}{\partial n} = \frac{d\gamma}{dT}\frac{dT}{dx} \tag{15}$$

when a temperature gradient is imposed.

N.B. The effect of confinement on the continuity of viscous stresses at the interface is discussed in the following section (6.3).

6.3 Additional pressure gradient in the dynamical meniscus

In the previous sections, we wrote that the curvature of the droplet menisci in the plane (y, z) was constantly equal to $e/2$. This assumption implies that the curvature of the menisci is dominated by the Laplace pressure. However, Bretherton has shown that, when a meniscus is advancing or receding on a solid boundary, its curvature could be locally modified by the viscous friction in between the meniscus and the wall. More specifically, he has shown that, in the region that separates the lubrication film (I) from the droplet spherical meniscus (II), the viscous shear had to balance the capillary pressure gradient imposed by this variation of curvature, see figure 10, [32]. In this region (III), called the dynamical meniscus, the Stokes equation writes:

$$\eta_o \frac{\partial^2 v}{\partial_z^2} = \frac{\partial p}{\partial_y} \tag{16}$$

We note $H(y)$ the distance from the wall to the droplet interface such that in the lubrication approximation, the equation (16) verifies

$$\eta_o \frac{\partial^2 v}{\partial_z^2} = \gamma \partial_y^3 H \tag{17}$$

where $\gamma \partial_y^3 H$ is the capillary pressure gradient in the meniscus. Bretherton finds that, in the case of a confined non-wetting droplet, the viscous friction associated with the droplet motion on the wall is sublinear with the droplet velocity and scales as $C_a^{2/3}$.

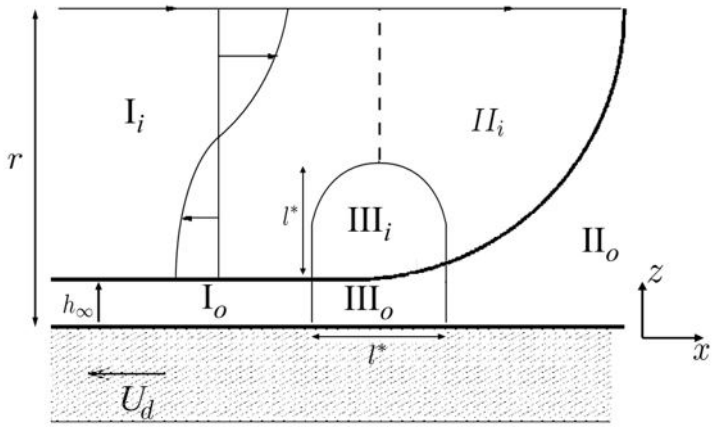

Figure 10: Scheme of the droplet meniscus confined near a solid boundary. Hodges *et al.* defines three regions: the spherical meniscus (II), the dynamical meniscus (III) and the flat film (I). The indexes $_o$ and i respectively describe the outer phase and the inner phase. The film thickness is noted h_∞ and l^* defines the horizontal extent of the lubrication film. In their study, it is the solid boundary that is pulled at a velocity U_d. r is the half-height of the cavity. The figure is extracted from [27].

In a review [33], Cantat estimates the numerical expression of the viscous force that prevails in the dynamical meniscus of a bubble, see the Appendix page 114. She shows that the force dependence on the capillary number varies with the boundary condition that is imposed on the liquid/liquid interface at the level of the dynamical meniscus.

1. <u>In the case of a stress-free condition</u>

   The stress-free condition neglects the viscous coupling in between the droplet phase and the outer phase. In this case, the interface is fully mobile and its velocity is set by the viscous dissipation in the outer phase. The boundary condition writes,

$$\eta_o \frac{\partial v}{\partial z} = 0 \tag{18}$$

Cantat finds that the viscous force per unit of length writes $f_{sf}^{f} = 3.84\gamma C_a^{2/3}$ if the meniscus is advancing and $f_{sf}^{r} = -1.1\gamma C_a^{2/3}$ if the meniscus is receding.

Provided that the interface is not rigidied by surface active agents, this condition is by definition true for a bubble/liquid interface since the viscosity of the bubble is negligible.

2. In the case of a rigid interface

   $\mathbf{v} = 0$ at the interface in the bubble frame. Cantat finds that the viscous forces per unit of length in the meniscus are $f_{sl}^{f} = 3.75\gamma C_a^{2/3} + 0.47\gamma C_a^{1/3}\frac{2l}{e}$ and $f_{sl}^{r} = -3.07\gamma C_a^{2/3} - 0.47\gamma C_a^{1/3}\frac{2l}{e}$,

   where $\frac{2}{e}$ is the radius of the meniscus in region II and l is the horizontal extent of the dynamical meniscus.

In order to determine the boundary condition that needs to be considered for the case of a water droplet in oil in the region of the dynamical meniscus, we can rely on the works of Hodges *et al.*[27]. They have shown that the boundary condition in that region depends mostly on the viscosity ratio between the inner phase and the outer phase $\lambda = \frac{\eta_o}{\eta_w}$ and the parameter $\epsilon \sim \frac{h_\infty}{e}$ that scales as $C_a^{2/3}$. Figure 11 recaps all the boundary conditions that can be encountered in the different regions of the droplet meniscus, depending on the experimental values of λ and ϵ.

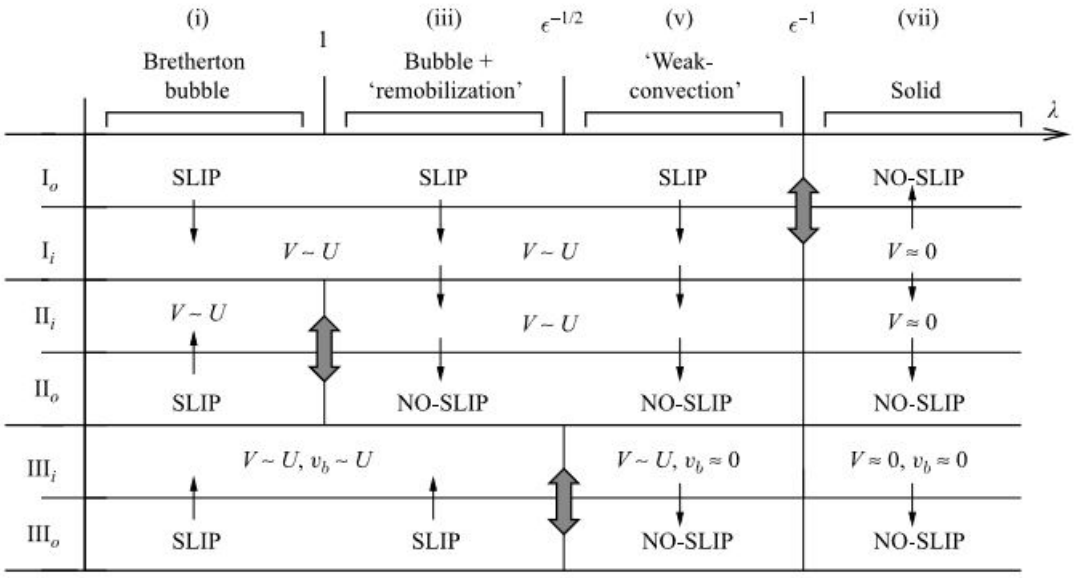

Figure 11: Table explaining the interface boundary condition in each region of the droplet as a function of λ and the parameter $\epsilon \sim C_a^{2/3}$. By SLIP, Hodges *et al.* mean that there is a stress-free condition at the interface. By NO-SLIP, they mean that the boundary velocity is set by the flow in the droplet. The figure is extracted from [27].

In the studied system, $\lambda = \frac{\eta_o}{\eta_w} = 25$ and $\epsilon \sim C_a^{2/3} \sim (10^{-6})^{2/3} \sim 10^{-4}$. Therefore, we have $1 << \lambda << \epsilon^{-1/2}$ and the boundary condition is stress-free in the dynamical mensicus (III_o) and in the film (I_o). In the plane (x, z), this condition writes

$$\eta_w \frac{\partial v^{(w)}}{\partial z} = 0 \tag{19}$$

In the spherical meniscus region of the droplet (II_o), the boundary condition is defined as 'No-Slip' and verifies

$$\eta_w \frac{\partial v^{(w)}}{\partial z} = \eta_o \frac{\partial v^{(o)}}{\partial z} \tag{20}$$

In this region, we can assume that the viscous shear lengthscale is approximately the same for the inner and the outer phase and scales as e, the channel height. However, the viscosity of the inner phase is 25 times more viscous than the outer phase. Therefore, the boundary condition writes

$$\eta_o \frac{\partial v^{(o)}}{\partial z} \approx 0 \tag{21}$$

In the experiments, we consider that the flow velocity in the droplet is almost zero such that $v = 0$ at the droplet interface in region (II).

Summary

We study the dynamical behavior of a mineral oil droplet in water mixed with SDS at 2 cmc. The droplet is confined in the rectangular channel of a microfluidic channel and does not wet the walls. Given the geometrical and the physico-chemical characteristics of the experimental system, the droplet behavior is governed by viscous and capillary effects.

In these conditions, the Stokes equation, written in the lubrication approximation, can be invoked to describe the velocity field in both phases. The motion of the droplet is induced by Laplace pressure gradients ($\approx \gamma \partial_x^3 h$) in the equatorial plane (x, y) and can in turn induce a capillary pressure gradient ($\approx \gamma \partial_z^3 H$) in the plane (y, z), along the droplet dynamical menisci (region III), that are moving normally to the flows. These regions concern mainly the pocket of the deformed droplet and the extremities of the droplet. In these dynamical menisci, the viscous force is sublinear with the outer phase velocity and scales as $C_a^{2/3}$, depending on the boundary conditions at the interface.

Based on the work of Hodges *et al.*, we consider that the boundary conditions that are required to solve the Stokes equation are:
- stress-free in the dynamical menisci of the droplet and in the lubricating films

$$\eta_w \frac{\partial v^{(w)}}{\partial n} = 0 \tag{22}$$

- $v = 0$ at the interfaces of the droplet spherical menisci (mainly in the gutters).

In the specific case in which a thermal gradient is imposed along the droplet interface, the boundary condition writes

$$\eta_o \frac{\partial v^{(o)}}{\partial n} - \eta_w \frac{\partial v^{(w)}}{\partial n} = \frac{d\gamma}{dT}\frac{dT}{dx} \tag{23}$$

We consider that there is no interfacial rheology induced by the presence of surfactants.

Part II

Materials and Methods - The thermomechanical actuation

Many techniques have already been developed in microfluidics to handle droplets based on a large variety of physical mechanisms: electrophoresis [54], magnetic field [55], acoustic field [56], marangoni effects [57, 58]. In this manuscript, we focus on an additional technique, called the *thermomechanical actuation*, that can propulse, stop, split, store and sort droplets. All these functionalities have been demonstrated few years ago by Miralles et al. [106]. In this manuscript, we use this technique to impose *a local variation* of the topography in the microfluidic channel and to study, in a more fundamental perspective, the response of a droplet to this topographic variation.

The thermomechanical actuation technique relies on the electrical actuation of *a micropatterned resistance* that locally heats the microfluidic channel by the Joule effect [48]. This chapter is dedicated to the description of the microfabrication of the thermomechanical device and to the characterization of the thermal effects that are induced on the droplets: *the thermal dilation of the channel walls* and *the increase of surface tension with temperature*.

7 Microfabrication of the thermomechanical device

Figure 12 illustrates the thermomechanical device. The latter is composed of a PDMS microfluidic chip [59] that is sealed on top of a glass substrate over which are patterned a network of micro-resistances, made of chromium and gold. A cross-section of the chip is schemed in figure 13.

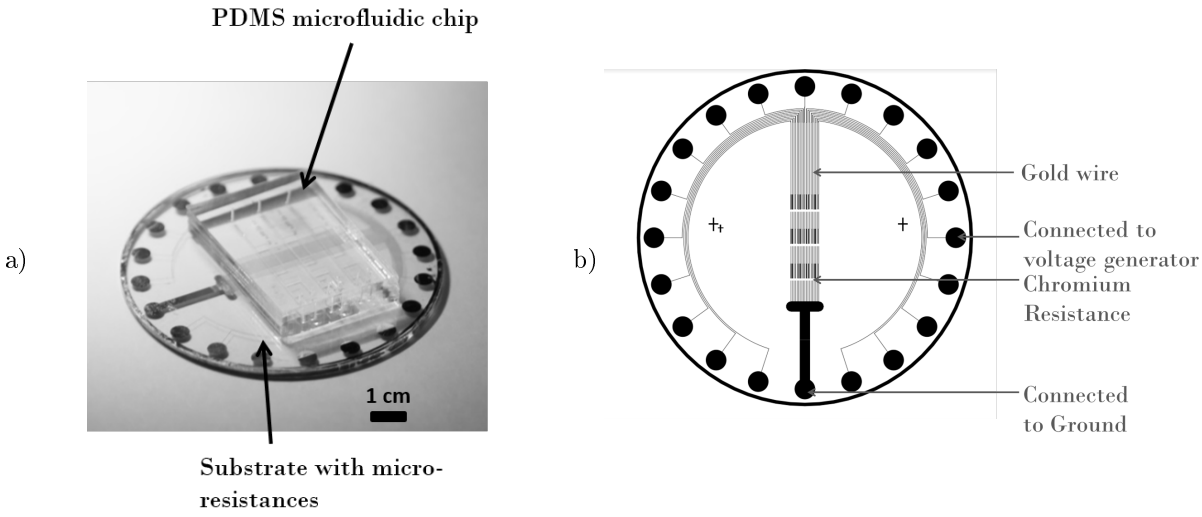

Figure 12: a) Image of the thermomechanical device composed of a PDMS chip on top of a glass substrate. b) Top view of the glass substrate on which are patterned the micro-resistances.

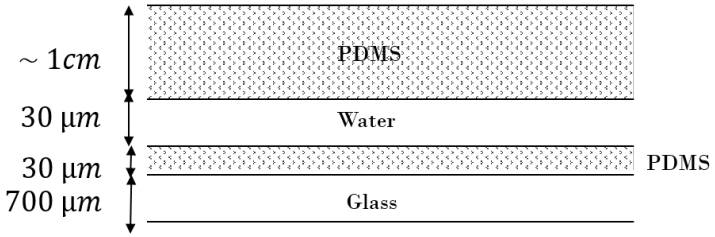

Figure 13: Scheme of a cross-section of the device with the different materials that are encountered: glass, PDMS, water (the channel), PDMS. The material height scales are not respected on the scheme.

7.1 The PDMS microfluidic chip

The microfluidic chip is made in a single block of poly(dimehtyl)siloxane (PDMS). The PDMS block is composed of polymer RTV-615 mixed with a crosslinker at a weight ratio 1/10. The crosslinker/polymer mixture is poured on a silicium wafer (soft-lithography technique [60]) over which the patterns of the microfluidic channels are designed in photoresist SU8 as the result of a photolithography process [61] (see figure 14). The mixture is cooked at 70 °C for 2 hours.

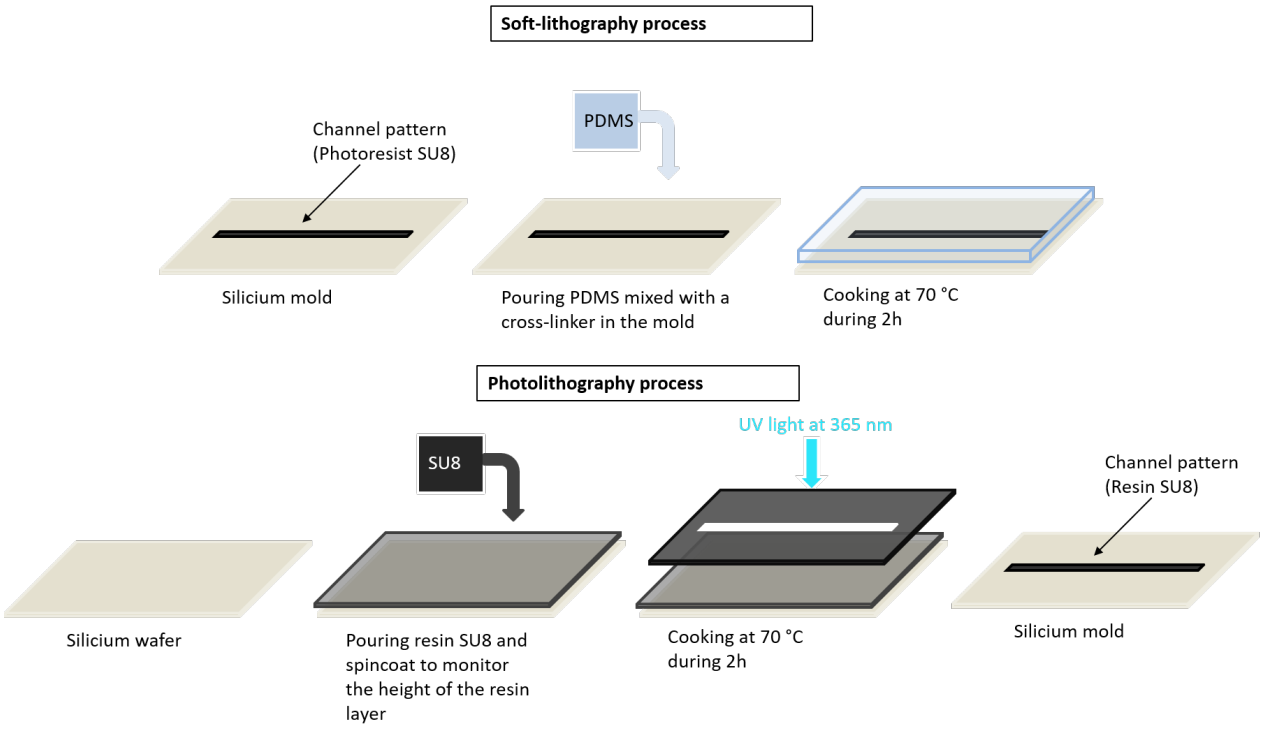

Figure 14: Soft-lithography process and photolihtography process.

7.2 Substrate with micro-resistances

The substrate is a 700 µm thick borosilicate glass wafer on which are deposited 15nm of chromium and 150 nm of gold. (ACM Grenoble). The two layers of metal are patterned with an etching process using S1818 photoresist [106]. Chromium patterns constitute the heating resistances and gold patterns serve as electrical connectors as their resistance is much smaller. The resistor width is 50 µm and its length is 400 µm. Its typical ohmic value is 300 ohm. The resistances are electrically isolated by spincoating a 30 µm thick layer of PDMS on top of the glass substrate.

1. First, the liquid PDMS at 1:10 is spincoated onto the substrate at 2500 rpm during 40s.
2. Then, the substrate is cooked in the oven at 70 ° C during 2h.

7.3 Assembly of the device and surface treatment

The microfluidic chip and the substrate are exposed to an oxygen plasma for 45 s such that -OH are created at their surface. When the two surfaces are put in contact few seconds after the oxygen plasma, they become bonded with covalent bondings (Si-O-Si). Water is injected in the microfluidic channel few minutes after the plasma exposition to ensure that the PDMS channel remains hydrophilic during the experiments [35].

8 Actuation of the thermomechanical device

External wires are connected to the resistances and to an external voltage generator. The device is illustrated on figure 15.

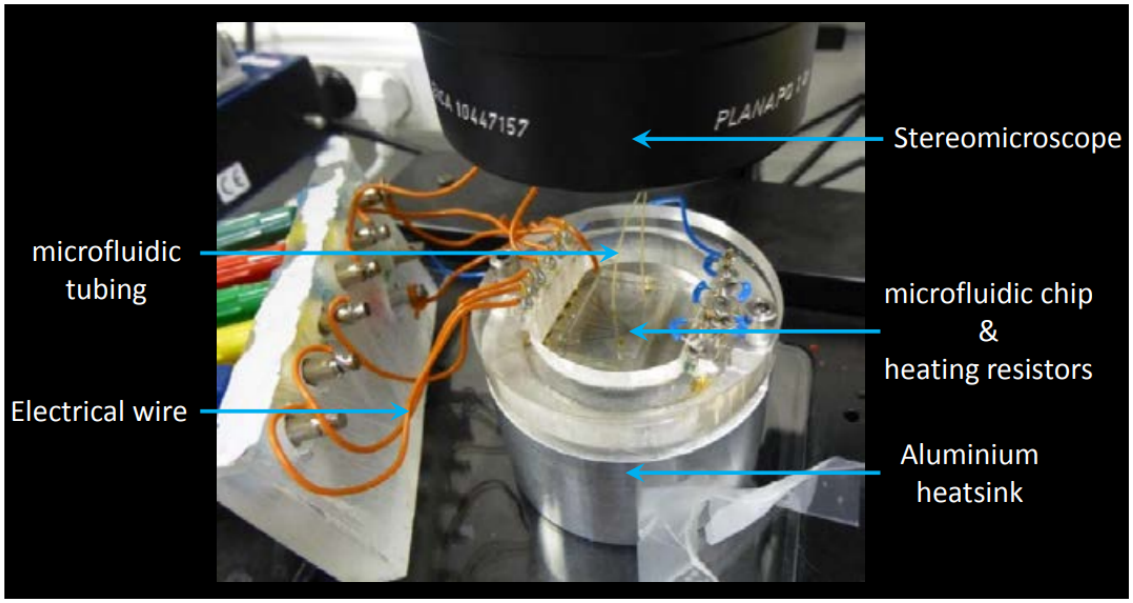

Figure 15: Image of the experimental set-up extracted from [106].

9 Observation set-up

The experimental cell is placed under a stereomicroscope (Leica MZ FLIII) that can illuminate the device with a white light source (Volpi Intralux 5100) and with a UV lamp (ebq 100) in reflection configuration. The droplet deformation is recorded with a CMOS camera (PixelLink PL-B781) at 15 Hz acquisition frame rate and is observed in the plane (x, y).

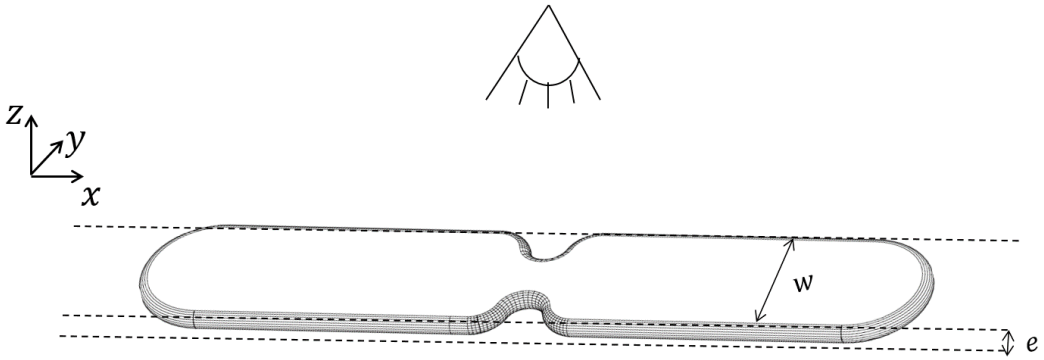

Figure 16: The droplet is experimentally observed in the plane (x, y).

10 Generation of mineral oil droplets in water

As mentioned in the introduction chapter, non-wetting, mineral oil droplets (Sigma Aldrich M5904) are generated in a solution of deionized water mixed with surfactants

(Sodium Dodecyl Sulfate : SDS, Sigma-Aldrich L4509) at 2.4 g.L^{-1}. The droplet production is achieved in a T-junction at the entrance of the microfluidic system, see figure 17a) [62, 63].

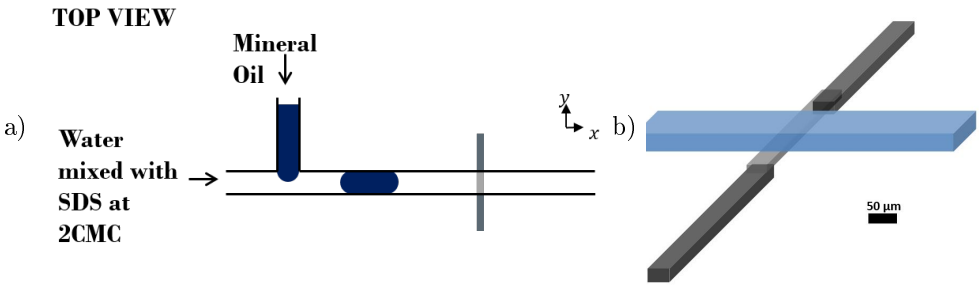

Figure 17: a) Scheme of the channel design composed of a T-junction that allows the generation of droplets. b) 3D view of the microfluidic channel that is aligned on the micro-patterned chromium resistance.

Remark:

Fluorescein is added to the water phase at 0.44 g.L^{-1}. Thus, when the droplet is illuminated by a UV lamp, all the field of observation appears black, except from the outer phase that appears green (with the eyes) or white (with the camera).

11 Temperature increase in the system

When a voltage is applied to the micro-patterned resistance, we measure a local temperature increase in the channel. This temperature increase has been characterized with an infrared camera (FLIR camera) that has a spatial resolution of 5 µm and a time resolution that is smaller than 100 ms, see figure 18.

The infrared camera captures the temperature ony at the surface of an object. In order to measure the temperature increase in the channel induced by the heating resistance, the temperature is captured on top of the sublayer of PDMS that is spincoated on the glass substrate.

To ensure that the temperature that is measured by the infrared camera comes only from the hot substrate and not from reflected IR waves of the ambient atmosphere, a painting (a black-body solution) is deposited on the substrate (Velvet black painting) that has an emissivity close to 1 [64]. Then, the temperature is captured at the surface of this thin layer of painting. In the following experiments, the room temperature is set to 26°C.

Spatio-temporal profile of the temperature gradient in the system

Figure 18a illustrates the temperature profile along the x-axis on one side of the hot resistance (located at $x = 0$) for electrical powers varying from 0 to 75 mW. Since the length of the resistance in the y-direction is larger than the typical width of the channel, the temperature is considered as homogeneous along the channel width.

Figure 18b illustrates the time evolution of the temperature in the channel when the resistance is successively switched on (at $t = 4.6$ s) and off (at $t = 18.5$ s), for a power equal to 50 mW. The typical timescales of the temperature increase and decrease in the channel are smaller than 500 ms. The typical time of our experiments being of few tens of seconds, we can consider that the temperature increase and decrease are instantaneous in the channel. After this transient time of at most 500 ms, the temperature remains constant in the channel as long as the resistance is on.

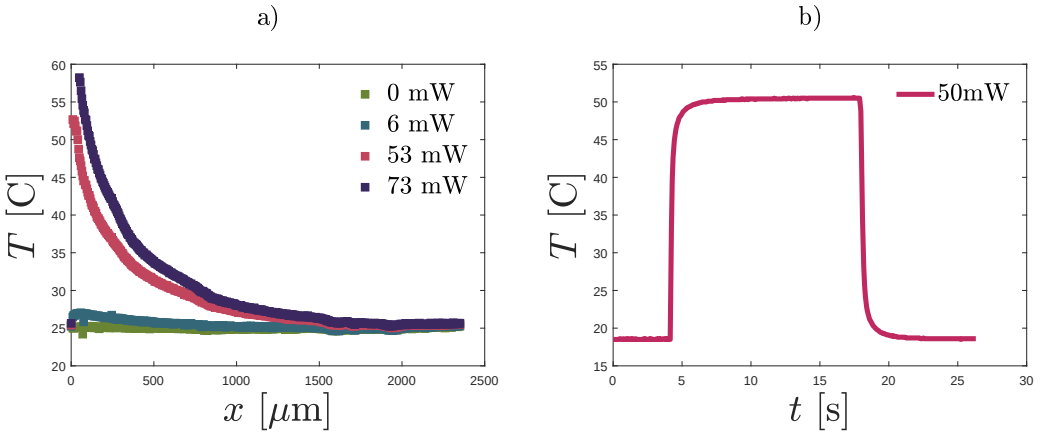

Figure 18: a) Spatial temperature profile measured with an infrared camera for $0 < P < 75$ mW along the x-axis. b)Temporal temperature profile for $P = 50$ mW. The resistance is switched on at $t = 4.6$ s and off at $t = 18.5$ s .

As suggests figure 18a, the spatial temperature profile is not linear. However, figure 19 shows thar we can extract some bounds for the temperature gradient : $8000 < \partial_x T < 16000$ K.m^{-1}. From now on, we consider that $\partial_x T$ is constant and is of the order of magnitude 10^4 K.m^{-1}.

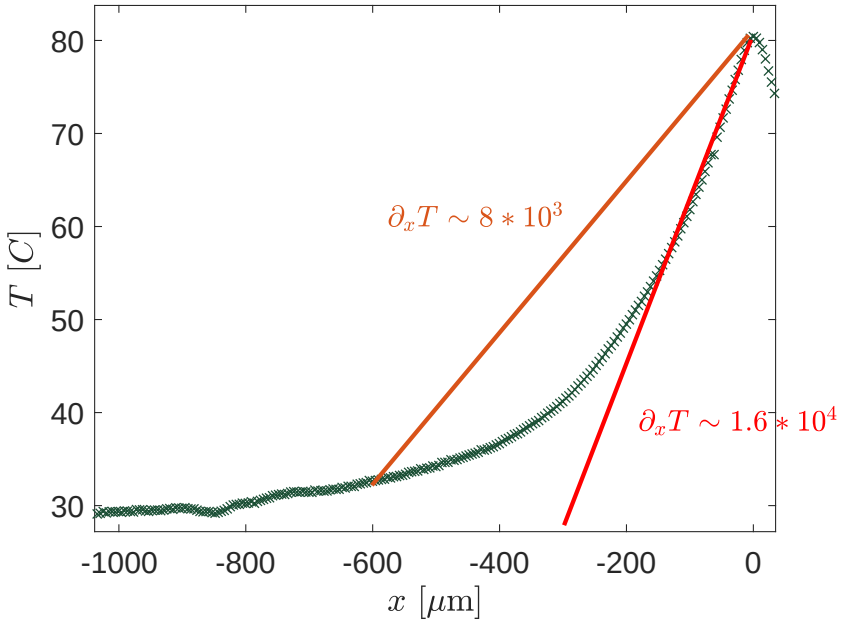

Figure 19: Spatial evolution of the temperature profile. Upper (red) and lower bound (orange) of the temperature gradient for $T = 80$ °C.

Thermal diffusion accross the channel height

The time of the thermal diffusion accross the channel height scales as $\tau_T = e^2/D$ where D is the thermal diffusion coefficient of mineral oil ($D = \kappa/(\rho C) \sim 0.1333/1900/870 \sim 10^{-7}$ m^2.s^{-1}), at room temperature [65]. We find that $\tau_T \sim 10^{-10}/10^{-7} \sim 10^{-3}$ s, which is much smaller than the typical time of our experiments (fews tens of seconds). Thus, even though the temperature has only been measured at the surface of the channel bottom wall, the latter can be considered as constant accross the channel height.

N.B. In this calculation, we provide the thermal diffusion coefficient of mineral oil at room temperature but we expect it to be a bit smaller at higher temperature. Therefore, the calculation $t_T \sim 10^{-3}$ s gives an upper bound for the thermal diffusion time accross the channel height.

Effect of a flow in the channel on the temperature profile

The temperature profile could be altered by flows in the channel. In the case of a uni-directional stationary flow along the x-axis of mean velocity V, the temperature would obey the advection-diffusion law that writes $V\partial_x T = D\partial_z^2 T$, z being the direction along which the dimension of the channel is the smallest.

To know if convection might alter the temperature gradient, we need to compare the time of the heat transfer induced by convection and the time of the heat transfer induced by diffusion. Thus, we define the Peclet Number: $P_e = \frac{t_{diff}}{t_{adv}} = \frac{Vl}{D}$.

In our experiments, we recall that

$V = 10$ µm.s^{-1}

$l = 1$ mm and

$D = 10^{-7}$ m^2.s^{-1} .

We find that $Pe \sim 10^{-1}$ which means that $t_{diff} << t_{adv}$ and that the heat transfer is dominated by diffusion. Therefore, the temperature gradient is not altered by the flows in the channel.

Variation of the temperature with the electrical power

From now on, the variable T describes the maximum temperature in the channel on top of the hot resistance, at $x = 0$. Figure 20 shows the linear evolution of T as a function of the electrical power in the system. The electrical power P that is applied at the edges of the resistance equals to $\frac{U^2}{R}$ where U is the voltage at the edges of the resistance and R its ohmic value. We find that within the range $0 < P < 100$ mW, the maximum temperature verifies $T = T_{amb} + \beta_T P$ where the ambient temperature, T_{amb}, is equal to 26°C and $\beta_T = 0.5$ °C.mW^{-1}.

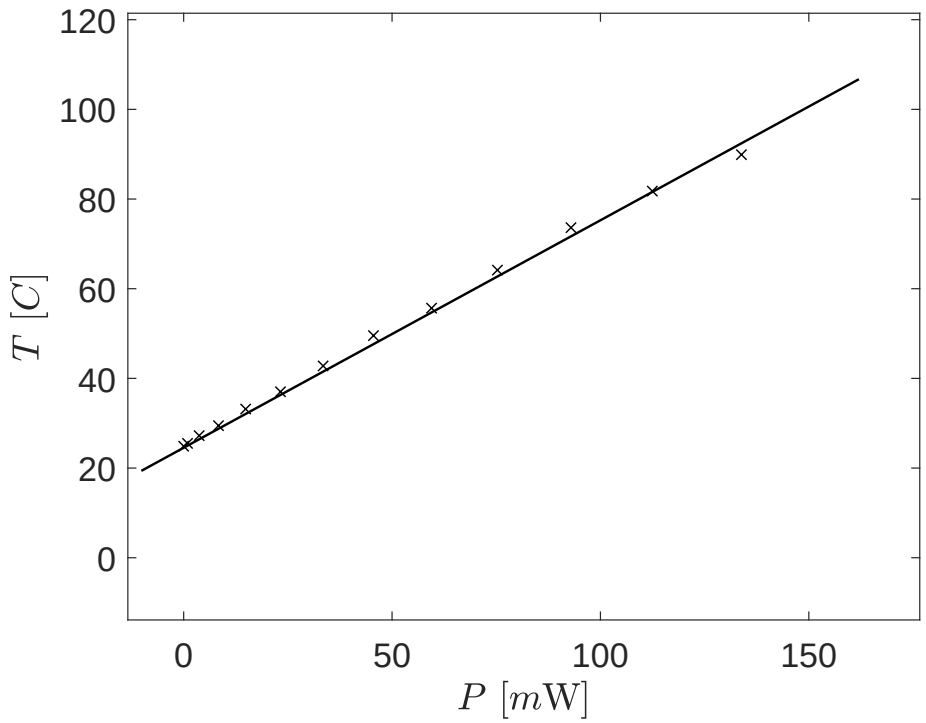

Figure 20: Evolution of T with the electrical power P that is applied at the edge of the micropatterned resistance.

12 Effect of the temperature on the channel topography

The thermal expansion of PDMS RTV-615 has been characterized in the literature and its coefficient of thermal expansion α_T is equal to $3 * 10^{-4} K^{-1}$ [66, 67]. In a (x, z) plane, we can estimate the maximum channel deformation, $\delta(z)$, that results from the temperature increase in the device. This deformation verifies $\delta(z) = \alpha_T h T$ where h is the initial height of the PDMS layer and T, the maximum temperature in the material.

- For the 30 µm thick PDMS sublayer at the bottom of the channel, we find that $\delta(z) = 30 * 10^{-6} * 3 * 10^{-4} * 80 \sim 0.1$ µm for $T = 80$ °C.
- For the block of PDMS on top of the channel, we find that $\delta(z) = 10^{-2} * 3 * 10^{-4} * 80 \sim 100$ µm, if we consider that this block is approximately 1 cm thick.

This would mean that the 30 µm high channel could be completely blocked at the level of the hot resistance. We do not observe such a deformation in our experiments, which might be explained by the fact that this calculation is very naive. Indeed, it assumes for example that the temperature is homogeneous across the 1 cm PDMS block which is unlikely true. In order to further characterize the thermal dilation of the channel walls, we carry out a direct experimental calibration.

12.1 *In-situ* characterization of the channel thermal dilation

Most methods used to measure deformations inside a sealed cavity are optical. Among them, we list:

- Fluorescence measurement using the linear relationship between the fluorescent solution layer thickness and intensity [68].
- Confocal microscopy, very convenient to measure topological shapes but its resolution of about 1 µm makes it unadapted to measure deformations of few µm [69].
- Refracted images of a pattern produced by a curved interface. Dangla et al. used this optical method to measure the swelling of micro-channels induced by alcane oils [70].

These methods turn out to be complex to implement to measure the thermal dilation of the channel walls *in-situ*. In the first method, fluorophores bleach with temperature and in the last method, multiple interfaces are curved along the light path and these interfaces might not be curved towards the same direction, which makes the analysis of the refracted patterns quite difficult.

Home-made method to measure the thermal dilation of the channel

To quantify the topological change induced by the thermal dilation of the channel walls, we designed a simple home-made system that we call the calibration step chip. This PDMS chip is composed a 200 µm wide channel that is 4, 5, 6 up to 15 µm high, with incremental steps of 1 µm, see fig. 21a. The chip is fabricated with a soft-lithography technique using a brass mold that has been milled with a micro-milling machine (the resolution of which is smaller than 100 nm).

The substrate on top of which is sealed the calibration chip is composed of a glass slide on which micro-resistances are patterned and a 30 µm thick layer of PDMS is spincoated - the substrate is similar to the one that is described in section 1. The channel is full of air ($n = 1$) to increase the refractive index difference in between the channel and the PDMS walls ($n = 1.42$).

When the channel dilates of d_z, the roof touches the bottom channel wall such that a contact line in between the two layers appears at step heights that are smaller or equal to d_z , see figure 21. By measuring the maximum height of the step at which the contact line is observed for a given temperature in the device, we can quantify the maximum deformation of the channel walls in the z-direction. The variation of this deformation as a function of the maximum temperature in the channel is illustrated in figure 22. The calibration measurements show that the channel deformation is comprised in between 0 µm and 10 µm. Unfortunately, the calibration step chip fails to quantify the horizontal extent of the confinement gradient that is established in the channel.

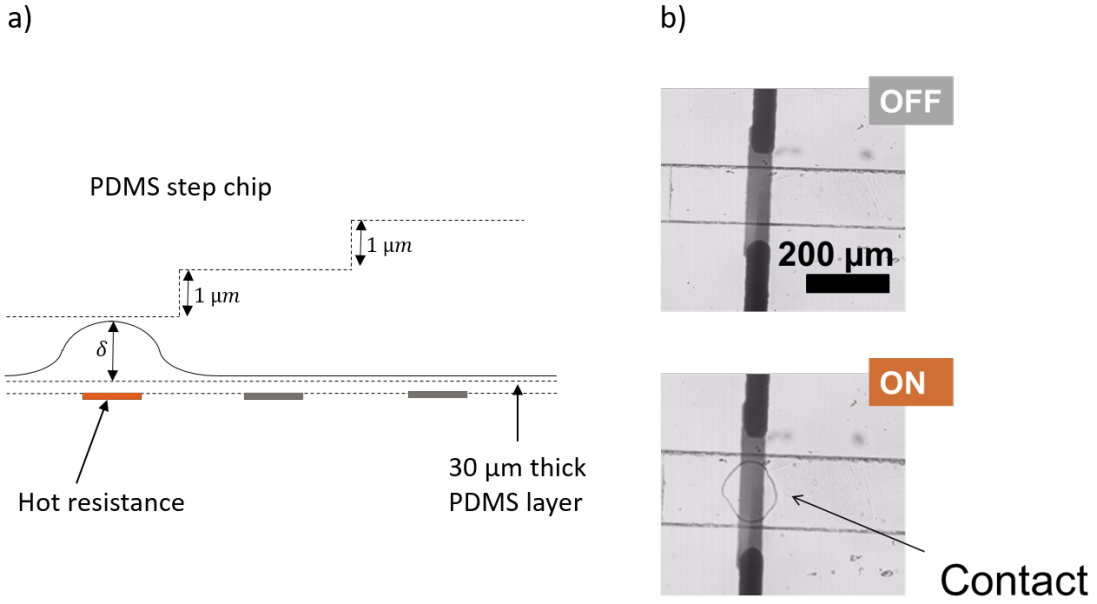

Figure 21: a) Scheme of the home-made calibration step device. The device contains steps in its roof to measure the dilation of micro-channels. The channel width is 200µm and its height is comprised in between 1 and 15 µm with steps of 1 µm. b) Typical observation that is made in the calibration chip. A contact line appears when the channel walls dilates such that the top wall touches the bottom wall.

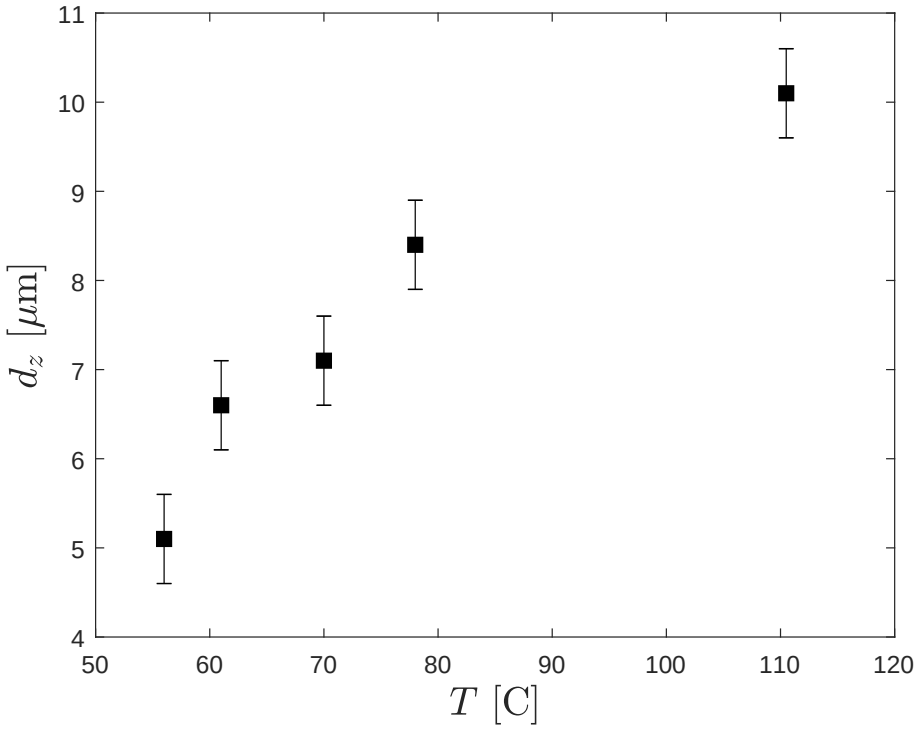

Figure 22: Height of the channel deformation versus the maximum temperature in the device, calibrated with the calibration step chip.

An interesting observation might help us to interpret the unexpected large dilation of PDMS

When the 30 µm thick sublayer of PDMS is not present in the chip, we do not observe any dilation of the channel, even at the smallest step heights. Oddly enough, we deduce that it is the PDMS sublayer that dilates the most in the channel. Contrary to the main PDMS block that constitutes the chip, the sublayer of PDMS is not degassed during the microfabrication process. Thus, some air bubbles might remain trapped in the thin layer of polymer such that the latter dilates largely when the temperature is increased in the channel. To validate this interpretation, the same calibration measurements should be carried out after having degassed the PDMS sublayer.

12.2 Mechanical profilometer measurements

In order to measure the horizontal extent of the channel dilation, we open the thermomechanical device to measure the topography of the bottom wall with a mechanical profilometer (Dektak 6M) when the resistance heats the device. The PDMS sublayer is stiffened by two glass slides that are separated by the typical width of the channel 200 µm [106].

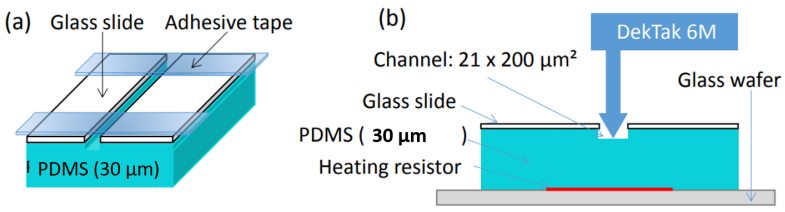

Figure 23: Scheme of the experimental set-up that is used to characterize a topographical change in the channel with a mechanical profilometer. This image is adapted from Miralles et al. [44]. The sublayer is stiffened by two glass slides that are separated by the typical width of the channel 200 µm to reproduce the experimental configuration of a closed channel.

The thermal dilation profile of the bottom channel wall is shown in figure 24. We observe that this deformation is comprised in between 500 nm to 2.5 µm for $30 < T < 80$ °C and that its horizontal extent is around 60 µm. Figure 25 illustrates the maximum deformation of the sublayer as a function of the maximum temperature in the channel. This deformation is approximately 4 times smaller than the one that has been measured with the calibration step chip. In the following, we only consider the values of d_z provided by the step chip that accounts for the dilation of all the channel walls and that has a geometrical configuration more similar to the experimental device.

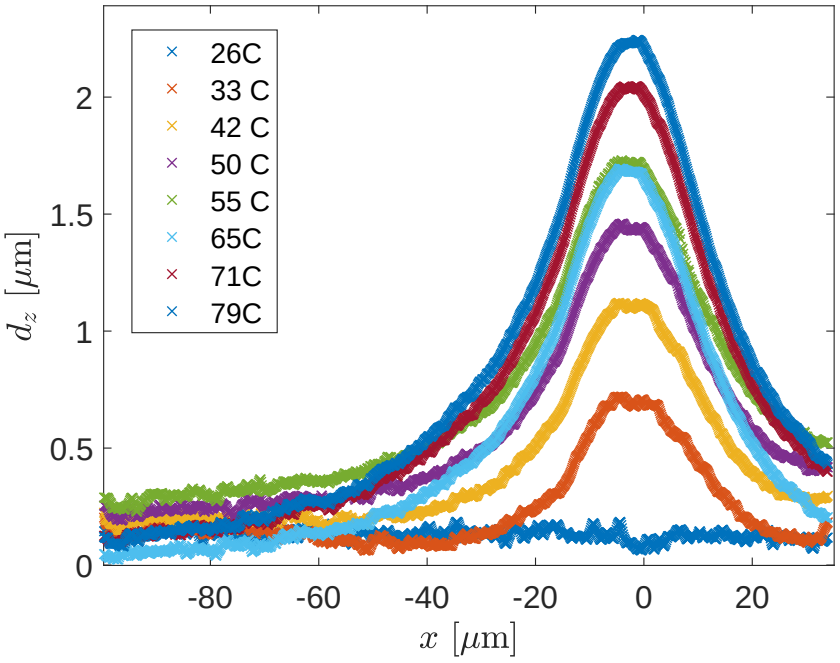

Figure 24: Spatial profile of the bottom layer of PDMS that is spin-coated on top of the resistance and stiffened by two glass slides. The profile is measured with a mechanical profilometer for different temperatures in the channel.

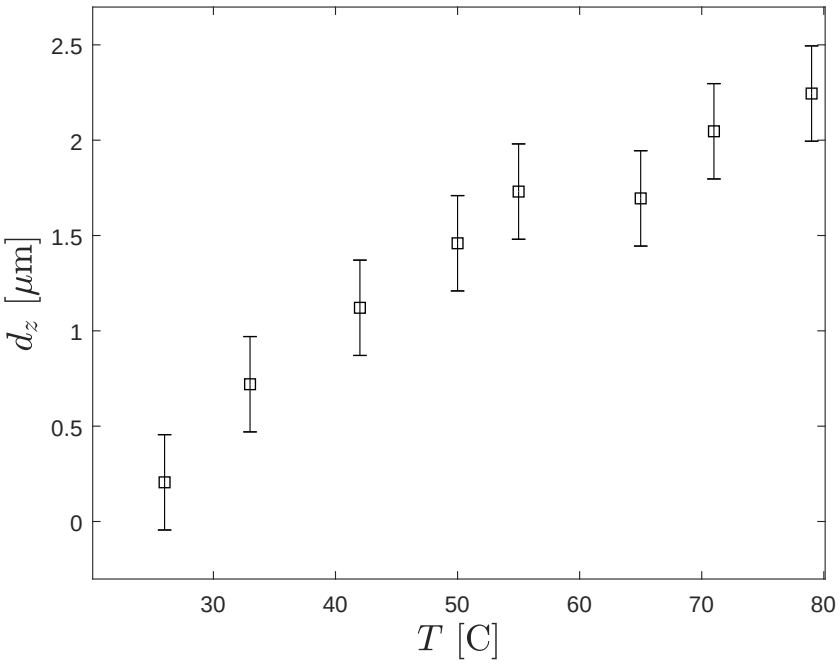

Figure 25: Maximum deformation the bottom layer of PDMS that is spin-coated on top of the resistance and stiffened by two glass slides separated by a distance of 200 µm. This deformation is measured with a mechanical profilometer as a function of the maximum temperature in the channel.

N.B. We measured the deformation profile of the sublayer of PDMS after a succession of cycles of temperature increase. We found the sublayer recovers a nearly flat surface

when the resistance is switched off. Therefore, we consider that the thermal dilation of the channel is reversible.

13 Effect of temperature on surface tension: the Marangoni effect

Surface tension is known to vary with temperature. The sign of $\frac{d\gamma}{dT}$ ($\partial_T\gamma$) depends on the liquids that are at play. In the case of mineral oil and water mixed with fluorescein and sodium dodecyl sulfate, we characterize the surface tension variation with temperature. We observe that surface tension increases with temperature. The gradient $\partial_T\gamma$ has been measured using the pendant drop method (KRÜSS) coupled with a thermal bath (JILABO), see figure 26. The software provided by Krüss measures the shape of the pendant droplet and extracts a surface tension by balancing the gravitational pressure with the Laplace pressure. For each temperature, a picture of the pendant droplet immersed in the thermal bath is taken at equilibrium and each of the images is associated with a surface tension [71].

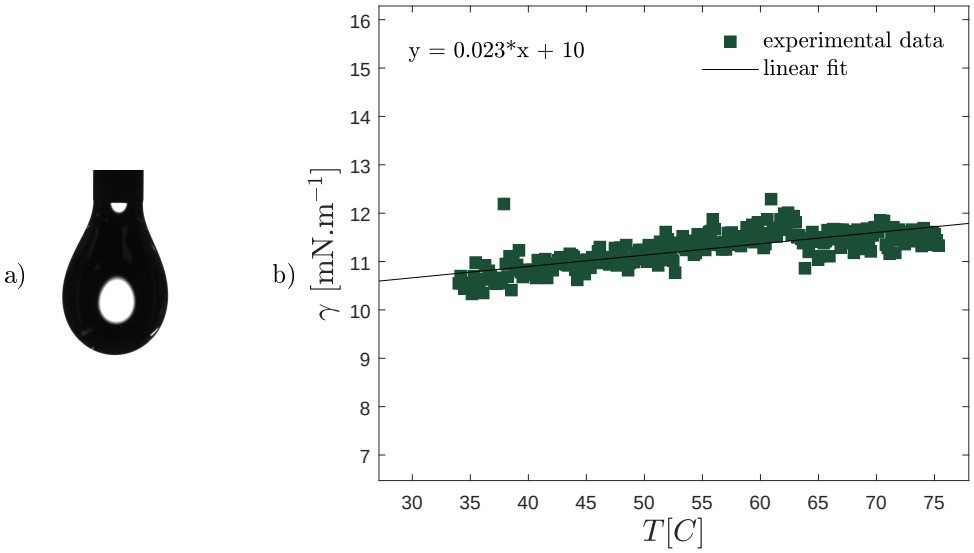

Figure 26: a) Image of a pendant drop b) Profile of the interfacial tension between mineral oil and water mixed for [SDS]=2 CMC.

We find that $\frac{d\gamma}{dT} = 2.3 * 10^{-5}$ N.m^{-1}.K^{-1}. Therefore, the stress that is imposed at the interface of the droplet in the vicinity of a hot resistance is equal to

$$\frac{d\gamma}{dx} = \frac{d\gamma}{dT}\frac{dT}{dx} \sim 2 * 10^{-5} * 10^4 \sim 0.2\text{Pa}. \tag{24}$$

Summary

We describe a technique based on a thermomechanical actuation that allows to change in a reversible way the topography of the channel. This actuation is based on the heating of a micropatterned resistance that establishes a gradient of temperature of around 10^4 K.m^1 on the lengthscale of the droplet. This temperature gradient has two effects on the droplet:

1. it imposes a Marangoni stress at the droplet interface.

   The value of the stress is $\frac{d\gamma}{dx} = \frac{d\gamma}{dT}\frac{dT}{dx} \sim 2 * 10^{-5} * 10^4 \sim 0.2$ N.m^{-2} (P$_a$)

   when the resistance heats at 80 °C ($P = 130$ mW).

2. it induces a change of the channel topography because of the thermal expansion of the latter.

   The maximum dilation that is observed in the channel has been characterized *in-situ* and seems to be bounded in between 5 µm and 10 µm for electrical powers varying from 50 mW to 110 mW.

Part III

Droplet deformation

In this chapter, we focus on the droplet deformation induced by a local variation of the channel topography. This topographic variation is induced by the thermal dilation of the channel walls. The temperature increase that creates this dilation stems from the heating of a micro-resistance that is located below the microfluidic system, see section Materials and Methods for more details.

We observe that when a droplet is located on top of the heating micro-resistance, it deforms until it can even break. Several thermal effects could account for the droplet deformation. Indeed, beyond the confinement gradient that is imposed on the droplet because of the channel dilation, a surface tension gradient sets along the droplet interface that provokes a Marangoni flow in both phases towards the hot regions where the surface tension is higher for the working liquids.

To discriminate the relative contribution of the Marangoni effect and of the confinement gradient effect on the experimental droplet deformation, a "mechanical" device has been designed to mimic the topographical variation that is induced by the thermal channel wall dilation without any temperature increase. The confinement gradient is indented in the channel during the microfabrication process. By comparing the droplet deformation that is achieved in this "mechanical" device with the one that is observed in the "thermomechanical" device, we are able to show that the thermal Marangoni contribution to the droplet deformation process is negligible. Thus, the droplet deformation is mainly due to the local variation of the channel topography. We show that a variation of only 15 % of the channel height can induce the droplet deformation and even its break-up.

The droplet deformation is driven by a capillary motion and is mediated by viscous dissipation. To model the deformation mechanism, we calculate the minimum surface energy of the droplet given the geometric constraints that are imposed in the channel. Then, we couple this calculation to a power balance between the viscous dissipation power and the increased surface excess energy of the droplet per unit of time that manages to recover the main features of the dynamics of the droplet deformation.

14 State-of-the-art on the droplet break-up

Droplet break-up is a basic functionality that is required in emulsion science for droplet production. The break-up mechanism has been extensively studied in the literature. In 1873, Plateau showed that droplets of controlled volume can be produced as the result of the destabilization of a liquid thread; this instability is now known as the Rayleigh-Plateau instability. Since the pioneering study of Taylor on the droplet deformation induced by an extensional flow, break-up has also been investigated in a large variety of flow and geometrical configurations.

When droplets are placed in shear flows [72] or in extensional flows [73, 74], they deform until they are sufficiently elongated to allow the growth of capillary instabilities (Rayleigh-Plateau instability). In these flow conditions, it has been demonstrated that droplet breakup occurs when the capillary number exceeds a certain threshold value C_a^*. This value varies non-monotonically with the viscosity ratio in the biphasic system, λ [75]. The confinement also plays a crucial role in these elongation-mediated breakups, [76], see Varanoye et al. 2006 for a review. For instance, Guillot *et al.* have proved that the growth of capillary instabilities could be prevented in confined geometries [77, 78].

Since the flow conditions that are required to induce droplet break-up depend on many parameters (shear or extensional flow, viscoity ratio and confinement), active techniques have been developed to break droplets on demand using, for instance, an electrical field [79] or an acoustic field [56]. The electrical field imposes a Lorentz force on the droplet that is polarized as a dipole. It results in the elongation of the droplet until the latter breaks. The acoustic field deforms the droplet interface under the effect of the radiation pressure.

In parallel, some researchers have designed complex geometric microfluidic configurations to break up droplets with a fairly high throughput: T-junction [80, 62, 81, 82, 83], cross-flow channels [84], obstacles [7], step channels [85]. In T-junction geometries or in cross-flow channels, that are very often used in microfluidic devices, breakup also occurs when the capillary number is higher than a threshold value C_a^*. In addition, the breakup criteria depends on the geometrical parameters of the system like the initial length of the droplet and the width of the inlet channel [82].

In the step emulsification, the liquid thread destabilizes when it reaches a step change in the cavity height or when it undergoes a confinement gradient [85, 45]. In this case, the radius of the droplets that are produced depends on the confinement gradient and on the initial height of the cavity. In the step-emulsification process, the thread is injected at a constant flow-rate Q in a stepped cavity. The initial height of the thread is h_0 while $h_0 + \Delta h$ is defined as the height of the output cavity. This process results in the production of controlled volume droplets, the radius of which

is h_0 when $\Delta h > h$. A variation of this technique consists of injecting the thread into a large cavity where the top wall is tilted with an angle α that is comprised between 0.5°and 4.5°. Dangla et al. [45] discuss the criteria of break-up of this system and predict that the radius of the droplets that are produced verifies

$$R^* = 0.44\sqrt{1 + 0.2\sqrt{\tan(\alpha)}\frac{w}{h_0}}\frac{h_0}{\sqrt{\tan(\alpha)}}. \tag{25}$$

Our study relies on an additional technique to achieve droplet break-up. This technique -so far called the thermomechanical actuation- has been already developed by [34, 44]. In this work, we propose a theoretical framework to predict the droplet deformation and break-up achieved with this thermomechanical device.

15 Experimental observations

We observe that when the droplet is located on top of a hot resistance, a neck forms at its center. The droplet deforms in the equatorial plane (in-plane) like a peanut (fig. 27). By mass conservation, the outer phase (water) is pulled towards the center of the droplet to occupy the volume that is released by the formation of the neck. In the meantime, the volume of oil is conserved such that the droplet extremities move slowly away from the resistance.

In order to describe the droplet deformation, several parameters are considered: the droplet length $L(t)$, the neck extension in the y-axis and the neck extension in the x-axis. We define $h(x,t)$ as the in-plane distance in between the channel wall and the droplet interface. The maximum value of this distance which by definition occurs at x=0, on top of the heating resistance, is noted $h_0(t)$. Thus, the neck extension in the y-axis writes $w - 2h_0(t)$ where w is the channel width. The neck extension in the x-axis is defined as $b(t)$. By volume conservation, we should be able to relate the neck extension to the droplet elongation. In the following sections, we decide to describe the droplet deformation through the spatio-temporal evolution of the neck instead of the droplet length.

Gutters are located at the four corners of the channel. The typical size of these gutters, schematically indicated in the green-boxed inset in figure 27b, scales linearly with the channel height e. The length of these gutters is noted L_g. All these notations are illustrated in Figure 27.

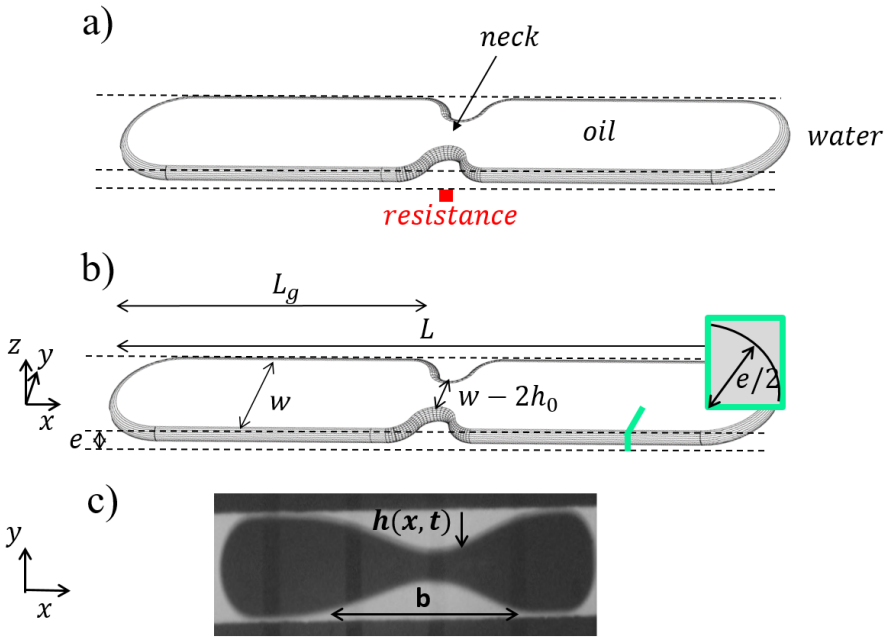

Figure 27: a) 3D scheme of the non-wetting mineral oil droplet surrounded by water confined in a rectangular microfluidic channel. The neck is defined as the spatial region in which the droplet interface deforms. This region is located in the vicinity of the resistance. b) Geometrical parameters of the system. Gutters are located at the four corners of the channel. The typical size of these gutters, schematically indicated in the green-boxed inset, scales linearly with the channel height e. c) Typical droplet deformation captured with a camera in a top view plane (x, y). The interface profile of the droplet is described by $h(x,t)$, the horizontal extent of the neck region is defined by b.

When the resistance is switched on, the droplet deforms until it can either reach an equilibrium shape (figure 29) or break into two (figure 28). The fate of the droplet depends on the temperature increase that is induced in the system. Beyond a certain critical value of the temperature increase T^*, the droplet deforms until its neck width gets smaller than the channel height ($w - 2h_0(t) = e$) and the droplet breaks. Snapshots illustrate the droplet break-up process in figure 28. The break-up criteria $w - 2h_0(t) = e$ is discussed further in this chapter.

If the temperature increase in the channel is smaller than the critical temperature, $T < T^*$, the droplet deforms until it reaches an equilibrium shape. Figure 29 illustrates a snapshot of the droplet deformation until the neck width stabilizes to a constant value. The typical timescale of the droplet deformation up to its equilibrium state is few seconds to tens of seconds, for oil-in-water droplets with hundreds of micrometers length, in channels with typically tens of microns in height.

Above $T*$:

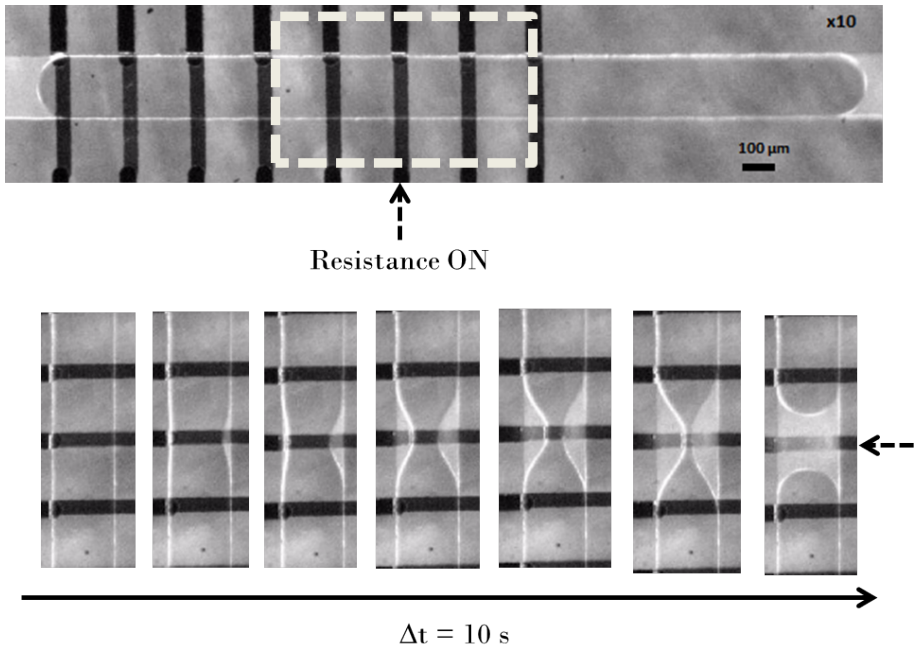

Figure 28: Snapshot of the droplet deformation in the vicinity of the heating resistance. 10 seconds after the resistance is switched on, the droplet breaks. In this experiment, the channel width is 200 µm and its height is 30 µm. The temperature at the level of the resistance is approximately 75 °C.

Below $T*$:

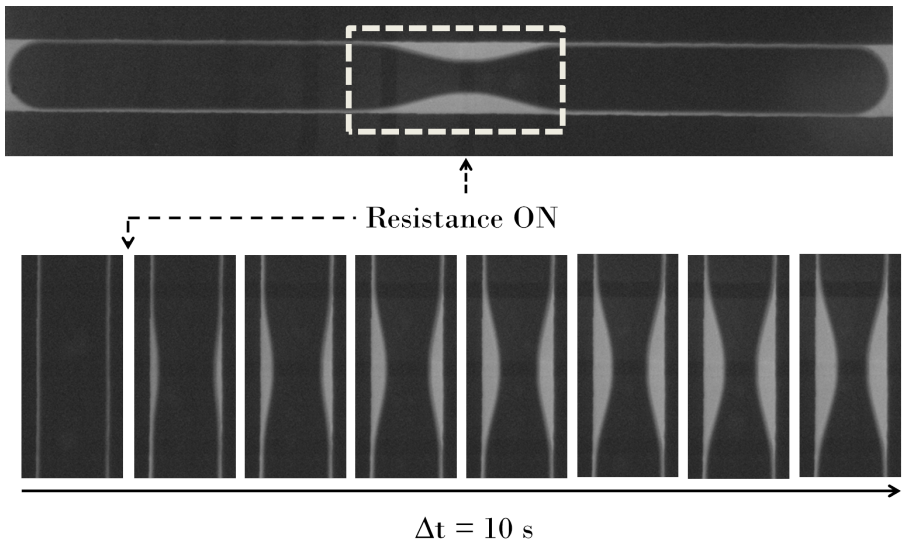

Figure 29: Snapshot of the droplet deformation in the vicinity of the heating resistance. The droplet starts to deform few hundreds of ms after the resistance is switched on, until reaching an equilibrium shape. The typical timescale of this process is ten seconds. In this experiment, the channel width is 200 µm and its height is 30 µm. The temperature at the level of the resistance is approximately 55 °C as measured with an infrared camera.

Figure 30 shows the time evolution of the neck width defined as $w - 2h_0(t)$ for the breaking (fig. 28) and the non-breaking droplet case (fig. 29). We recover that in the breaking case ($T = 74$ °C), the neck width $w - 2h_0(t)$ decreases over time until it reaches the value $e = 30$ µm and the droplet breaks. In the non-breaking case ($T = 54$ °C), the neck width decreases until it reaches a plateau.

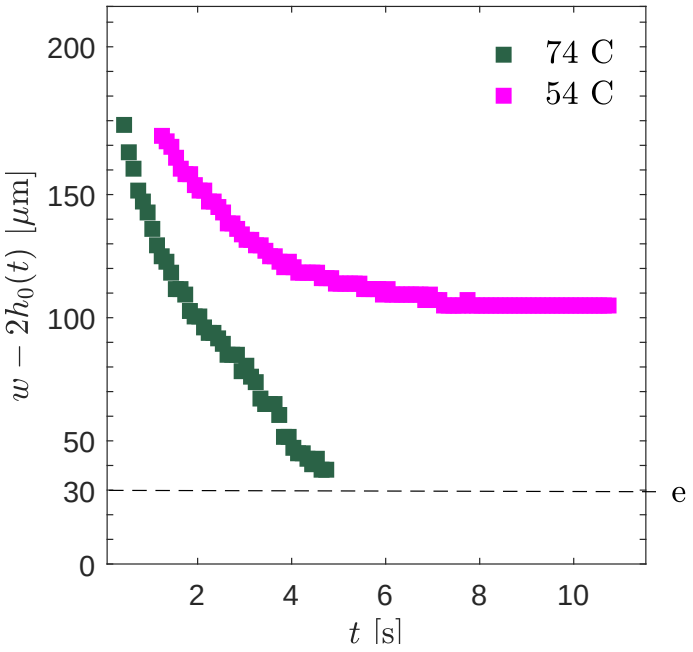

Figure 30: Time evolution of the neck width for a non-breaking and for a breaking droplet. In this experiment, the droplet length is 800 µm, the channel height and width are respectively 30 µm and 200 µm. For $T = 74$ °C, the neck width $w - 2h_0(t)$ decreases over time until it reaches the value $e = 30$ µm and the droplet breaks. For $T = 54$ °C, the neck width decreases until it reaches a plateau value that is approximately half of the channel width.

Figure 31 plots the same time evolution of the droplet neck width for a larger range of temperature (47 °C $< T <$ 74 °C). On the figure, we can assume that the critical temperature T^* above which the droplet breaks is comprised in between 54 °C and 60 °C.

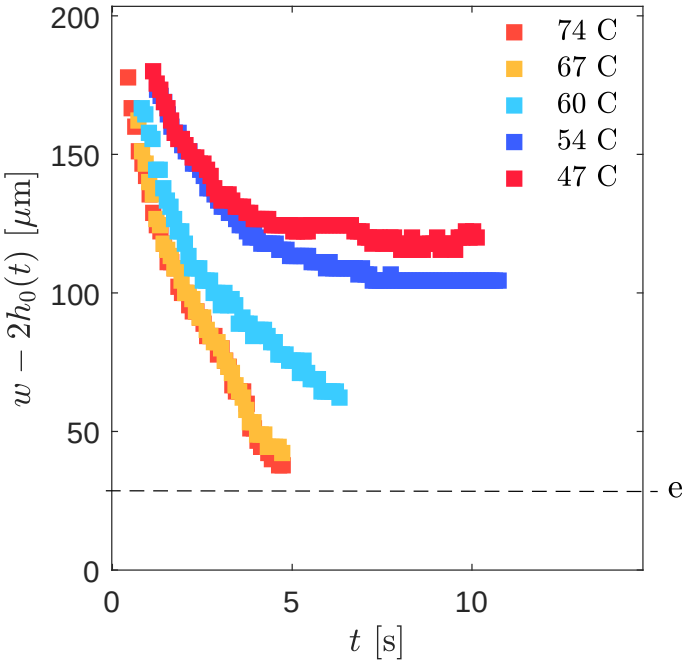

Figure 31: Time evolution of the neck width for a large range of temperature (47 °C $< T <$ 74 °C). Given the conditions of the experiment (800 µm long droplet in a 30 µm and 200 µm high and wide channel), we can assume that the critical temperature T^* above which the droplet breaks is comprised in between 54 °C and 60 °C.

In figure 32, we plot the dynamics of a series of droplets that break. The only geometrical characteristic that differentiates these droplets is their length. The temperature is the same for all these droplets and is higher than the critical temperature for them to break. On this plot, we put a line for $w - 2h_0 = e$, and we recover once again that the dynamics encounters a transition at this point: the droplets break. Lastly, we observe that the break-up dynamics increases with the droplet length.

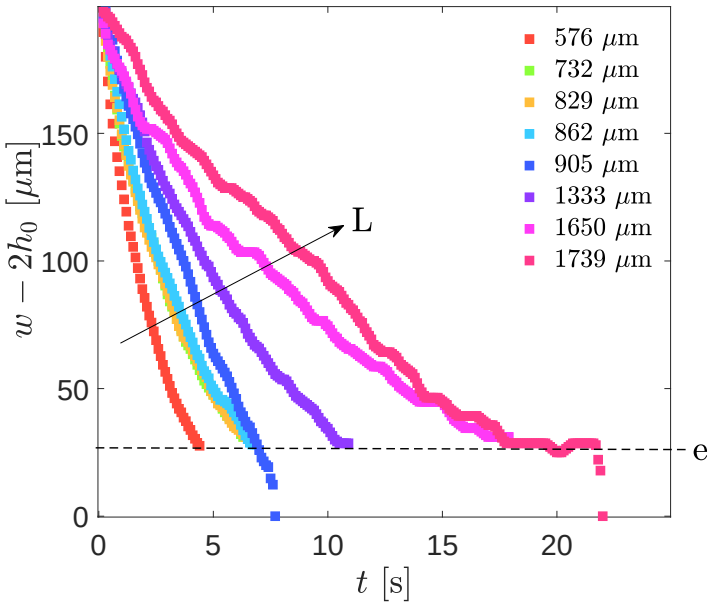

Figure 32: Time evolution of the neck width for a large range of droplet lengths (500 µm $< L <$ 1800 µm). In these experiments, the channel dimensions are $e = 30$ µm and $w = 200$ µm. In the experiments, the temperature is $T = 60°$C.

We now look at the time evolution of the entire interface profile defined as $h(x,t)$, see figure 33a. The latter appears to be self-similar at late times (the last 60 % of the dynamical process) such that we can define the function p_r that verifies $h(x,t) = h_0(t)p_r(x/b)$, for $-b < x < b$. In figure 33b, this function p_r is plotted versus the dimensionless variable u defined as $u = x/b$, b being the extent of the neck in the x-axis. The fact that the interface profile $h(x,t)$ can be expressed as the multiplication of two functions that depend respectively on time and space simplifies the model of the droplet deformation process. This separation of variables will be fully elaborated in the next section.

The variable $u = x/b$ can be defined independently on time since we notice in figure 33a, that b does not vary with time ($b \sim 200$ µm). At early times, this observation is no longer true and $b(t)$ can not be considered as constant, see the Appendix page 111. In figure 33, the interface profile is plotted 20 seconds after the beginning of the droplet deformation up to the end of the droplet deformation, 70 seconds after.

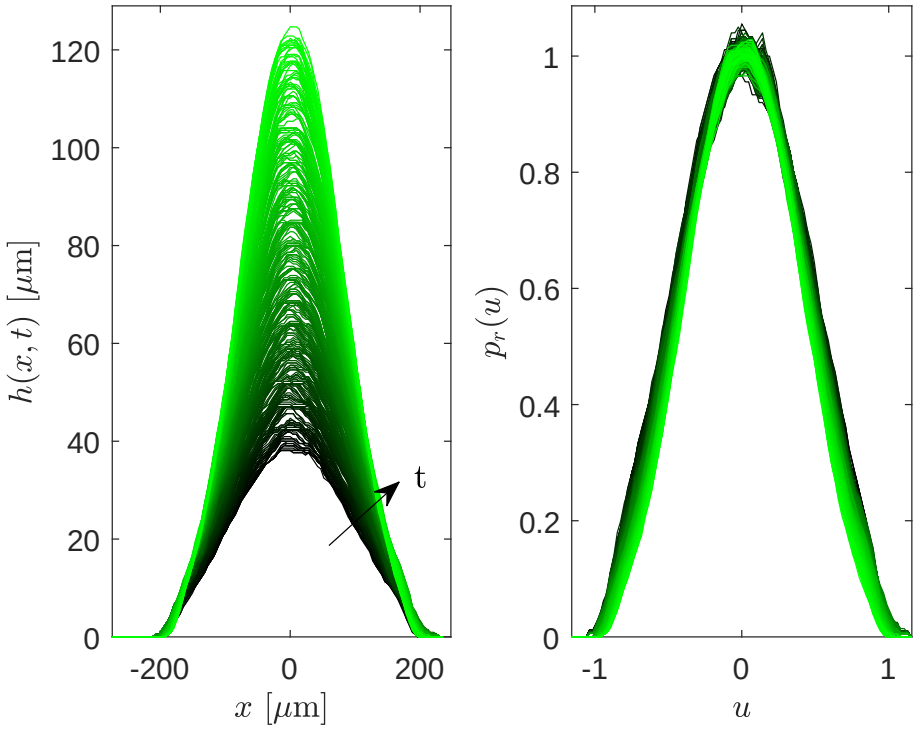

Figure 33: a) Entire interface profile time evolution of the neck during a droplet deformation experiment. Green curves correspond to late times while black curves correspond to early times. The profiles $h(x,t)$ are plotted from $t = 20$ s after the beginning of the droplet deformation up to $t = 90$ s. The dimensions of the channel are $w = 400$ µm and $e = 30$ µm. In this experiment, the droplet length is 3800 µm. b) Same interface profiles rescaled by $h_0(t)$. The x-axis is rescaled by b.

16 The break-up criteria: experimental check

We have observed in the last section that droplets break when the neck width $w - 2h_0(t)$ gets smaller than the channel height e. This criteria is consistent with several studies that deal with droplet break-up in a confined geometry in the literature [82, 45].

However, as an experimental check, we show that when $w - 2h_0(t) = e$, the surface of the deformed droplet gets larger than the surface of two splitted droplets such that it becomes more energetically favorable for the droplet to break. We define τ_{break} as the experimental time at which the droplet breaks.

Approximately, we calculate the perimeter Φ of the in-plane droplet interface in the neck region at most $\Delta t = 100$ ms before the break-up and 100 ms after the break-up, see fig. 34. We assume that the cavity height profile along this in-plane perimeter is constant during this period of time - that lasts at most 200 ms.

After a simple image processing, we find that $\Phi(\tau_{break} - \Delta t) = 512$ µm and that $\Phi(\tau_{break} + \Delta t) = 460$ µm. We can then assume that the surface of the droplet

interface in the neck region is approximately 512*e μm^2 just before the break-up and approximately 460*e μm^2 just after the break-up. While this preliminary analysis is highly approximate, we will show more rigorously in the following that droplet breakup is energetically favorable under the conditions of a sloped channel geometry.

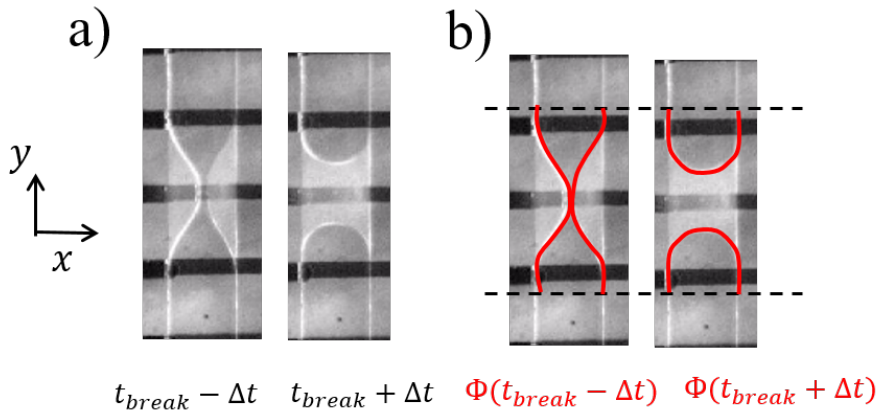

Figure 34: a) Zoom on the neck region of a droplet captured just before and just after the break-up. b) The contour of the in-plane droplet interface that is detected over time to measure Φ is highlighted in red.

The following sections provide more robust insights on the physical mechanisms that are at play during the droplet deformation.

17 The physical mechanisms at play

We identify two physical mechanisms that may account for the droplet deformation: the Marangoni effect and the confinement gradient effect (called the mechanical effect). Both effects are discussed in this section.

17.0.1 Why might the droplet deform when a gradient of surface tension is established at its interface ?

The thermal Marangoni effect corresponds to a variation of surface tension with temperature. The surface tension gradient that establishes along the droplet interface sets a stress at the interface such that the continuity of the tangential stresses writes

$$\left(\eta_o \frac{\partial v_x^{(o)}}{\partial n} - \eta_w \frac{\partial v_x^{(w)}}{\partial n} \right)_{interface} = \frac{d\gamma}{dx} \tag{26}$$

where n defines the normal direction at the interface. In the studied system (mineral oil in water and SDS), surface tension increases with temperature. The Marangoni

stress that is associated with this increase has been characterized in chapter Materials and Methods.

When the temperature is 70 °C at the level of the resistance, we find that the order of magnitude of the Marangoni stress is 0.2 $N.m^{-2}$.

$$\frac{d\gamma}{dx} = \frac{d\gamma}{dT}\frac{dT}{dx} \sim 10^{-5} * 10^{4} \sim 10^{-1} N.m^{-2} \tag{27}$$

Figure 35 illustrates the flows that can stem from the thermal Marangoni effect at the droplet interface. These flows are oriented towards the high surface tension regions.

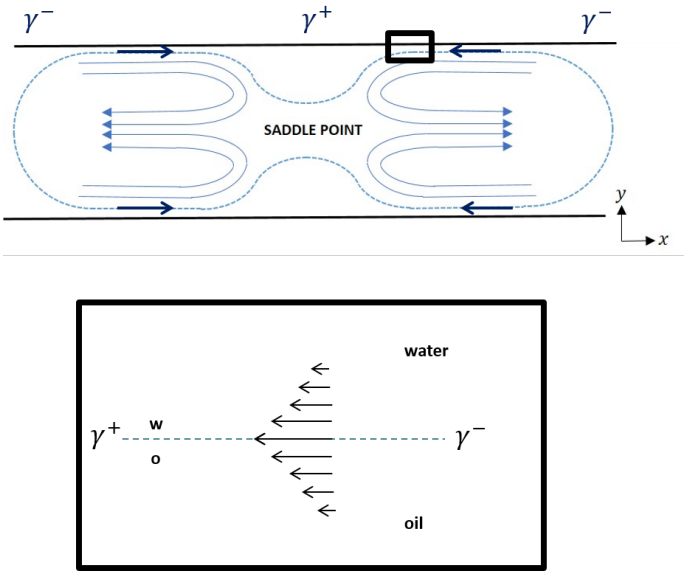

Figure 35: Flow pattern that may arise from the thermal Marangoni effect. The droplet interface is moved by the Marangoni stress and its advection creates a flow near the interface in both phases. This flow is oriented towards the hot regions. By symmetry, there might be flow recirculations in the droplet phase such that the droplet interface can be deformed by the incoming flow of the outer phase towards the neck of the droplet.

We prove in the following that the Marangoni effect is not the prevailing mechanism in the droplet deformation process. However, the Appendix page 111 provides an estimation of the order of magnitude of a break-up time that would only be due to Marangoni flows.

17.0.2 Why might the droplet deform when the channel locally contracts ?

The mechanical effect corresponds to the local variation of topography induced by the thermal dilation of the channel walls. This dilation is illustrated in figure 36. The figure recaps all the parameters that describe the droplet deformation. More specifically, the channel thermal dilation is characterized by two parameters: its

horizontal extent, d_x and its vertical extent, d_z. We recall that the variation of d_z with the temperature has been characterized *in-situ* while we have not characterized the horizontal extent d_x of the topographic variation in the channel, see the chapter Materials and Methods. The function $e(x)$ describes the channel height that varies along the droplet length.

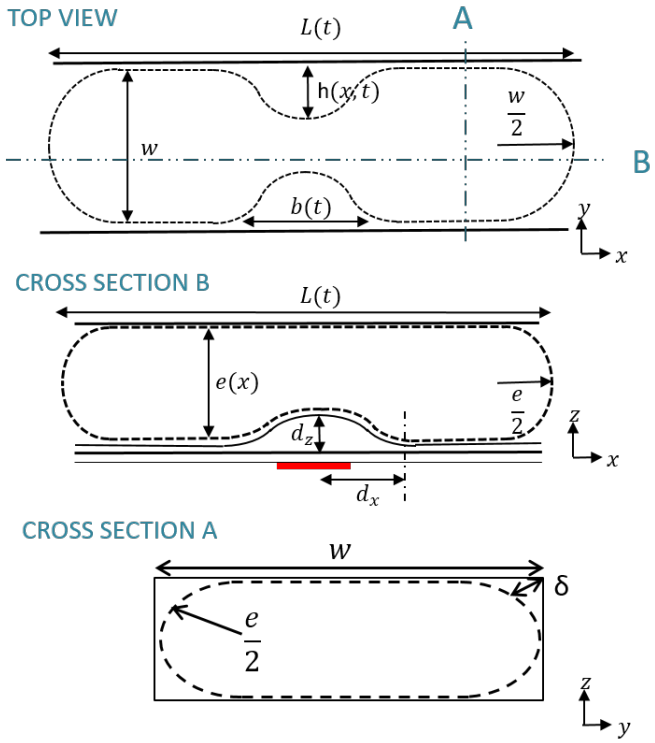

Figure 36: Geometrical parameters that are used to describe the droplet deformation.

When the channel height is constant and equal to e, we recall that the radius of the droplet meniscus in the plane (y, z) is constant and equal to $e/2$, see the chapter Introduction for more details. When the droplet undergoes a local gradient of confinement, this radius is decreased as $e(x)/2$, meaning that the droplet curvature in the (y, z) suddenly increases. Where the confinement gradient is localized, the droplet mean curvature writes

$$\mathcal{C} = \frac{\partial_x^2 h}{\sqrt{1 + (\partial_x h)^{3/2}}} + \frac{2}{e(x)} \tag{28}$$

where $\frac{\partial_x^2 h}{\sqrt{1+(\partial_x h)^{3/2}}}$ is its in-plane curvature.

At equilibrium, to maintain $\mathcal{C}$ constant, $\frac{\partial_x^2 h}{\sqrt{1+(\partial_x h)^{3/2}}}$ should decrease when $\frac{2}{e(x)}$ increases. Initially, the in-plane curvature of the droplet is zero at the level of the side channel walls, see figure 36. Thus, when the confinement gradient is imposed on the droplet, this curvature is expected to become more and more negative as

$e(x)$ decreases. This mechanism could account for the neck formation at the center of the droplet where the confinement gradient is established. Indeed, Dangla et al. have shown that a confinement gradient of only few degrees could break a thread, as the result of the formation of this negative in-plane curvature in response to the decrease of the channel height [45].

In order to determine whether it is the mechanical or the Marangoni effect that prevails in the droplet deformation process, we design an experimental device that allows to isolate the confinement gradient effect without any temperature increase.

17.0.3 Comparison with a purely mechanical device

A device that mimics the confinement gradient induced by the hot resistance has been designed and fabricated using a micro-milling machine. This device, that is schemed in figure 37, contains a symmetric and linear confinement gradient. This confinement gradient is defined by two parameters d_x and d_z that describe respectively its horizontal and vertical extent. Different systems were designed in which d_x varies from 400 to 800 µm and d_z from 3 to 10 µm, e varying from 20 µm to 40 µm and w varying from 200 µm to 400 µm. The values of d_x and d_z are measured with a mechanical profilometer (Dektak 6M). The ratio $\frac{d_z}{d_x}$ defines the tilt θ of the channel top wall and this tilt ranges from 0.2 ° to 1.4 °. In these devices, called "mechanical" devices, the channel height $e(x)$ can be defined as a linear piecewise function:

- for $-\infty < x < -d_x$, $e(x) = e$
- for $-d_x < x < 0$, $e(x) = e - d_z - \theta x$
- for $0 < x < d_x$, $e(x) = e - d_z + \theta x$
- for $d_x < x < \infty$, $e(x) = e$

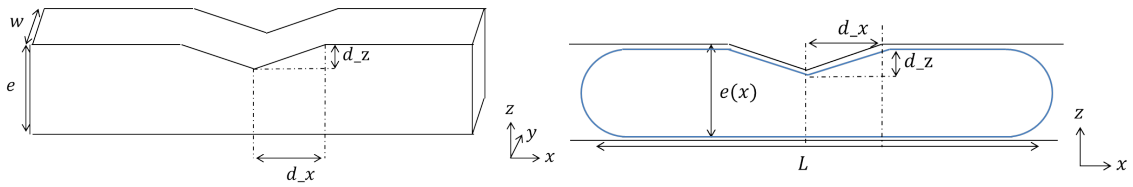

Figure 37: Scheme of a mechanical device in which a confinement gradient is indented. The system is called the "mechanical" system and is compared to the "thermomechanical" system. a) 3D view b) Cross view in the plane (x, z).

In the "mechanical" devices, droplets deform when they undergo the gradient of confinement, similarly to the "thermomechanical" devices. Figure 38 illustrates a

snapshot of a 1600 µm long droplet that deforms in a "mechanical" device in which $d_z = 5$ µm, $d_x = 400$ µm, $e = 30$ µm and $w = 400$ µm.

In a "thermomechanical" device, the confinement gradient is applied on demand on the droplet once the latter is static in the channel. In the "mechanical" device, the droplet has to be pushed under the confinement gradient. The droplet velocity is monitored with a pressure controller that adjusts the pressure at the entrance of the channel. When the droplet is centered under the confinement gradient, the latter is stopped - the pressure is decreased to zero at the entrance of the channel. The droplet starts to deform as soon as it undergoes the confinement gradient. In the following, we only observe the period of time during which the droplet is stopped in the channel. This period corresponds to the late times of the droplet deformation (typically the last 40-50% of the droplet deformation process).

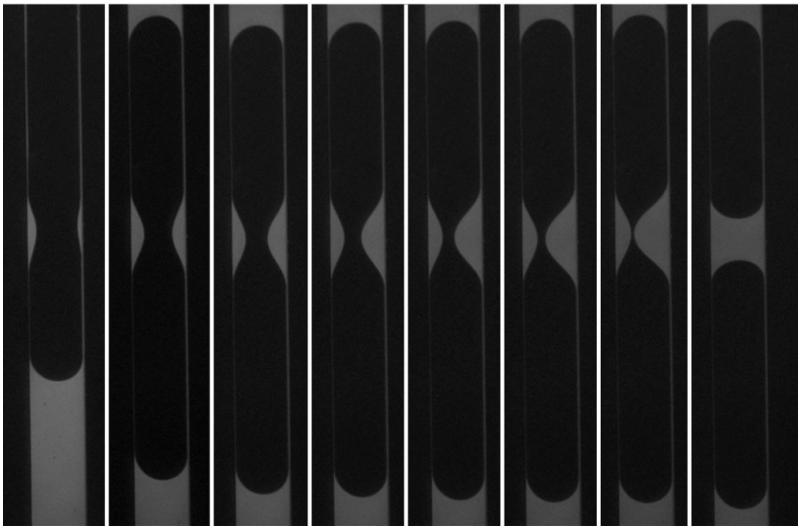

Figure 38: Snapshots of the droplet deformation in a "mechanical" device in which $d_z = 5$ µm, $d_x = 400$ µm, $e = 30$ µm and $w = 400$ µm. The droplet is 1600 µm long. The droplet deformation is considered only after the third frame when the droplet is stopped in the channel. The images are equally spaced in time and the total duration of the snapshot is 104 seconds.

Figure 39 plots the time evolution of the entire interface profile of the droplet. The latter appears to be also self-similar at late times, this represents a further similarity to the "thermomechanical" device. For this device, we can also define a function p_m that verifies $h(x,t) = h_0(t)p_m(x/b)$ for $-b < x < b$. The function p_m is plotted in Figure 39b versus $u = x/b$, b being the extent of the neck in the x-axis that is also constant over time.

Remark:

For this experiment, the neck extension in the x-axis is approximately 350 µm, similarly to the extension of the confinement gradient d_x that is equal to 400 µm. This observation is important for the model section.

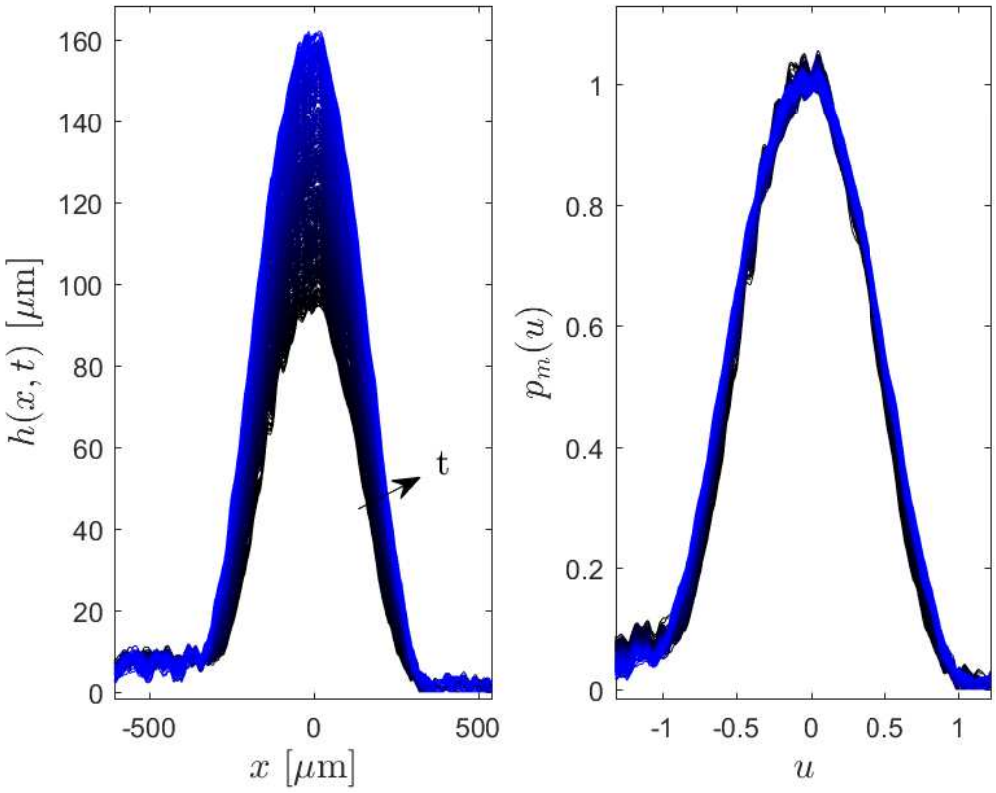

Figure 39: Time evolution of the interface profile $h(x,t)$ of the droplet deformation in a "mechanical" device in which $d_z = 5$ µm, $d_x = 400$ µm, $e = 30$ µm and $w = 400$ µm. The droplet is 1600 µm long. The timelapse that is plotted is around 70s. During this period of time, $h(x,t)$ is self-similar and writes $h(x,t) = h_0(t)p(x)$. We define $u = x/b$ where b is the x-axis extent of the neck that is constant over time.

In figure 40, we compare the self-similar function p_r and p_m respectively for the "thermomechanical" and the "mechanical" devices as a function of u ($u = x/b$ where b is the extent of the droplet deformation in the x-axis). We observe that the self-similar functions in both devices collapse on top of each other with an error of 10%. This observation supports the idea that the droplet is mainly deformed by the confinement gradient that is imposed in the channel and that the thermal Marangoni effect can be disregarded. Given these considerations, we write a model in the next section that aims at predicting the droplet equilibrium shape and its break-up given the geometrical constraints of the channel.

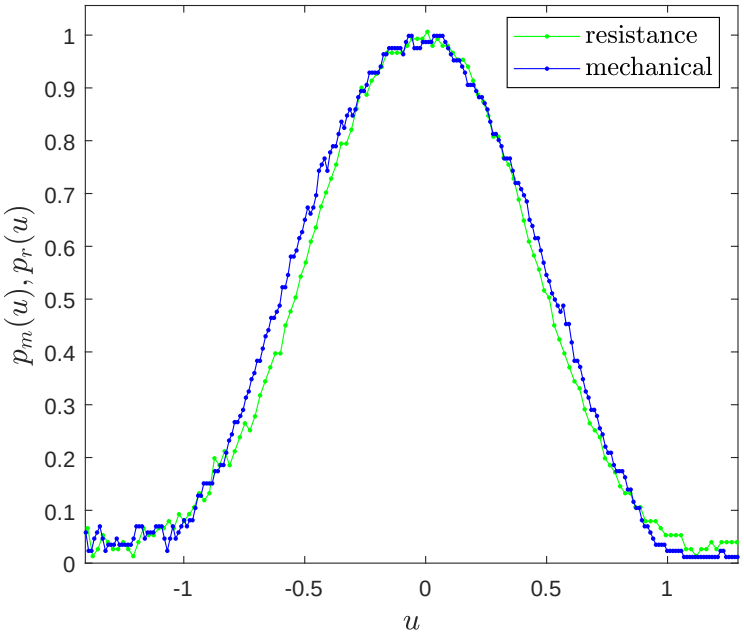

Figure 40: Comparison of the self-similar functions p of the droplet deformation in between the "thermomechanical" and the "mechanical" device.

18 Predicting the droplet deformation shape

To predict the droplet deformation shape, we calculate the minimum surface that the droplet can adopt when the confinement gradient is imposed.

18.1 Surface minimization

The surface energy of the droplet writes $E = \gamma S$ where S is the surface of the droplet. Surface tension leads the droplet to minimize its surface energy. We calculate the excess surface of the droplet that is the difference between the surface energy of the droplet when the latter is deformed and the surface energy of the droplet when the latter has its initial plug-like shape. This calculation takes into account the variation of the channel height $e(x)$. We write that the excess surface energy of the droplet is $E_\Sigma = \gamma \Delta S$. In the following discussion, we assume that the surface tension is constant along the droplet interface such that minimizing E is equivalent to minimizing ΔS.

Because the droplet is centered at the level of the confinement gradient, the axis $x = 0$ is an axis of symmetry for the droplet. Hence, we only consider the half-surface of the droplet and we distinguish three regions :

- the droplet extremity (1) which only translates in the channel
- the sides of the droplet (2) which are elongated during the evolution and where the gutters are localized

- the confinement gradient region (3) where the neck forms.

Figure 41 illustrates the regions 1, 2 and 3. We calculate the excess surface of the droplet interface in each of these regions.

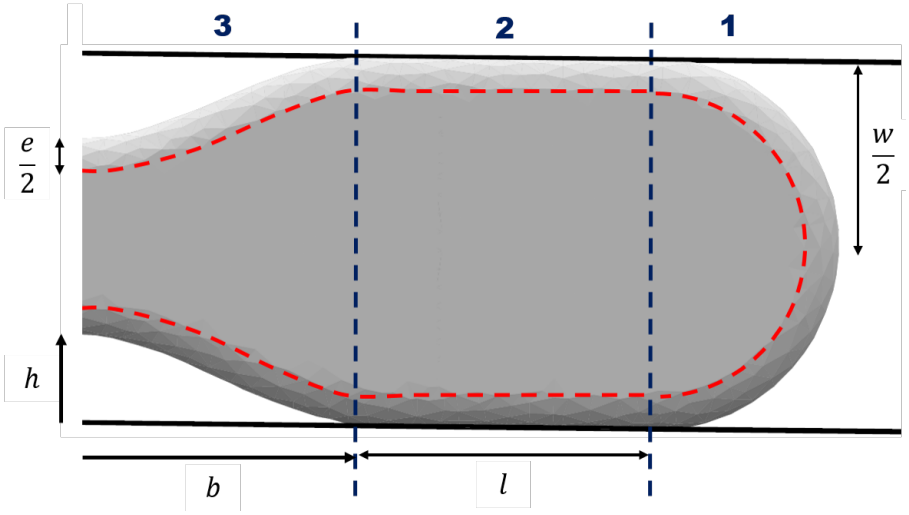

Figure 41: Regions (1,2,3) of the droplet surface.

In region 1:

By definition, the surface of the droplet interface is not modified in this region.

In region 2

The droplet is elongated by volume conservation. Indeed, the volume that is lost in region **3** for the formation of the neck is moved to region **2**. The droplet is then elongated by Δl.

Since we observe on figure 39 that the extent of the neck is the x-axis, b, is of the same order of magnitude as the confinement gradient extent d_x, we consider that the cavity height is constant in region **2**, equal to e and decreases only in region **3**. The total surface of the droplet including the menisci is given by

$$\Delta S_2 = (2(w-e)+\pi e)\Delta l \tag{29}$$

The droplet elongation Δl is deduced from the volume conservation in the droplet.

The volume that is lost in region **3** is

$$\Omega_1 = \left((w-e)e+\frac{\pi e^2}{4}\right)b - e\left((w-e)b - 2\int_0^b h(x,t)e(x)\mathrm{dx}\right) - \int_0^b \frac{\pi e^2(x)}{4}\sqrt{1+\partial_x h^2}\mathrm{dx} \tag{30}$$

that simplifies as

$$\Omega_1 = 2\int_0^b h(x,t)e(x)\mathrm{dx} - \int_0^{\mathrm{b}} \frac{\pi \mathrm{e}^2(\mathrm{x})}{4}(\sqrt{1+\partial_{\mathrm{x}}\mathrm{h}^2}-1)\mathrm{dx}. \tag{31}$$

This volume must be equal to the volume that is increased in region **2**

$$\Omega_2 = e\left((w-e)+\frac{\pi e}{4}\right)\Delta l \tag{32}$$

Ω_1 must be equal to Ω_2 by volume conservation such that we get

$$e\left((w-e)+\frac{\pi e}{4}\right)\Delta l = 2\int_0^b h(x,t)e(x)\mathrm{dx} - \int_0^{\mathrm{b}} \frac{\pi \mathrm{e}^2(\mathrm{x})}{4}(\sqrt{1+\partial_{\mathrm{x}}\mathrm{h}^2}-1)\mathrm{dx} \tag{33}$$

By replacing the expression of Δl obtained with the volume conservation in equation (33) in the expression of the excess surface in equation (29), we get the expression of the surface excess in region **2**.

$$\Delta S_2 = \frac{2(w-e)+\pi e}{(w-e)e+\frac{\pi e^2}{4}}\left[2\int_0^b h(x,t)e(x)\mathrm{dx} - \int_0^{\mathrm{b}} \frac{\pi \mathrm{e}^2(\mathrm{x})}{4}(\sqrt{1+\partial_{\mathrm{x}}\mathrm{h}^2}-1)\mathrm{dx}\right] \tag{34}$$

In region 3

In this region, the surface of the droplet interface decreases to counter the excess surface induced by the confinement gradient. The top channel is considered to be flat while the bottom channel wall is locally deformed by the confinement gradient tilted with a angle $\theta << 1$.

1. The excess surface of the top interface writes

$$\Delta S_3^t = \left[wb - 2\int_0^b \left(h(x,t)+\frac{e(x)}{2}\right)\mathrm{dx}\right] - (w-e)\,b \tag{35}$$

so,

$$\Delta S_3^t = -2\int_0^b \left(h(x,t)+\frac{e(x)}{2}\right)\mathrm{dx} + \mathrm{eb} \tag{36}$$

$$\Delta S_3^t = -2\int_0^b \left(h(x,t)+\frac{e(x)-e}{2}\right)\mathrm{dx} \tag{37}$$

Since $e - e(x) < d_z$ and $d_z \sim 5$ µm, $\frac{e(x)-e}{2} << h(x,t)$ and the expression of ΔS_3^t simplifies as

$$\Delta S_3^t = -2\int_0^b h(x,t)\mathrm{dx} \tag{38}$$

2. The excess surface of the bottom interface writes

$$\Delta S_3^b = \left[\left(wb - 2\int_0^b \left(h(x,t) - \frac{e(x)}{2}\right)\mathrm{dx}\right) - (w-e)\,b\right]\frac{1}{cos\theta} \tag{39}$$

simarly to ΔS_3^t, ΔS_3^b simplifies as

$$\Delta S_3^b = -2\int_0^b h(x,t)\frac{1}{cos\theta}\mathrm{dx} \tag{40}$$

As a result, $\Delta S_3 = \Delta S_3^t + \Delta S_3^b$ gives

$$\Delta S_3 = -2\int_0^b h(x,t)\left(1 + \frac{1}{cos\theta}\right)\mathrm{dx} \tag{41}$$

3. The excess surface of the droplet menisci writes

$$\Delta S_3^m = 2\int_0^b \pi e(x)(\sqrt{1+\partial_x h^2} - 1)\mathrm{dx} \tag{42}$$

Conclusion

The total excess surface of the droplet writes

$$\Delta S = -2\int_0^b \left(1 + \frac{1}{\cos\theta}\right)\, h(x,t)\mathrm{dx} + 2\int_0^b \pi \mathrm{e(x)}(\sqrt{1+\partial_\mathrm{x}\mathrm{h}^2} - 1)\mathrm{dx} + (2(w-e) + \pi e)\Delta l \tag{43}$$

In this expression, we replace

- $h(x,t)$ by $h_0 p(x/b)$ and
- $\partial_x h$ by $\frac{h_0}{b}p'(x/b)$
- $e(x)$ by $\min(e, e - d_z\frac{d_x - x}{d_x})$.

The function p is extracted from the experimental data. More precisely, p is obtained by fitting the experimental profiles illustrated in figure 40. We find for $0 < x < 1$,

$$p(x) = -1.6727x^5 + 3.3531x^4 + 0.317x^3 - 3.0016x^2 + 0.0033x + 1.0001 \tag{44}$$

and

$$p'(x) = -5 * 1.6727x^4 + 4 * 3.3531x^3 + 3 * 0.317x^2 - 3.0016x + 0.0033. \tag{45}$$

18.2 Minimization of the droplet surface

We minimize the excess surface of the droplet $\Delta S(h, b)$ in order to predict the equilibrium shape of the droplet deformation defined by $b_{eq} = b(t_{eq})$ and $h_{eq} = h_0(t_{eq})$, t_{eq} being the time at which the droplet reaches an equilibrium shape. We solve the system of equation

$$\frac{\partial \Delta S}{\partial h}(h_{eq}, b_{eq}) = 0 \tag{46}$$

and

$$\frac{\partial \Delta S}{\partial b}(h_{eq}, b_{eq}) = 0 \tag{47}$$

using the matlab function **fminsearch**.

We find that b_{eq} and h_{eq} depend on four geometrical parameters of the system: the channel width and height, w and e and the confinement gradient extents d_x and d_z. For example, figure 42 illustrates the theoretical predictions of the droplet deformation for a $w = 400$ µm wide channel and for a confinement gradient that has a $d_x = 400$ µm x-axis extent. To build this phase diagram, we find the minimum (h_{eq}, b_{eq}) of ΔS for e varying from 15 µm to 50 µm and for d_z varying from 0 µm to 10 µm. If h_{eq} verifies $w - 2h_{eq} < e$, we say that the droplet breaks. If $h_{eq} < 1$ µm, we say that there is no deformation. Otherwise, we draw a transient region in which we predict that the droplet deforms but does not break.

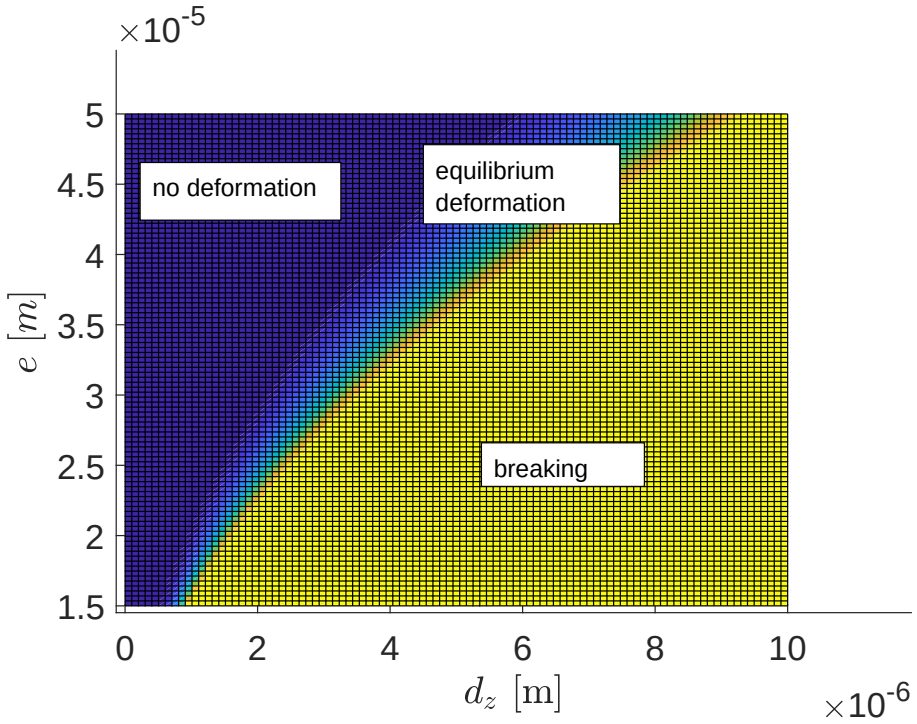

Figure 42: Phase diagram of (e, d_z) for $d_x = 400$ µm and $w = 400$ µm, that predicts the fate of droplets in devices with dimensions $(e, w = 400, d_z, d_x = 400)$: breaking (below the orange line) or non-breaking (above the orange line). A transient region is plotted above the orange line and corresponds to situations in which droplets deform but reach an equilibrium shape. Then, a darker zone is plotted that corresponds to cases in which droplets do not deform.

We are thus able to draw a phase diagram in figure 43 that predicts the fate of droplets as a function of three dimensionless parameters $\frac{d_z}{w}$, $\frac{e}{w}$ and $\frac{d_x}{w}$.

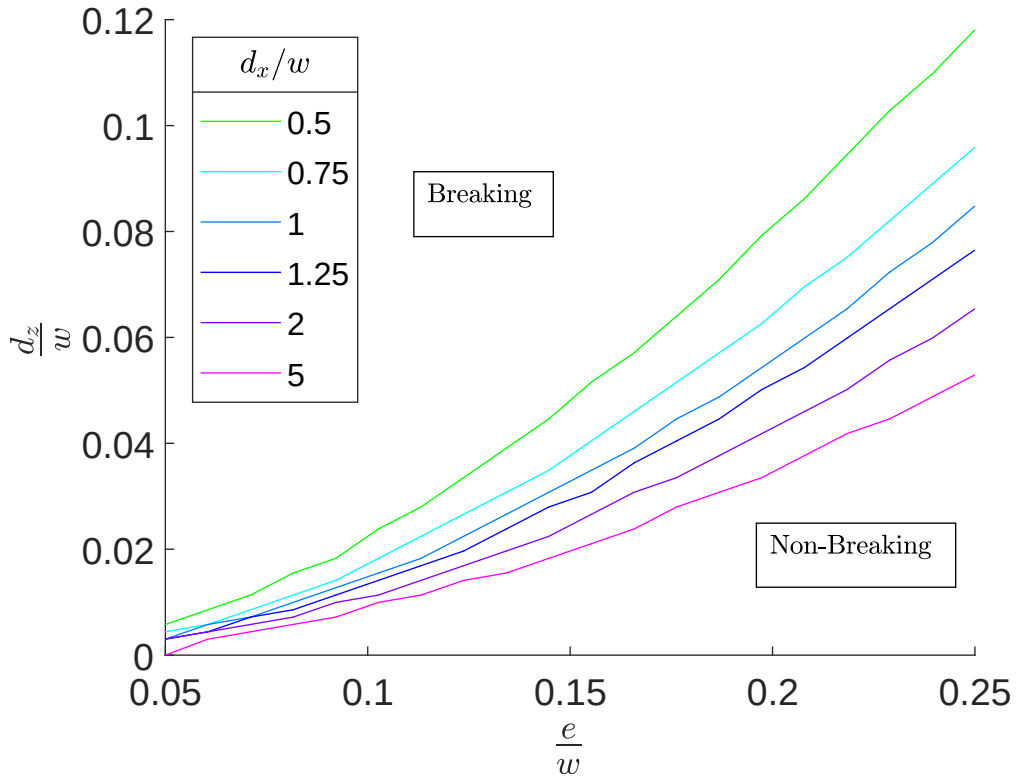

Figure 43: Phase diagram that predicts the fate of droplets in devices with dimensions (e, w, d_z, d_x): breaking (above the line) or non-breaking (below the line). The geometric parameters are adimensionned by the channel width w. The curves correspond to the spectrum of equations $w - 2h_{eq} = e$ plotted for different ratios $\frac{d_x}{w}$.

The experimental data obtained with the "mechanical" devices are plotted on this phase diagram, see figure 44. The experimental data seem consistent with theory. To further validate this model, the theoretical predictions of h_{eq} and b_{eq} are compared to Surface Evolver simulations.

Remark:

The experimental data obtained with the "thermomechanical" device can not be illustrated on the diagram since d_x has not been properly characterized in this device. Having said this, we give in the next section some details of comparisons of this model with the experimental data to extract values for d_x.

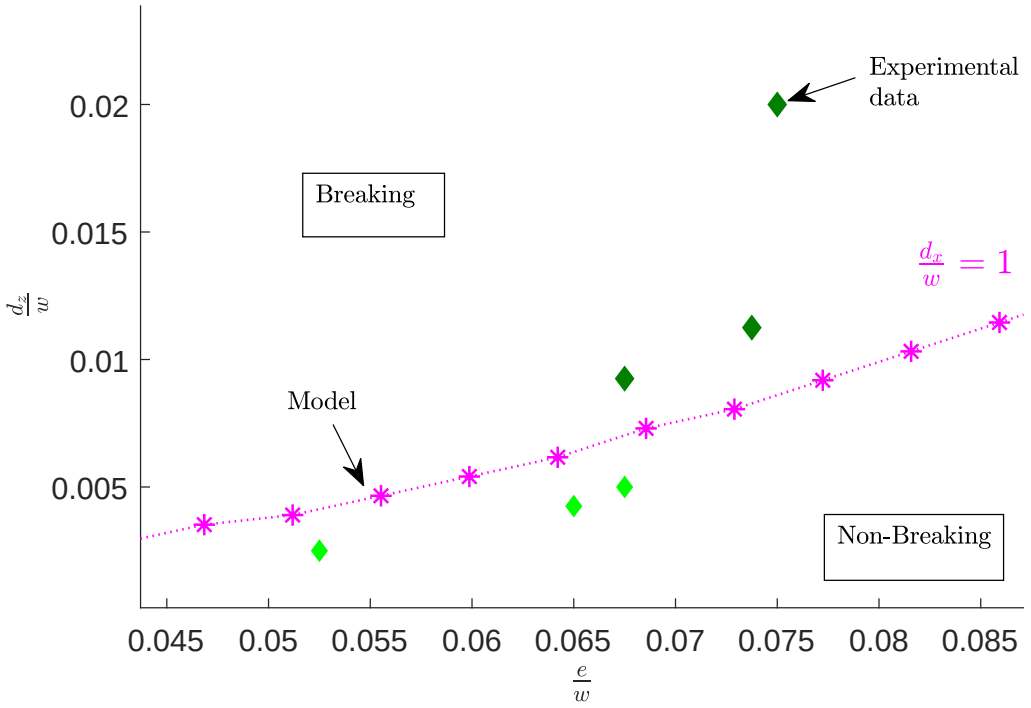

Figure 44: Phase diagram 43 on which the experimental data obtained with "mechanical devices" are added. Dark green dots correspond to breaking devices, light green dots correspond to non-breaking "mechanical" devices. In the latter devices, the droplets do not even deform.

18.3 Validation of the model: Surface evolver simulations

Surface Evolver is a free simulation software that minimizes the surface energy of an object subject to predefined geometric and energetic constraints. It uses 2D finite elements to represent 3D bodies and minimizes their energy through a sequence of mesh refining. A detailed description of the Surface Evolver algorithm is given in [86]. Our model consists in a fixed volume droplet that is bounded in a rectangular microchannel that contains a confinement gradient as described in 12. An additional symmetry constraint ensures that the droplet is centered around the deformation.

Surface Evolver calculates the minimum energy geometry of the droplet but gives us no information on the dynamics of the droplet evolution. It allows us to compute equilibrium shapes for a range of geometric parameters and to predict if the droplet will break or not. Figure 45 illustrates an example of a droplet deformation induced by a local gradient of confinement that is achieved with Surface Evolver simulations.

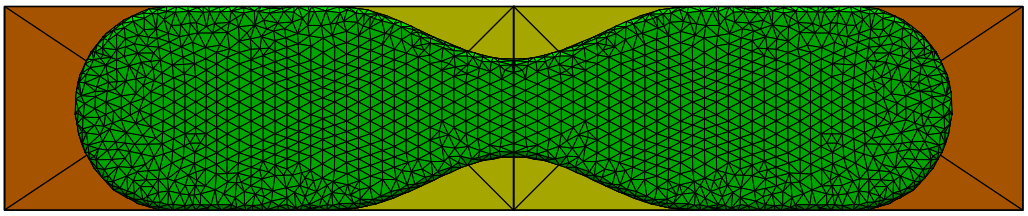

Figure 45: a) Example of the surface evolver simulations that are carried out for $d_z = 5$ µm, $d_x = 400$ µm, $e = 30$ µm and $w = 400$ µm. These dimensions are similar to the ones of a mechanical device that has been used in our experiments.

Figure 46 shows that the interface profile of the droplet provided by Surface Evolver collapse on top of the one predicted by the model with an error that is smaller than 5 %.

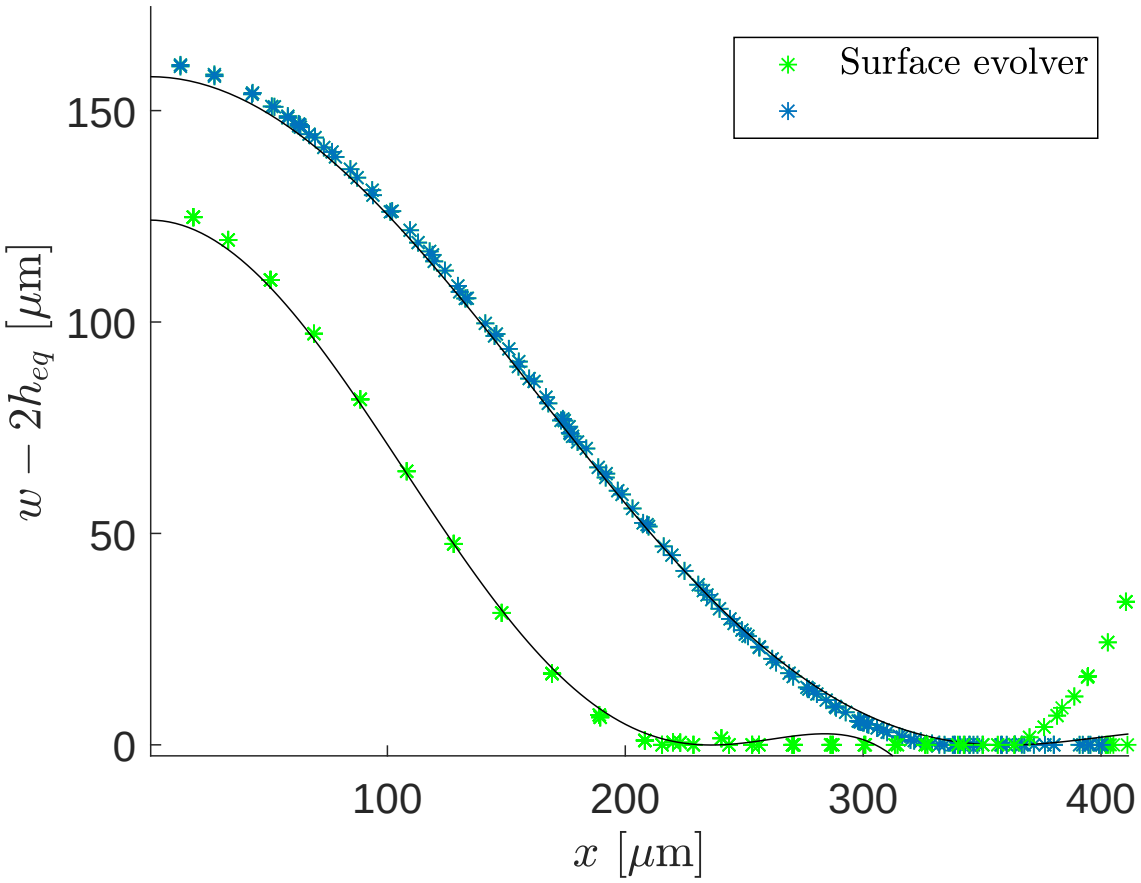

Figure 46: Plot of the droplet interface profile in the neck region provided by Surface Evolver (cross markers) and by the semi-theoretical model (black lines using expression 44) for two sets of geometric parameters: (blue) $d_z = 4\mu m$, $d_x = 400\mu m$, $e = 35\mu m$ and $w = 400\mu m$ and (green) $d_z = 9\mu m$, $d_x = 300\mu m$, $e = 40\mu m$ and $w = 200\mu m$

The surface minimization of the droplet seems to capture with a good agreement the deformation of the latter. This model neglects the thermal Marangoni effect contribution which thus suggests that its contribution to the equilibrium shapes is

minimal. In the next section, we build a model that aims at predicting the dynamics of the droplet deformation.

19 Predicting the droplet dynamics

The droplet deformation that is studied in the last section is not immediate since it is mediated by the viscous dissipation in the biphasic system. In this section, we are interested in predicting the dynamics of the droplet deformation which requires first to identify the origin of this viscous dissipation. While the analytical description of the viscous distribution in the system is complex, an experimental observation makes us assume that the dynamics of the deformation process is set by the viscous dissipation of water in the gutters.

19.1 Localization of the viscous dissipation in the gutters

Figure 48 shows the variation of the break-up time τ_{break} defined by $w-2h_0(\tau_{break}) = e$ as a function of the droplet length for the channel geometry. We observe that the break-up time varies linearly with the droplet length. We notice that when τ_{break} tends to zero, the droplet length is approximately 300 µm which is approximately equal to b in these experiments, see figure 39a that shows the interface profile of the neck in the same channel geometry: $\delta = 5\mu m$, $b = 400\mu m$, $e = 30\mu m$ and $w = 400\mu m$.

If we now plot τ_{break} as a function of the mean gutter length, we observe that the curve $\tau_{break} = f(L)$ is shifted to (0,0), see figure 48b. To calculate the mean gutter length of the droplet, we calculate the equivalent length of the four gutters in parallel through which the neck fills:

$$\frac{1}{L_g} = \frac{1}{L_g^{left}} + \frac{1}{L_g^{right}} \tag{48}$$

where L_g^{left} and L_g^{right} are defined in figure 47. Given these observations, we are motivated to only take into account the viscous dissipation of water that drains through the gutters to model the dynamics of the droplet deformation.

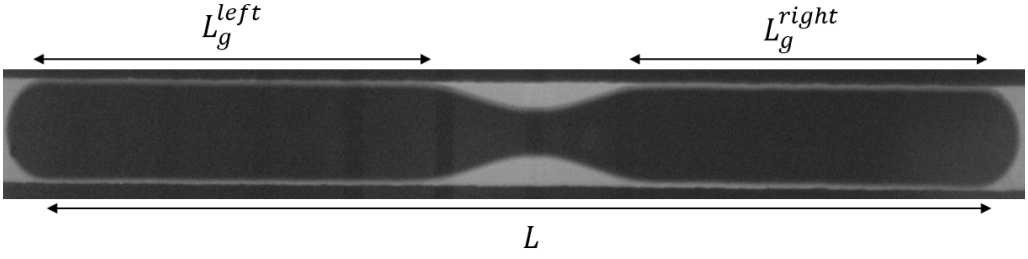

Figure 47: Definition of the L_g^{left} and L_g^{right}.

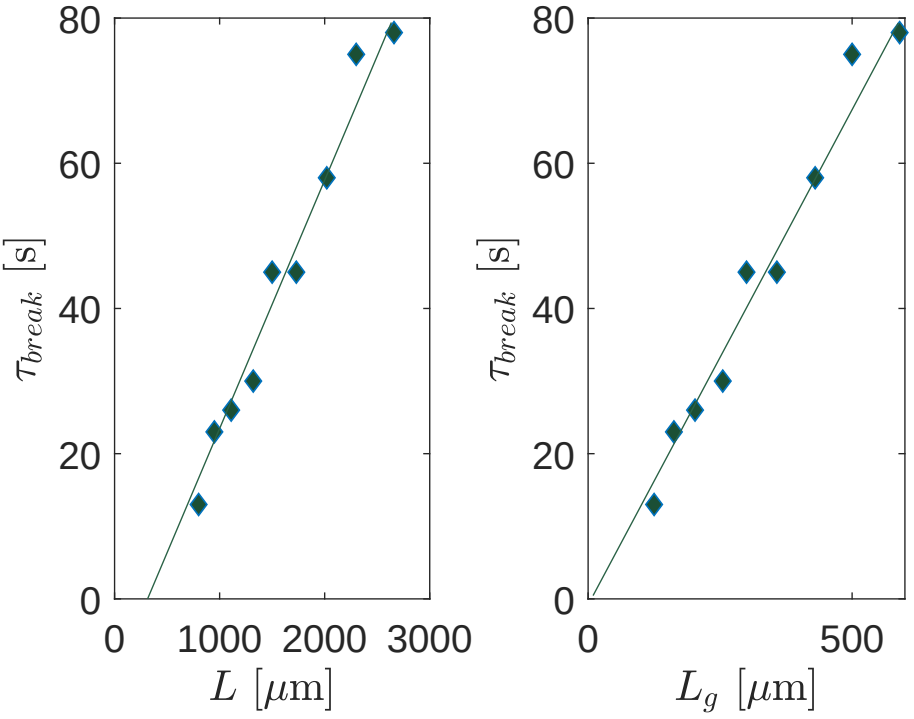

Figure 48: Break-up time of droplets in a mechanical gradient depending on drop effective size (geometric parameters : $\delta = 5\mu m$, $b = 400\mu m$, $e = 30\mu m$ and $w = 400\mu m$

19.2 Power balance

To model the droplet deformation dynamics, we write a power balance that compares the viscous dissipation power with the excess surface energy that is increased in the system per unit of time.

The viscous dissipation power

The viscous dissipation power in the system is [37]

$$P = \int\int\int \eta(\nabla v + {}^T\nabla v)^2 d\Omega \tag{49}$$

where η is the viscosity of the fluid, v is the velocity field in the fluid, Ω is the volume of the fluid in which the viscous power is calculated.

The volume of the gutters scales as $e^2 L_g$, e^2 being the typical section of the gutters. Flows shear on the typical size of the gutters e. Thus, if we only take into account the viscous dissipation in the gutters (see section 21.2), the power scales as

$$\mathcal{P} \sim \eta_w \frac{v^2}{e^2} e^2 L_g \tag{50}$$

where v is the mean velocity in the gutters. Hence,

$$\mathcal{P} \sim \eta_w v^2 L_g. \tag{51}$$

By conservation of mass, the volume of water that is emptying in the neck region per unit of time should be equal to the flow rate in the gutters. Therefore, we must have

$$\partial_t \Omega_1 = v e^2 \tag{52}$$

with Ω_1 given by equation (31) that is recalled here,

$$\Omega_1 = 2\int_0^b h(x,t)e(x)\mathrm{dx} - \int_0^{\mathrm{b}} \frac{\pi \mathrm{e}^2(\mathrm{x})}{4}(\sqrt{1+\partial_{\mathrm{x}}\mathrm{h}^2}-1)\mathrm{dx}. \tag{53}$$

Then, the viscous dissipation power is

$$\mathcal{P} \sim \frac{\eta_w L_g}{e^4}\left[\partial_t \Omega_1\right]^2 \tag{54}$$

In order to take into account all the approximations that we make to express this viscous dissipation power, we define an adjustable parameter K such that

$$\mathcal{P} = K\frac{\eta_w L_g}{e^4}\left[\partial_t \Omega_1\right]^2 \tag{55}$$

We replace the expression $h(x,t) = h_0 p(x/b)$ in equation (55) such that we get,

$$\mathcal{P} = K\frac{\eta_w L_g}{e^4}\left[\partial_t\left(2\int_0^b h_0 p(x/b)e(x)\mathrm{dx} - \int_0^{\mathrm{b}} \frac{\pi \mathrm{e}^2(\mathrm{x})}{4}(\sqrt{1+\frac{\mathrm{h}_0^2}{\mathrm{b}^2}\mathrm{p}'^2(\mathrm{x/b})}-1)\mathrm{dx}\right)\right]^2. \tag{56}$$

In equation (56), all terms are constant in time such that the power verifies,

$$\mathcal{P} = K\frac{\eta_w L_g}{e^4}\partial_t^2 h_0\left[2\int_0^b p(x/b)e(x)\mathrm{dx} - \int_0^{\mathrm{b}} \frac{\pi \mathrm{e}^2(\mathrm{x})}{4}\frac{\mathrm{h}_0\mathrm{p}'^2(\mathrm{x/b})}{\mathrm{b}^2\sqrt{1+\mathrm{h}_0^2\mathrm{p}'^2(\mathrm{x/b})}}\mathrm{dx}\right]^2. \tag{57}$$

For sake of simplicity, we note $I(h_0) = \left[2\int_0^b p(x/b)e(x)\mathrm{dx} - \int_0^{\mathrm{b}} \frac{\pi \mathrm{e}^2(\mathrm{x})}{4}\frac{\mathrm{h}_0\mathrm{p}'^2(\mathrm{x/b})}{\mathrm{b}^2\sqrt{1+\mathrm{h}_0^2\mathrm{p}'^2(\mathrm{x/b})}}\mathrm{dx}\right]^2$.

The excess surface energy per unit of time

The excess surface energy of the system per unit of time is obtained by calculating the time derivation of ΔS given by equation (43),

$$\partial_t E = \gamma \partial_t(\Delta S) \tag{58}$$

In equation (58), the interface profile expression $h(x,t)$ is replaced by $h_0(t)p(x/b)$ and the time derivative of the interface profile is $\partial_t h_0 p(x/b)$.

We have,

$$\partial_t(\Delta S) = -2\int_0^b \partial_t h_0 \left(1+\frac{1}{\cos\theta}\right) p\left(\frac{x}{b}\right) \mathrm{x} + 2\int_0^{\mathrm{b}} \pi \mathrm{e}(\mathrm{x})\partial_{\mathrm{t}}\mathrm{h}_0 \frac{\mathrm{h}_0 \mathrm{p}'^2(\mathrm{x/b})}{2\sqrt{1+\partial_{\mathrm{x}}\mathrm{h}^2}}\mathrm{dx} + (2(w-e)+\pi e)\partial_t(\Delta l) \tag{59}$$

with

$$(2(w-e)+\pi e)\partial_t(\Delta l) = \frac{2(w-e)+\pi e}{(w-e)e+\frac{\pi e^2}{4}}\left[2\partial_t h_0 \int_0^b p\left(\frac{x}{b}\right) e(x)\mathrm{dx} - \int_0^{\mathrm{b}} \frac{\pi \mathrm{e}^2(\mathrm{x})}{4}\partial_{\mathrm{t}}\mathrm{h}_0 \frac{\mathrm{h}_0 \mathrm{p}'^2(\mathrm{x/b})}{2\sqrt{1+\partial_{\mathrm{x}}\mathrm{h}^2}}\mathrm{dx}\right]. \tag{60}$$

We factor equation (61) by $\partial_t h0$ such that the equation writes,

$$\partial_t(\Delta S) = \partial_t h_0 F(h_0) \tag{61}$$

F being a function of h_0. Indeed, in all the terms of equation (61), the only parameter that varies with time is h_0.

The power balance

The power balance writes

$$\partial_t E = P \tag{62}$$

Therefore, we must have,

$$\partial_t h_0 F(h_0) = \frac{K\eta_w L_g}{e^4} I(h_0). \tag{63}$$

The numerical resolution of equation (62) reconstructs the time evolution of $h_0(t)$ as follows,

$$h_0(t+1) = h_0(t) + \frac{K\eta_w L_g I(h_0)}{e^4 F(h_0)} \tag{64}$$

with $h_0(0) = 0$.

The adjustable parameter K is set by adjusting the time evolution $h_0(t)$ predicted by the power balance with the experimental data in the "mechanical" devices in

which the geometric parameters (d_x, d_z, w and e) are well characterized. We find $K = 2.1 * 10^{-3}$. Figure 49 compares the model prediction to the experimental data.

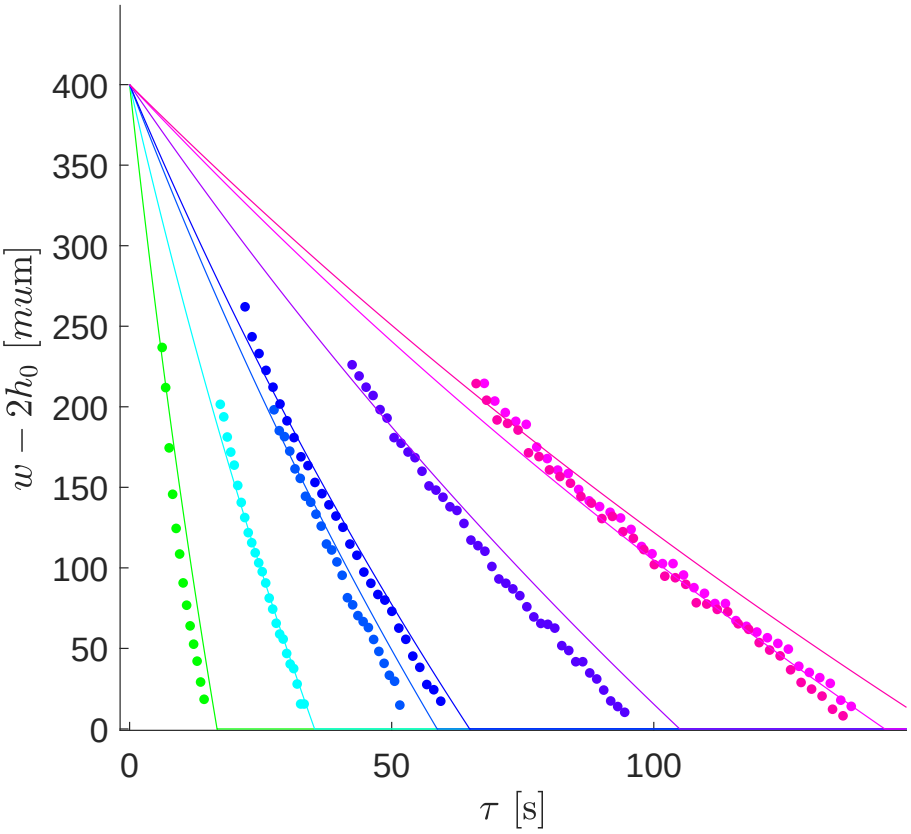

Figure 49: Time evolution of the neck width for a "mechanical" device in which $d_z = 5$ µm, $d_x = 400$ µm, $e = 30$ µm and $w = 400$ µm. The different curves correspond to droplets with varied gutters lengths $L_g = (17; 37; 60; 68; 100; 150; 155)$ µm ranked from the droplet that splits the quickest to the one that splits the slowest. The value of K is adjsuted to $2.1 * 10^{-3}$ in the power balance model to fit the experimental data (dots) with the theoretical predictions (line).

We set $K = 2.1 * 10^{-3}$ for the rest of the discussion and we compare the model to the experimental data obtained with the "thermomechanical" device. The parameter K can be regarded as a permeability coefficient by considering the gutters as pores that have a complex geometry. In this device, the value of d_z has been characterized as a function of the maximum temperature increase in the channel while the value of d_x is unknown. In order to compare the model with the time evolution of the neck width $w - 2h_0$, we need to adjust the value of d_x. For that, we define the dimensionless function N that calculates the difference between the model prediction $w - 2h_{th}(t)$ and the experimental profile $w - 2h_{exp}(t)$ of the neck width, normalized by the typical error of the image processing that we consider to be twice the pixel size, $e_{rr} = 10$ µm. N writes

$$N(d_x, d_z) = 4\frac{(h_{exp}(t) - h_{th}(t))^2}{e_{rr}^2}. \tag{65}$$

By minimizing function N (using the matlab function **fminsearch**), we can obtain

the values of (d_x, d_z) that best fit the experimental data. Figure 50 illustrates the model prediction for two experimental data sets corresponding to the same droplet at two different temperatures in the channel.

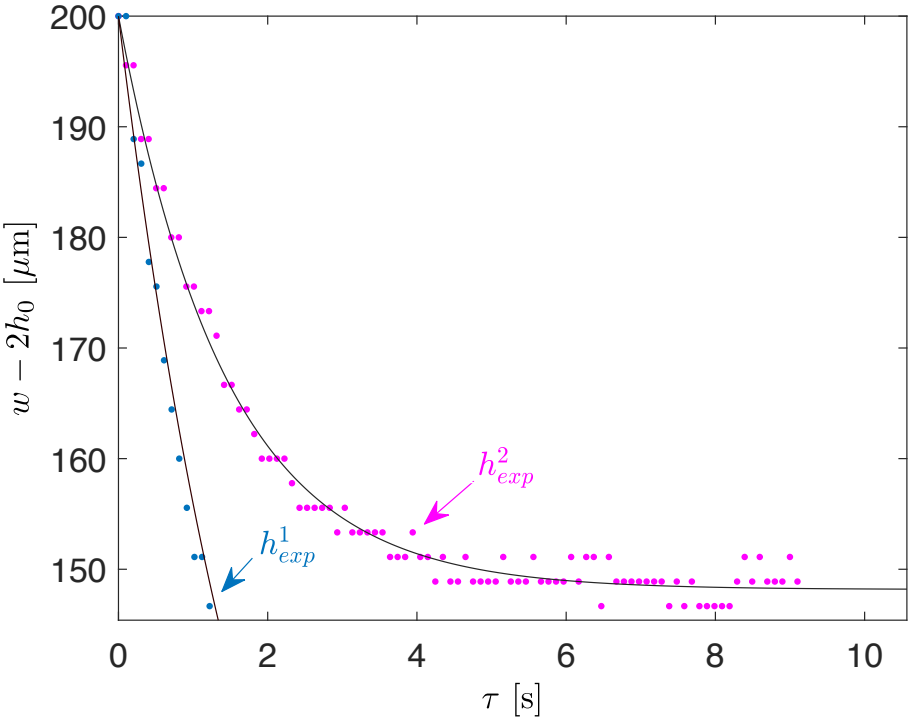

Figure 50: Time evolution of the neck width for experiments carried out in the "thermomechanical" device for two different temperatures: $T = 54°C$ (non-breaking droplet) and $T = 67°C$ (breaking droplet). The values of the geometrical parameters (d_z, d_x) are adjusted to fit the experimental data (dots) with the theoretical predictions (line).

By fitting the time evolution of the droplet deformation for a larger range of temperatures, see the Appendix page 114, we can plot the evolution of d_z and d_x as a function of the maximum temperature in the system. Figure 51a) plots the values of d_z that we implemented in the model to recover the dynamics of our experiment data. These values are compared to the ones that we have characterized in figure 22 in the chapter Materials and Methods. The characterization and the fitting values of d_z seem to be in pretty good agreement with one another, especially at high temperatures ($T > 60°C$). Similarly, figure 51b) shows the fitting values of d_x as a function of the maximum temperature in the system.

By plotting N as a function of d_x in the vicinity of the fitting value of d_x, we can estimate the sensitivity of the model to predict the variation of the channel topography. Figure 52a shows that when $N = N_{min} + 1$, we have $171 < d_x < 179$ µm, N_{min} being the minimum value of N. This means the sensitivity of the model on the parameter d_x is high (less than ten micrometers). The same considerations are made for d_z, see figure 52b. We find that the sensitivity of the model on the parameter d_z is hundreds of nanometers.

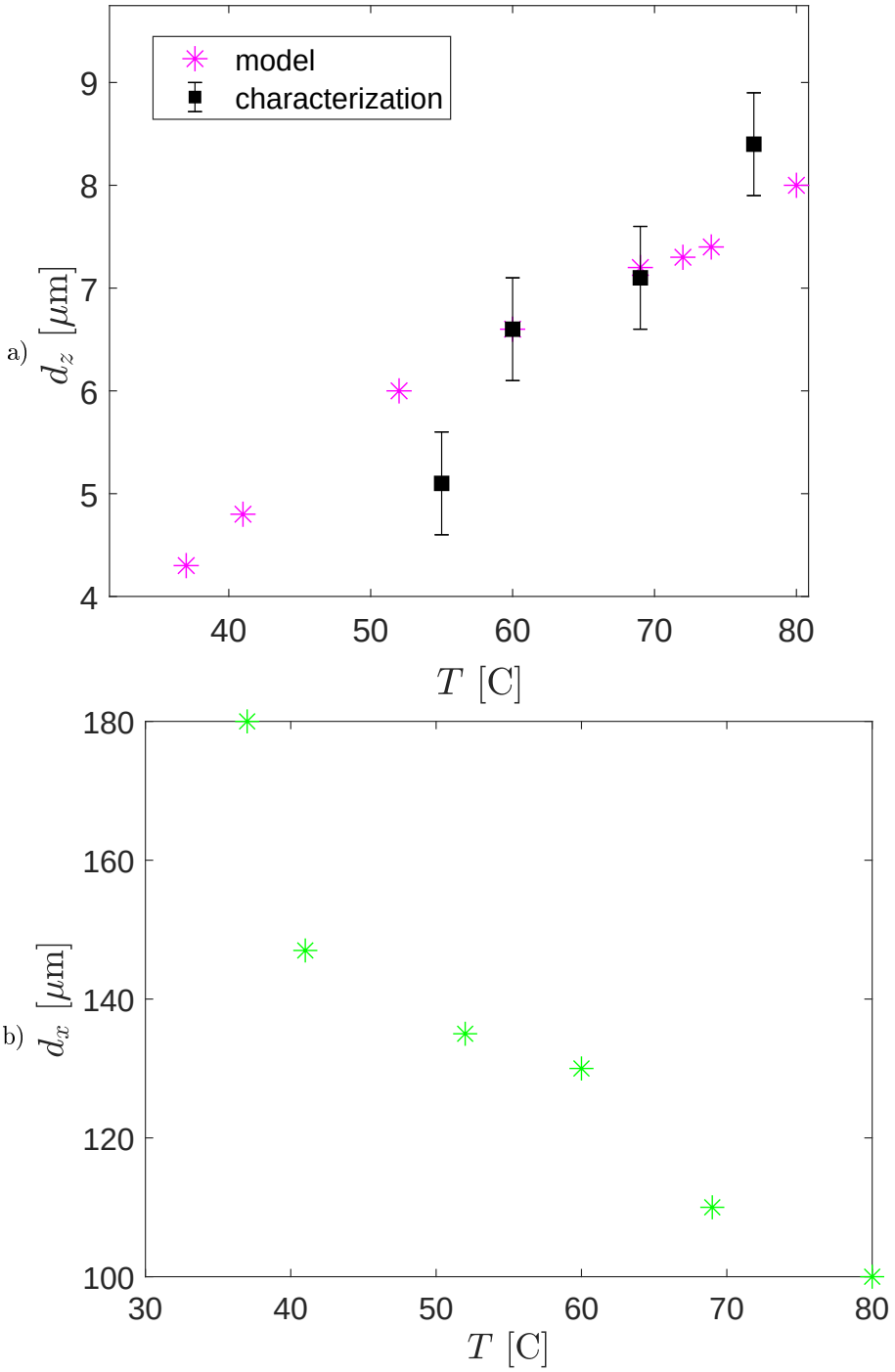

Figure 51: a) Fitting values of d_z (cross markers) that fit at best the theoretical model with the experiment profile of the time evolution of the neck width in the resistance device for different temperature increase. The predicted values of d_z (cross markers) are compared to the characterized values of d_z (square) in the chapter Materials and Methods. b) Fitting values of d_x that have been chosen to fit the experimental data with the model for different temperature increase.

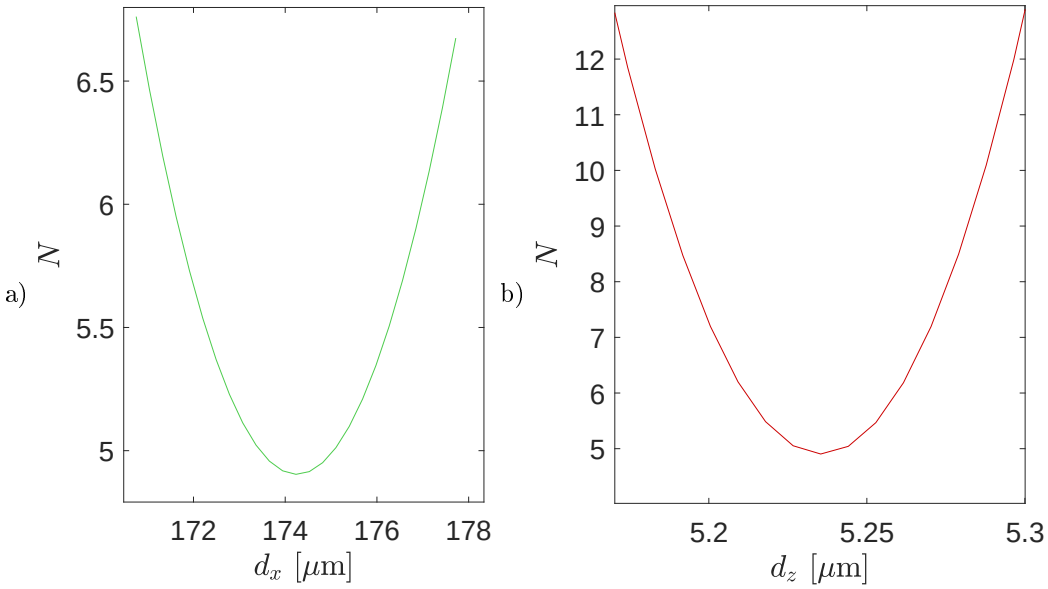

Figure 52: Evolution of the fitting error N as a function of: a) the x-axis extent of the gradient of confinement d_x b) the z-axis extent of the confinement gradient d_z near the best fitting values (d_x, dz).

20 Conslusions & Perspectives

- A local variation of the channel height of less than 20 % can lead to the droplet break-up when the latter is confined in a rectangular pore. By volume conservation, the external phase has to drain through the gutters towards the neck region when the droplet deforms.
- Even though, the droplet is 25 times mores viscous that the outer phase, the confinement modifies the distribution of the viscous stresses such that it is the less viscous phase that seems to set the dynamics of the droplet deformation.
- While a surface minimization seems to capture the droplet deformation features, a power balance based on scaling arguments manages to capture the dynamics of the deformation process. The model recovers that the linear breakup time scales with the length of the gutters L_g.
- The geometrical parameters of the confinement gradient d_z and d_x can be set as adjustable parameters in the power balance model such that their values could be extracted by fitting the model to experimental droplet deformation data. Consequently, the observation of in-plane droplet deformations could constitute a new technique to indirectly measure *in-situ* the local variation of a rectangular channel topography.

This work raises the following questions.

On the droplet deformation process

- We see that the droplet deformation is driven by the confinement gradient in the channel. However, we can wonder how the thermal Marangoni effect modifies the flows in both phases. What is the spatial extent of these flows ?
- Could the droplet deform if there were no gutters - in a cylindrical capillary tube for instance ? How would the deformation dynamics be altered in such a geometry ?

On the thermomechanical actuation

The indirect characterization of the PDMS thermal dilation seems to confirm that the channel contracts of approximately 20%. This large dilation is unexpected. One possible mechanism for this large deformation is the thermal dilation of nanobubbles that would be trapped in the polymer matrix and that would expand with temperature. Of course, other mechanisms are possible and we leave the interpretation of the thermal dilation of the channel as an open question.

Towards the fabrication of droplet shape soft-solid microstructures ?

Figure 53 shows a droplet deformed by a succession of confinement gradient indented in a system made out of a micro-milled mold. Figure 54 shows that by monitoring the topography of the channel, we can also deform a droplet made of diethylene glycol diacrylate mixed with 10% of 2-hydroxy-2-methylpropiophenone such that the latter can be solidified under a UV-exposition during the deformation process. Unlike the stop-flow lithography process that manages to build 2D structures with sharp edges - by illuminating a channel full of a photo-polymerisable solution with a UV lamp through a mask- [87], we achieve to fabricate 3D soft structures with a deformed droplet-like shape.

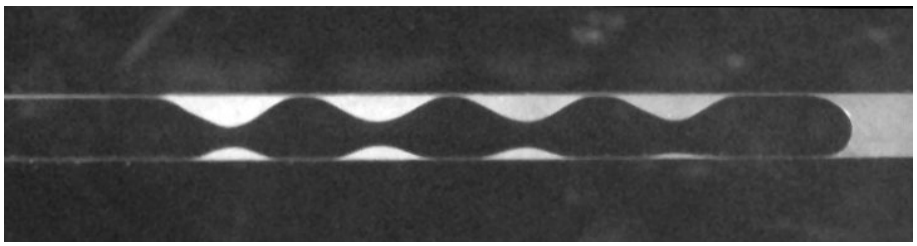

Figure 53: Droplet deformed by a succession of confinement gradient indented in a system made out of a micro-milled mold.

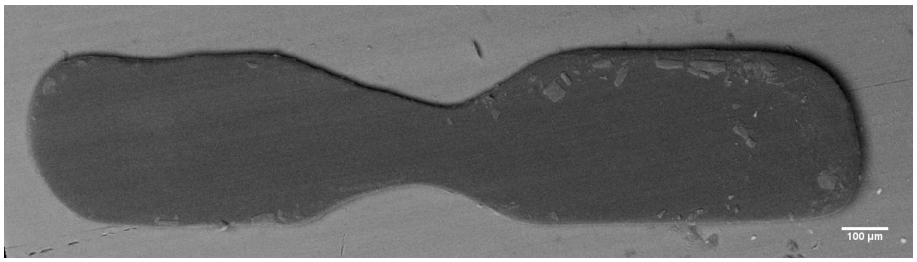

Figure 54: Solid droplet out of the channel using a scanning electron microscope (x120). The droplet is made of a solution of acrylate based monomers. The internal phase is a solution of diethylene glycol diacrylate with 10% 2-hydroxy-2-methylpropiophenone and the continuous phase is water with 2% SDS. The exposure time to the UV lamp is 500 ms.

Summary

In this chapter, we have investigated the droplet deformation induced by a local variation of the channel topography. This variation is induced by the local thermal dilation of the channel walls heated with a micro-patterned resistance that is located below the channel.
We show that the droplet deforms to minimize its surface energy when the latter undergoes the local confinement gradient until it can even break. The thermal Marangoni effect that is induced in the system does not seem to have a significant effect on the droplet deformation.
The dynamics of the droplet deformation seems to be set by the viscous dissipation of flows that drain through the gutters located at the four corners of the channel.
Observing the dynamics of the droplet deformation could constitute a new tool to indirectly measure the local variation of the channel topography, provided that this one can be assimilated to a symmetric and linear confinement gradient.

Part IV

Droplet Relaxation

In this chapter, we report the experimental study concerning the capillary relaxation of a droplet after the channel deformation is released. Initially pinched in its center (figure 55a), the droplet relaxes back to its plug-like shape minimizing its surface energy under the constraints imposed by the channel walls (figure 55b). During this relaxation process, the liquid contained in the central neck drains towards the extremities of the droplet. Surprisingly, the droplet relaxation that is also driven by surface tension and mediated by viscous dissipation, displays a dynamics that is very different from the droplet deformation. Figure 55c shows the spatio-temporal evolution for both the droplet deformation ($t_{on} < t < t_{off}$) and relaxation ($t > t_{off}$). t_{on} is the time at which the resistance is switched on and t_{off} is the time at which the resistance is switched off. While the rate of neck thinning during the deformation process is decreasing, the rate of neck thickening during the relaxation process is constant over time.

To explain the linear dynamics of droplet relaxations, we follow a theoretical approach that is different from the one we had for the droplet deformation. This approach integrates the role of the non-linear viscous dissipation in the dynamical meniscus of the neck [32]. This work allows us to show that classical models incorporating capillary driving with viscous dissipation employing geometrical invariance, whether translation or rotation cannot describe the relaxation in the intrinsically 3-dimensional geometry of the studied system. By "classical models", we refer to the ones that are used to describe for instance, the relaxation of a droplet in an infinite bath [74],[73], of a thin-liquid film that is invariant by translation [88, 89], of a droplet that has trapped a fluid pocket (a dimple) near a solid boundary [90, 91], of a droplet in a Hele-Shaw cell [92, 93] By considering the 3D problem, a scaling model incorporating dominant dissipation within the droplet menisci allows a full recovery of the self-similar droplet dynamics.

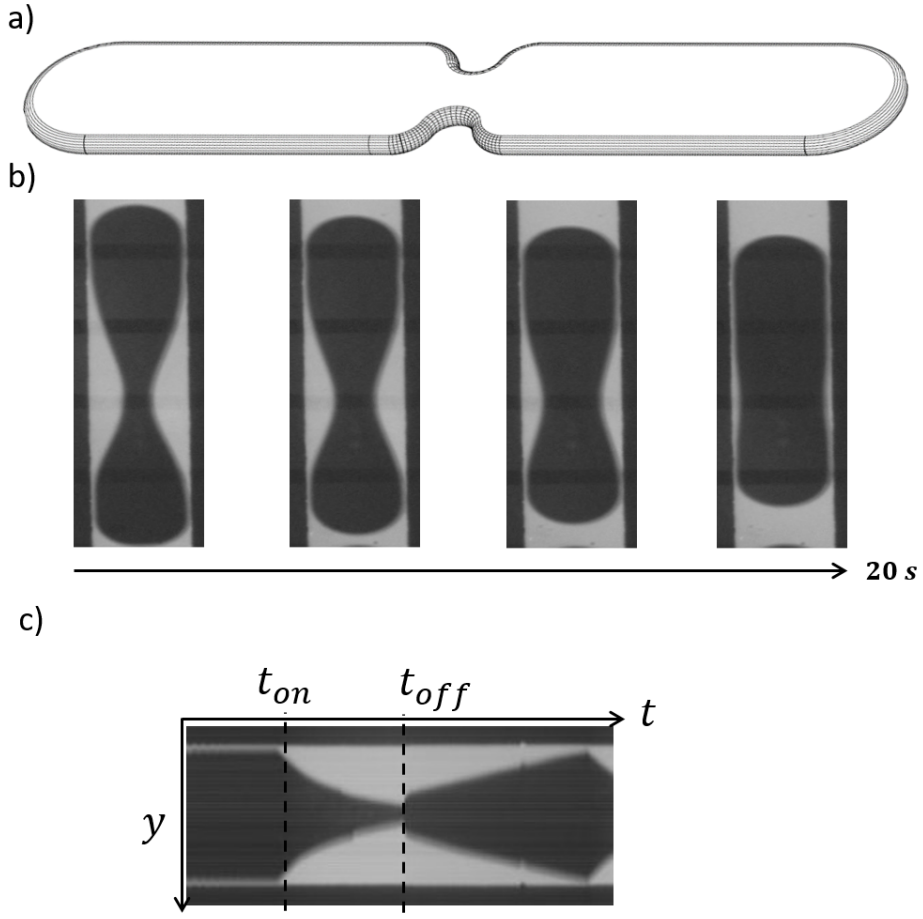

Figure 55: a) 3D illustration of the peanut-like shape droplet b) Snapshot of a 800 µm long droplet relaxation in a 200µm*30µm rectangular channel. The images are displayed every 5 seconds. c) Spatio-temporal evolution of the neck width during the droplet deformation $t_{on} < t < t_{off}$ and the droplet relaxation $t > t_{off}$. t_{on} is the time at which the resistance is switched on and t_{off} is the time at which the resistance is switched off.

Contents

21 Experimental observations

21.1 Definitions

This paragraph recaps the geometrical parameters of the problem, similar to the ones that are used to describe the droplet deformation. Figure 56 illustrates the droplet geometry. We define

- $h(x,t)$ as the distance between the channel side wall and the droplet interface
- L is the droplet length
- L_g is the length of the gutters

A sequence of droplet profiles is shown in Figure 56bi - iv). The neck is defined as the central portion of the peanut-like shape of the droplet. The extent of the neck in the x-axis is described by σ which corresponds to the the full width, half maximum of the interface profile. The extent of the neck in the y-axis is described by h_0, the maximum value of the interface profile. We observe that the timescale of the droplet relaxation is few seconds.

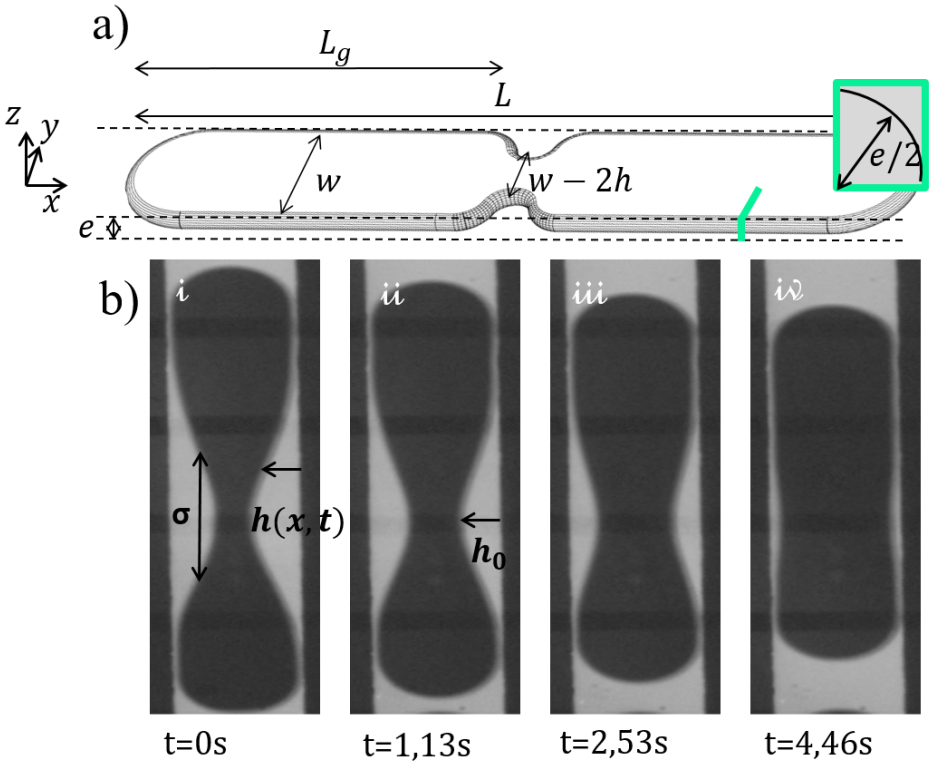

Figure 56: a) 3D schematic of the droplet geometry shaped by the confinement in the z-axis and in the y-axis. The undeformed droplet length is L; w and e are respectively the width and the thickness of the channel. The inset schematically shows the form of the gutters and the meniscus of radius $e/2$. (b) Snapshot of the relaxation of the droplet. The neck full width, half maxima is σ, and $h(x,t)$ is the distance between the channel wall and the deformed interface, of maximal value $h_0(t) = h(0,t)$.

In order to prepare the well-controlled, out-of-equilibrium droplet interfaces shown in Figure 57, we use a thermomechanical actuation. All the details of this process are provided in the previous chapter. When the heating resistors are switched off at time $t = t_{\text{off}}$, the PDMS relaxes and the droplet neck then returns to equilibrium. Figure 57a) displays the spatio-temporal evolution of the droplet cross-section at $x = 0$ for two different droplet lengths. Two regimes are observed. First, the neck relaxes abruptly over a typical time of hundreds of milliseconds and second, the relaxation proceeds more slowly and approaches equilibrium.

21.2 First temporal regime

The first temporal regime corresponds to the thermal relaxation of the PDMS dilation. During this regime, the channel thickness $e(x)$ increases such that the gradient of confinement disappears and a solid volume is suddenly released. The inset of Figure 57ai shows a zoom of this first relaxation, as well as a temperature profile taken

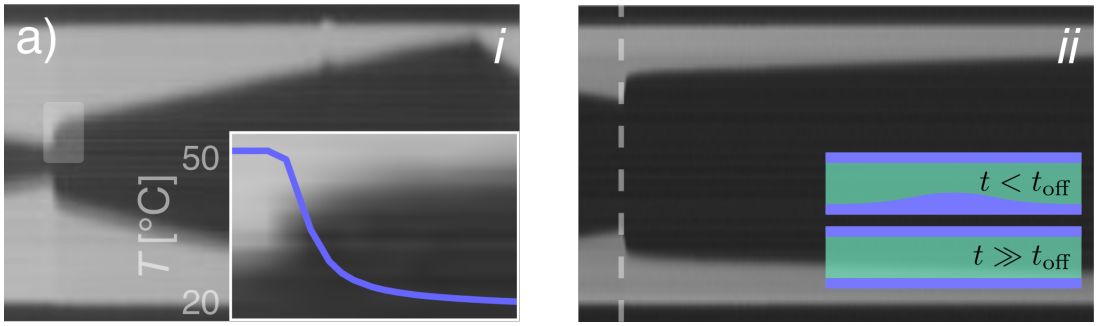

Figure 57: a) Spatiotemporal evolution of the neck for two droplets in a channel of section $e \times w = 30 \times 200$ µm^2 with lengths, *i*) $L_{\text{d}} = 510$ µm (elapsed time: 15s) and *ii*) $L_{\text{d}} = 1025$ µm (15 s). The insets show: *i*) experimental temperature versus time for the highlighted 1.4 s interval; *ii*) schematics of the thickness profile $e(x)$ around t_{off}, the latter quantity also indicated by the dashed vertical line.

with a infrared camera (Flir Camera, ATS). The first regime and the thermal relaxation in the device take place over the same period of approximately 200 ms (at most 500 ms). The newly available volume, schematically indicated in Figure 57a*ii*, is occupied by the phase that flows the most easily. A careful examination of both the volume released by the thermal homogenization and the increase of the inner phase volume in the neck suggests that *the inner phase flows more easily than the outer phase*. This result is consistent with our observations of the droplet deformation that suggested that it was the external phase that was setting the dynamics of the process, see the previous chapter.

Demonstration: The volume released by the thermal relaxation of the system can be extrapolated from the topography of the channel thermal expansion characterized in chapter Materials& Methods. The bottom channel topography is built from the maximum dilation height that has been experimentally calibrated.

For a temperature of $T = 60$ C that has been applied to a droplet in a 200 µm wide and 30 µm high channel, the volume (scheme 58) that is suddenly released by the thermal relaxation of the channel bottom layer can be approximated to $d_{\text{z}} * d_{\text{x}} * w \sim 5 * 100 * 200 \sim 10^5$µm^3 where d_{z} is the maximal dilation height of the bottom wall, d_x is the extent of the dilation in the x-direction that is assumed to be 100 µm and w is the channel width.

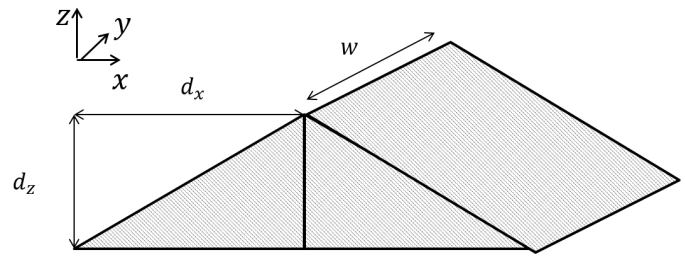

Figure 58: Volume of the bottom channel thermal expansion.

The increase of the inner phase volume in the neck region, can be estimated by subtracting the top view of a droplet before and after the switch off of the resistance and multiply the surface that derives from this substraction by the channel height. (see figure 59 which corresponds to a system that also verifies $T = 60$ C, w=200 µm and e=30 µm).

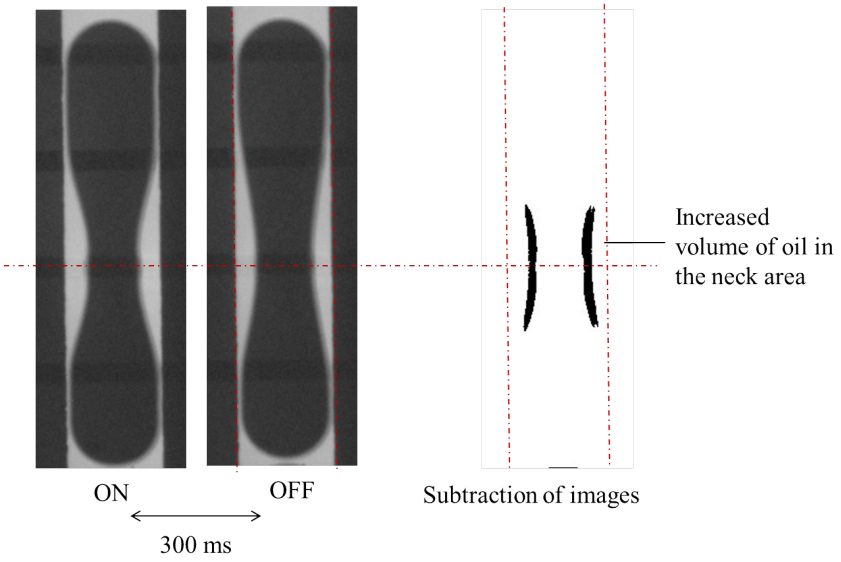

Figure 59: Calculation of the volume of oil, the inner phase, that occupies the free volume released by the thermal relaxation of the system.

The increased volume of the inner phase: $V_{\text{innerphase}} \sim 3,8.10^5 \mu m^3$ in the neck region, is of the same order of magnitude than the volume released by the thermal relaxation,V_{dilation}. This preliminary observation shows that because of the confinement, the inner phase ($\eta_i = 25 \times 10^{-3}$ Pa.s) flows more easily than the external phase ($\eta_o = 1 \times 10^{-3}$ Pa.s) - that has to flow through the gutters and possibly in the lubricating films. In the following, we consider that the dissipation occurs mainly in the external phase.

21.3 Second temporal regime

The second temporal regime is due to capillary driven flows. In Figures 60b) and c) we show the time evolution of the geometric features describing the neck: first, the neck extent along y, $h_0(t)$ and second, the neck extent along x, $\sigma(t)$ defined in figure 55c. For all the droplets that we have studied, we observe that $h_0(t)$, varies linearly with time over a significant period, and extrapolates to zero thickness at a time we call t_0. We note also that the relaxation time increases with the droplet length for a given channel geometry as demonstrated in Figure 60 - this is a signature of the dissipation of the liquid flowing in the gutters, see the previous chapter. Despite the small range of variation that is attainable with these experiments, the neck extent along x, $\sigma(t)$ varies with a power law that is captured by a scaling $(t_0 - t)^\beta$, with $\beta = 1/3$ providing a good description of the data; this power law is shown by the black line in this latter figure and is discussed in the next section.

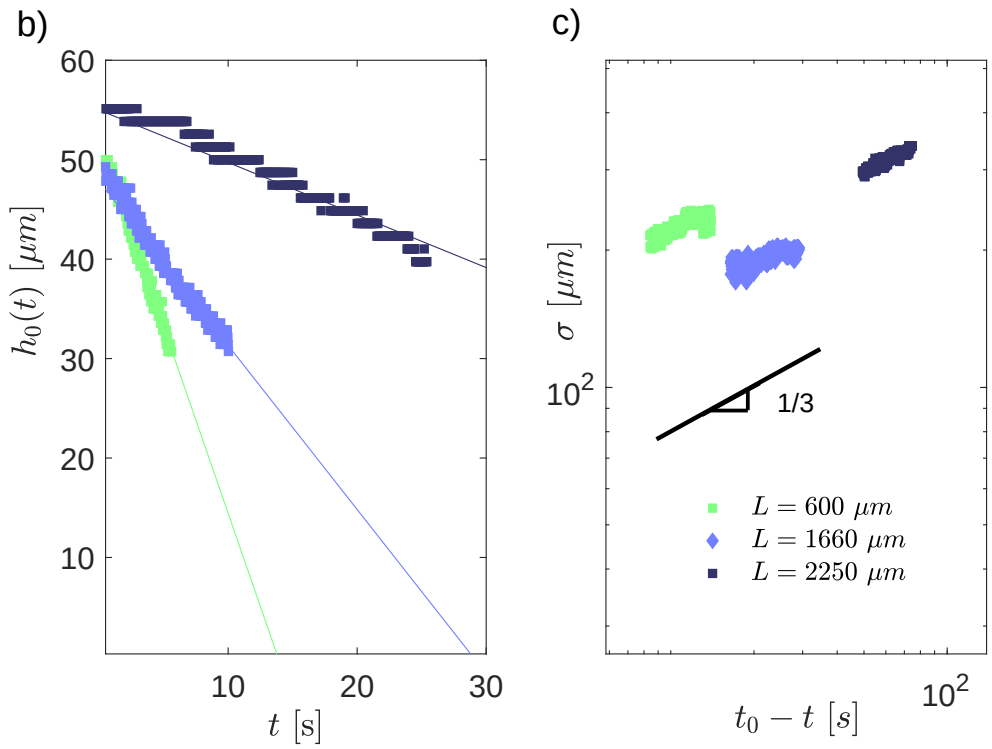

Figure 60: b) h_0 as a function of time for three droplet lengths and c) the corresponding time dependence of the x extent of the neck, σ.

Having briefly described the main features of the profile dynamics, we show in Figure 61a) the time evolution of the full raw profiles in the neck region at early times when $h_0(t) > e$. Based on the temporal evolutions of the neck features found in figure 57b) and c), we apply the scalings describing $h_0(t)$ and $\sigma(t)$ to the entire profiles of

Figure 61 a). Figure 61 b) thus depicts the rescaled curves of $h(x,t)/\tau$ as a function of $x/\tau^{1/3} \equiv u$, where we define $\tau = t_0 - t$. The interface profile $h(x,t)$ writes, in a self-similar way [94, 89, 95]:

$$h(x,t) = \tau^{\alpha} f\left(\frac{x}{\tau^{\beta}}\right) \tag{66}$$

where $\tau = t_0 - t$, $u = \frac{x}{(t_0-t)^{\beta}}$.

f is defined as the master curve on top of which all the interface profiles over time collapse after rescaling (Figure 61 (b)). Experimentally, we find a good quantitative agreement for $\alpha = 1$ and $\beta = 1/3$.

At late times, when $h_0(t) < e$, the interface profile does not follow very well the same self-similar analysis, see the Appendix page 115.

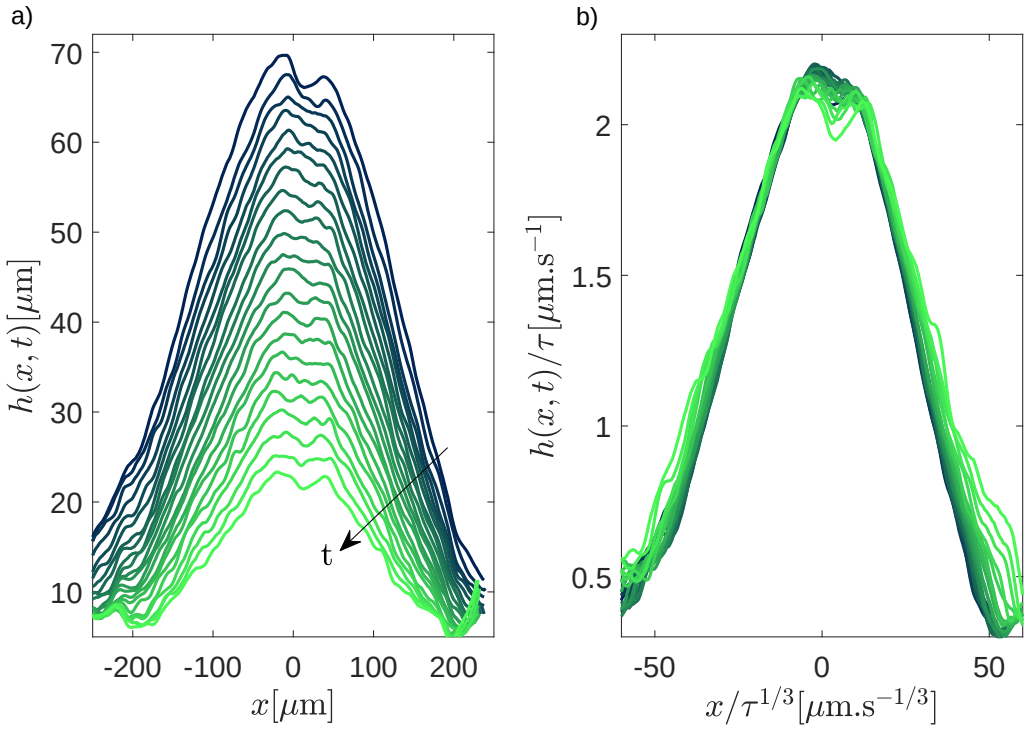

Figure 61: a) Interface profile $h(x,t)$ at the level of the neck over time. Dark blue plots illustrate the neck profiles at early stages and light green plots show the later stages; the total elapsed time is 6.5 s and the droplet length was $L = 800$ µm, with $e = 30$ µm and $w = 200$ µm. b) The same profiles of the central droplet interface after having rescaled the y-axis by $t_0 - t$ and the x-axis by $(t_0 - t)^{1/3}$.

Robustness of the exponent β:

In figure 61, the self-similar analysis shows that $\beta = 1/3$, also suggested by the time evolution of σ in figure 60c, is a good candidate to rescale the horizontal extent of the interface profile. Yet, a large range of β seems to give a good agreement with the experimental data as illustrated in figure 62.

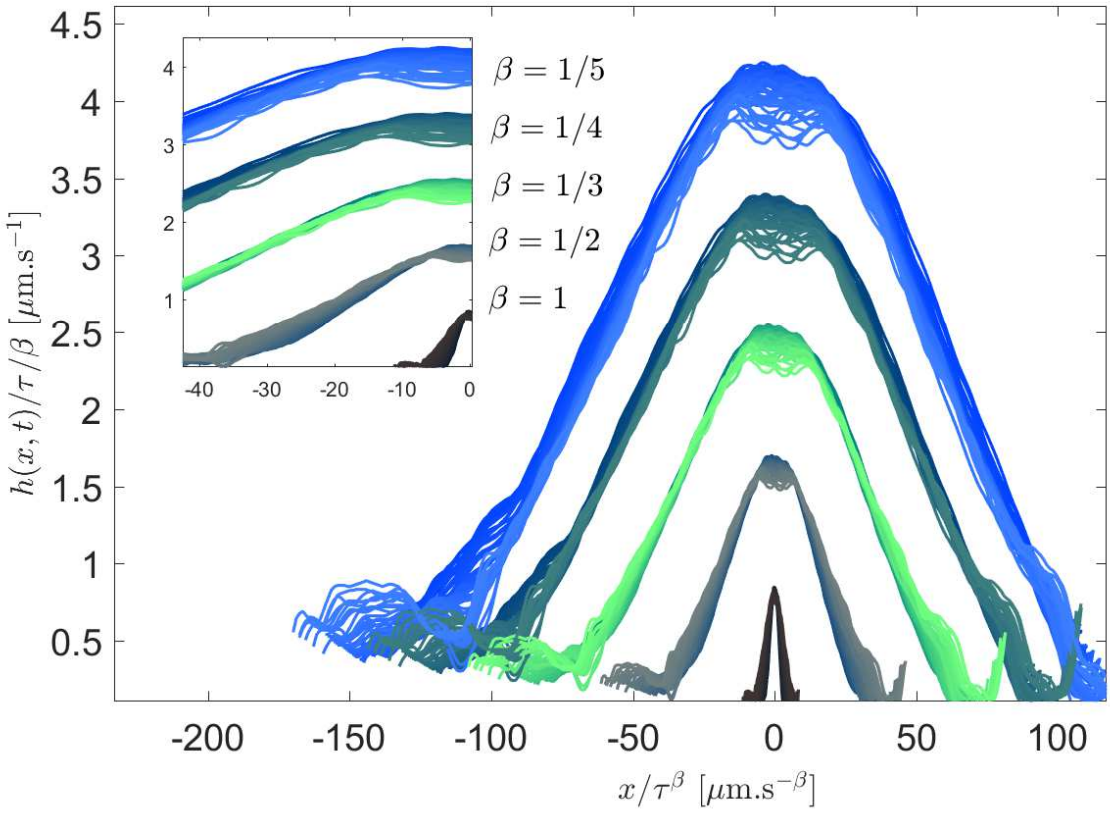

Figure 62: Self-similar profile of the interface after having rescaled the y-axis by τ and the x-axis by τ^{β} with $\beta = 1,\ 1/2,\ 1/3,\ 1/4,\ 1/5$. For more acuity, the interface profile are respectively mulitplied by 5, 4, 3, 2 and 1.

Since the self-similar analysis does not enable us to discriminate in a robust manner the values of β, we look at another parameter that varies also as a function of β: the volume of water that is trapped in the neck region $\Omega(t)$. This volume $\Omega(t)$ is approximately

$$\Omega(t) = 2e \int_{-c}^{c} h(x,t)dx. \tag{67}$$

where the bound c of the integral is chosen in between the maximum value of the neck extent in the x-axis and the extremity of the droplet. Thus, we ensure that $\Omega(t)$ covers the volume of water in the neck at any experimental time, t.

Using the self-similar expression of $h(x,t)$, the volume of the external phase in the neck becomes

$$\Omega(x,t) = 2e \int_{-c}^{c} \tau^{\alpha} f\left(\frac{x}{\tau^{\beta}}\right) dx. \tag{68}$$

Upon a change of variables, $u = x/\tau^{\beta}$, in the integral, Ω is given by

$$\Omega(x,t) = 2e\tau^{\alpha+\beta} \int_{-c}^{c} f(u)du. \tag{69}$$

where $\int_{-c}^{c} f(u)du$ is constant over time. The boundaries of the integral $[-c, c]$ can be considered as constant upon the change of variables since c has been chosen such c/τ^{β} is larger than the neck x-axis extent at any experimental time and since we consider that $h(x,t) = 0$ beyond $x = \pm c$.

Figure 63 shows the time evolution of $\Omega(t) \sim \tau^{\alpha+\beta}$. By fitting the curve with a function $m\tau^{p}$, for $p = [0; 1/5; 1/4; 1/3; 1/2; 1]$, we find that for $2 > p > 3/2$ and $p = 1$, corresponding respectively to $1 > \beta > 1/2$ and $\beta = 0$, the time evolution of $\Omega(t)$ is no longer in the errorbar of the experiment data.

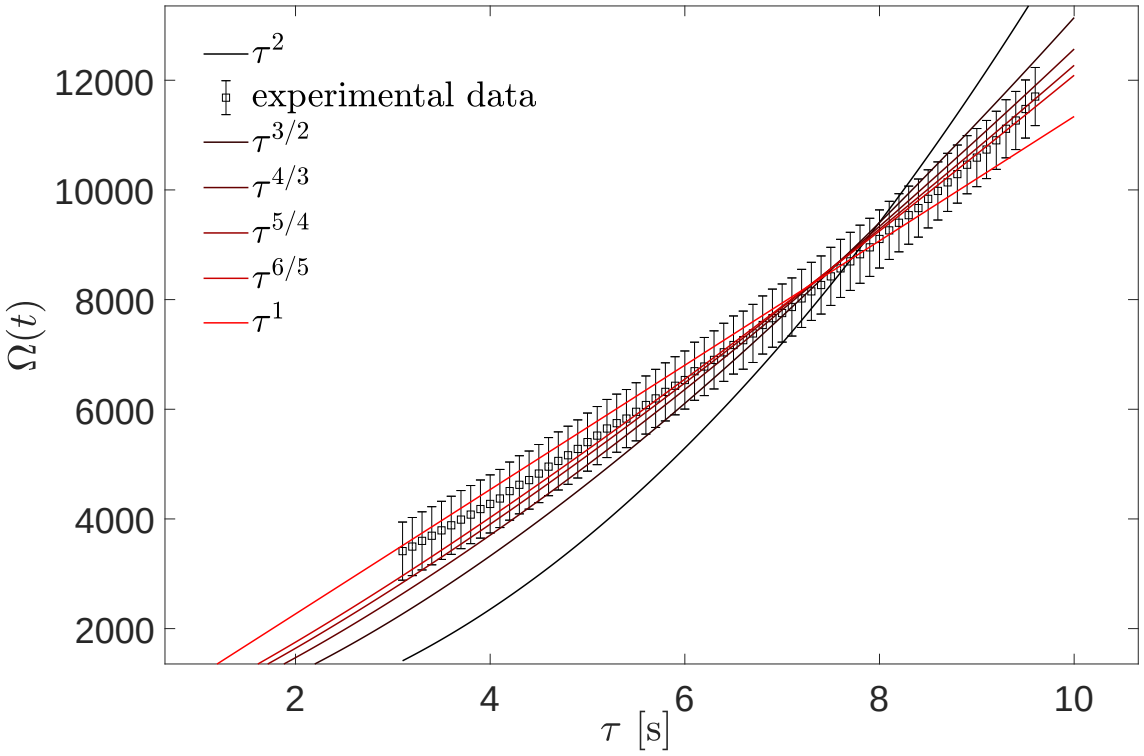

Figure 63: Time evolution of the volume of water in the neck $\Omega(t)$. Experimental data (rectangles) are compared to power evolutions $m\tau^{p}$ for for $p = [0; 1/5; 1/4; 1/3; 1/2; 1]$.

22 Model

In this section, we investigate the mechanisms that are at play in the droplet relaxation process. In order to do so, we identify the origin of the viscous dissipation in the system and we balance it with the capillary driving force induced by the initial curvature of the droplet interface.

In the previous section, we have seen that the dynamics of the droplet relaxation is very different from the one of the deformation process (discussed in chapter 3): the y-axis extent of the neck varies linearly over time and its x-axis extent seems to have a sublinear evolution with time τ. If we wanted to apply the surface minimization model of chapter 3 to the the droplet relaxation, we would have to integrate a varying

boundary b with time in the integrals of the excess surface expression, see equation 43. In addition, the power balance written for the droplet deformation would set only one constraint on α and β while we need a system of two equations to predict both values.

For all these reasons, we rather decide to investigate new theoretical approaches even though both processes deal with a liquid object that relaxes after having been driven out-of-equilibrium.

At first, we show that classical models as the lubrication equation in a 2D plane of invariance or the Brinkman approximation [90, 89, 92] are not appropriate to capture the self-similar exponents of the interface profile. Then, we write a model based on scaling arguments that consider the critical contribution of the droplet menisci and the gutters to the relaxation process. These arguments manage to recover the self-similar exponents of the droplet interface profile α and β.

22.1 First attempt: a thin-liquid film relaxation

At first sight, we consider the problem with invariance in z as considered, for example in [96, 89, 90]. This assumption discards the presence of the droplet menisci and the confinement of the external phase in the z-direction. This consideration is true at most at late times when the interface profile $h(x,t)$ becomes smaller than the cavity height, see figure 60 and 61.

In this approximation, the problem can be reduced to a 2D plane (x,y). The height of the flat film, at equilibrium, is considered to be e, the typical size of the gutters.

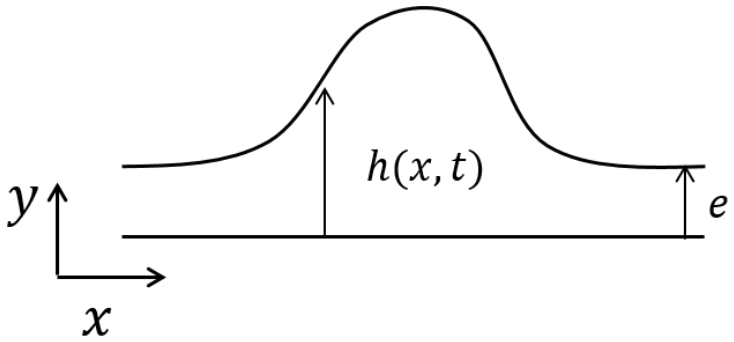

Figure 64: 2D approximation of the relaxation problem if we consider that the system is similar to a flat thin-liquid film infinite in the z-direction.

We assume that the y-axis deformation extent of the interface $h(x,t)$ is small compared to the scale σ of variations in the x direction, σ being the typical droplet length.

The velocity field in the external phase writes (v_x, v_y) in the (x,y) plane, where (v_x, v_y) scale respectively as (V_x, V_y). We consider the thin layer of fluid as incom-

pressible, so: $\partial_x v_x + \partial_y v_y = 0$ which thus gives on a scaling level $V_y \sim \frac{V_x h}{\sigma} << V_x$. The velocity can be considered as unidirectional in the x-direction (lubrication approximation, [97]).

In the external phase, the velocity v_x profile verifies the Stokes equation:

$$0 = -\partial_x p + \eta(\partial_{xx} v_x + \partial_{yy} v_x + \partial_{zz} v_x) \tag{70}$$

where $\partial_x p$ is the pressure gradient in the x-direction. In the system, the viscous dissipation scales as $\eta\left(\frac{V_x}{\sigma^2} + \frac{V_x}{h^2} + \frac{V_x}{e^2}\right)$. Since we only consider the period of time when, $h(x,t)$ becomes smaller than the channel height e, $h < e < \sigma$ ensures that the viscous dissipation prevails in the y-direction.

Hence, the Stokes equation can be simplified as:

$$\partial_{yy} v_x = \frac{\partial_x P}{\eta} \tag{71}$$

where η is the viscosity of the external phase and $\partial_x P$ is the pressure gradient driven by the curvature gradient at the surface of the thin film and scales as $\gamma \partial_x^3 h$ in the lubrication approximation.

We impose a no-slip boundary condition at the channel wall, $v_x = 0$ on $y = 0$. At the level of the advancing dynamical meniscus of the droplet, we impose a stress-free boundary condition, $\eta \partial_y v_x = 0$ at $y = h(x,t)$ (see the chapter Introduction), such that equation 71 gives:

$$v_x = \frac{\partial_x p}{2\eta}(y^2 - 2yh) \tag{72}$$

In these conditions, the flow rate per unit of length, $q(x) = \int_0^{h(x)} v(y)dy$, equals to $\frac{\gamma}{3\eta} h^3(x) \frac{\partial^3 h}{\partial x^3}$. The mass is conserved in the external phase such that $\partial_t h = -\partial_x q$. If we replace the expression of the flow rate per unit of length in the mass conservation equation, $h(x,t)$ obeys, [89, 90]:

$$-\frac{\gamma}{3\eta}\frac{\partial}{\partial x}\left(h^3(x)\frac{\partial^3 h}{\partial x^3}\right) = \frac{\partial h}{\partial t} \tag{73}$$

.

To solve equation 73 that is assumed to rule the interface profile, we use the self-similar expression of $h(x,t) = \tau^\alpha f(u)$ where $u = \tau^{-\beta} x$.

Resolution of the lubrication equation with a self-similar solution

Using the expression: $h(x,t) = \tau^\alpha f(\tau^{-\beta} x)$, we obtain the general expression of the temporal and spatial derivatives of $h(x,t)$:

$$\frac{\partial h}{\partial t} = \alpha\tau^{\alpha-1} f + \tau^{\alpha}\left(-\beta\frac{x}{\tau^{\beta+1}}\frac{\partial f}{\partial u}\right) \tag{74}$$

so

$$\frac{\partial h}{\partial t} = \alpha\tau^{\alpha-1} f - \beta\tau^{\alpha-1} u f' \tag{75}$$

and

$$\frac{\partial^n h}{\partial x^n} = \tau^{\alpha-n\beta} f^{(n)}(u). \tag{76}$$

In equation 73 that is supposed to rule the dynamics of relaxation, we have

$$\frac{\partial}{\partial x}\left(h^3\frac{\partial^3 h}{\partial x^3}\right) = 3h^2\frac{\partial^3 h}{\partial x^3} + h^3\frac{\partial^4 h}{\partial x^4}. \tag{77}$$

If we combine 73+75+76, the self-similar analysis of equation 77 gives

$$\alpha f - \beta u f' + \frac{\gamma}{\eta} f^2 f' f''' \tau^{4(\alpha-\beta)-(\alpha-1)} + \frac{\gamma}{3\eta}\tau^{4(\alpha-\beta)-(\alpha-1)} f'''' = 0. \tag{78}$$

For the equation to be right at all times, we have

$$3\alpha - 4\beta + 1 = 0 \tag{79}$$

which is not consistent with the experimental data (figure 61) that is much more in agreement with $\alpha = 1$ and $\beta = 1/3$. Indeed, if we take for granted that $\alpha = 1$ (figure 60b), this equation would give $\beta = 1$, which is inconsistent with the experimental data of the time evolution of $\Omega(t)$ and of the neck x-axis extension, $\sigma(t)$, on figures 60c and 63c.

Limitations of this approach

In the previous demonstration, we assumed that there was no shear in the z-direction. In reality, at early stages, $h(x,t)$ is of the same order of magnitude and even larger than the cavity height e, see 61. To take into account the contribution of the height e to the viscous dissipation in our projected 2D problem, we can amend the velocity profile using the Brinkman approximation [98, 99, 92].

Brinkman has shown that in a Hele-Shaw configuration, the viscous dissipation is diminished by a term that is proportional to the velocity v_x and to $k^2 = 12/e^2$, where e is the height of the cavity. The shear term then writes $\eta(\partial_y^2 v_x - k^2 v_x)$.

Brinkman approximation

In such approximation, Stokes equation writes

$$\partial_x p = \eta(\partial_{yy} v_x - k^2 v_x) \tag{80}$$

The general solution is then $v_x(y) = -\frac{1}{\eta k^2}\partial_x p + Ae^{ky} + Be^{-ky}$.

The no-slip boundary conditions, $v_x = 0$ on $y = 0$ and the stress-free boundary condition at the droplet interface, set $A = \frac{1}{\eta k^2(1+e^{2kh})}\partial_x p$ and $B = \frac{e^{2kh}}{\eta k^2(1+e^{2kh})}\partial_x p$

Volume conservation writes $\partial_t h = \int v_x dy$ such that we get

$$\partial_t h = \frac{-\gamma}{\eta k^2}\partial_x \left[\left(-h + \frac{1}{k}\tanh(hk)\right)\partial_x^3 h\right] \tag{81}$$

In order to recover the self-similar exponents α and β of $h(x,t)$ and carry out the self-similar analysis of the problem, we discard the term in tanh by making the approximation that $kh \gg 1$ which is at best true at early times when $h \gg e$. As a result, $h(x,t)$ verifies approximately

$$\partial_t h = \frac{\gamma}{\eta k^2}\partial_x(h\partial_x^3 h). \tag{82}$$

Combining equations 75+76 and 82, we obtain the following condition on the self-similar exponents: $\alpha - 4\beta + 1 = 0$ that is still not consistent with our experimental observations $\alpha = 1$ and $\beta = 1/3$. This equation would give $\beta = 1/2$ if $\alpha = 1$.

Besides, this model does not achieve to predict the values of both α and β. In the following section, we refine again our model by taking into account the viscous contribution of the droplet menisci to the relaxation dynamics.

22.2 Meniscus dissipation model

The fact that neither the lubrication equation 73 nor the Brinkman approximation 82 allows us to recover the dynamical features of droplets relaxation motivates an investigation of the viscous dissipation in the menisci. To take this dissipation into account, we write a scaling model in which we balance the capillary motion of the meniscus in the neck region and the viscous dissipation in the advancing/receding menisci of the droplet. This model, coupled to a volume conservation that takes into account the dissipation in the gutters, finally enables us to predict faithfully the self-similar exponents of the interface profile.

Our approach

In order to predict the self-similar exponents: α and β, a system of two equations is required. The spirit of the model that we write can be likened to the example of a tank of beer that empties through a tube, see the box.

Example of a tank of beer that empties under the effect of gravity and that is connected at its bottom to a small diameter tube.

Fist: a tank of water (without any foam)

It is assumed that the length of the end tiny tube L is long enough or e small enough to consider that the bulk viscous dissipation is larger in the tube than in the tank. The height of water in the tank is ruled by the balance between the gravitational force ($F_g \sim \rho g h \pi w^2$) and viscous forces. Among the viscous forces, we list the bulk viscous force in the tube ($F_v \sim \eta v L$), and the viscous dissipation at the level of the moving contact line at the interface water/air/wall. v corresponds to the mean velocity in the tube. If the radius of the tank is wider than the capillary length, the viscous friction at the level of the contact line can be neglected. The viscous dissipation that prevails is localized in the tiny tube.

Second: a tank of beer

To force the comparison, we add a foam on top of the liquid. We imagine that the bubbles of the foam are non-wetting. Therefore, the viscous force that prevails in the foam is due to the friction in the lubricating films between the wall and the bubbles of the foam [33, 32]. This force scales as $F_c = w\gamma C_a^{2/3}$ where w is the diameter of the tank and $C_a = \frac{\eta \partial_t h}{\gamma}$.

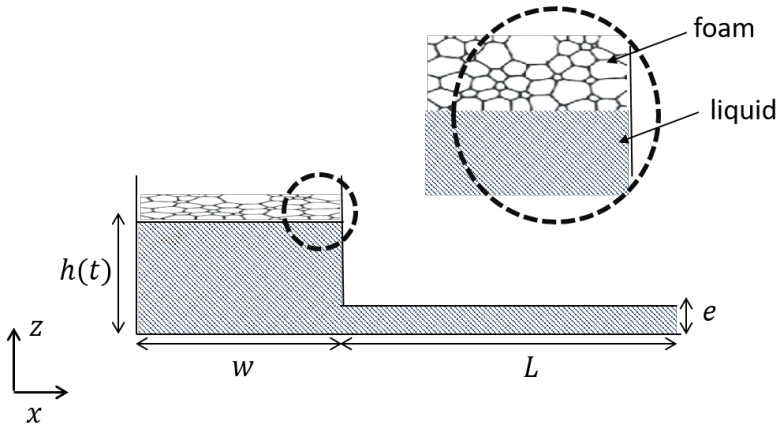

Figure 65: Scheme of a tank full of beer that is emptying under the effect of gravity and that is connected at its bottom to a small diameter tube. Geometrical parameters of the problem: L is the length of the tube, e is the diameter of the tube, w is the width of the tank, $h(t)$ is the height of beer. The beer is modelled as a liquid on top of which lays a foam.

The force balance in the system writes

$$F_g = F_v + F_c \tag{83}$$

We write the conservation of flow rate in the system such that $w\partial_t h = ev$.
The force balance writes: $\rho g h \pi w^2 = \gamma w \left(\frac{\eta \partial_t h}{\gamma}\right)^{2/3} + \eta \frac{Lw\partial_t h}{e}$.
The contribution of the foam to the overall dynamics has been evidenced for a sloshing tank by Gallaire et al. [100]. The authors show that sublinear capillary forces govern the friction at liquid-solid and liquid-liquid interfaces and amend the classical damped harmonic oscillator models for sloshing water even at the macroscale.
In the studied system, the tube is the equivalent of the gutters, the gravitational force must be replaced by capillary driving forces and the viscous friction in the moving foam with the tank wall can be compared to the viscous friction in the lubricating films at the level of the advancing menisci in the neck region.

Local force balance in the advancing menisci

Four menisci are advancing at the neck, both at the top and bottom walls for two sides of the neck. We note that four menisci are also receding at the droplet extremities (top and bottom walls at the two extremities), see figure 66. We assume that the velocities there are proportional to those in the neck.

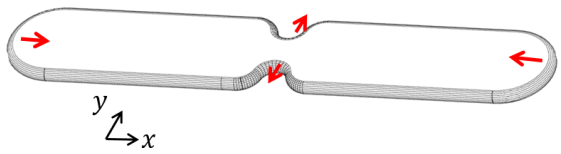

Figure 66: Direction of the moving droplet menisci in the neck region and at the extremities of the droplet.

Bretherton showed that, when a meniscus is advancing or receding near a solid boundary, most dissipation is in fact located in the *dynamical meniscus* [32, 33], which connects the flat lubricating film and the static meniscus with characteristic radius of curvature $2/e$ in the plane (y, z), see figure 67.

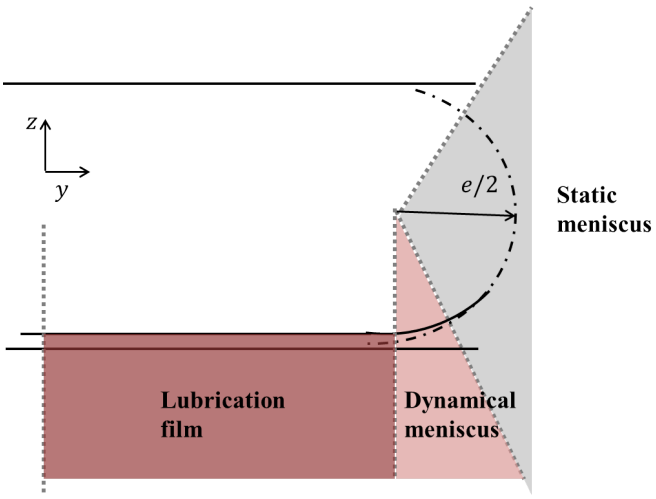

Figure 67: Geometry of a moving meniscus when a non-wetting droplet is pushed in a confined cavity. We define three zones: the static meniscus at the equator, $z = 0$, the dynamical meniscus close the wall and the constant thickness lubrication film that separates the liquid boundary from the wall.

The viscous drag force per unit length of the dynamical meniscus (in the x axis) scales with the capillary number, $Ca = \eta V \gamma^{-1}$ with V a typical interface velocity. Cantat [33] showed that $F_{\text{diss}} \approx \gamma Ca^{2/3}$.

The liquid velocity in the meniscus of the neck around the position $x = 0$ is $V \approx \partial_t h$ and the subsequent dissipative force in the dynamical meniscus writes $F_{\text{diss}} \approx \gamma \left(\eta\gamma^{-1}|\partial_t h|\right)^{2/3}$. The driving force is generated by the gradient of curvature along the interface, and writes in the limit of small slopes, and per unit length of the meniscus: $F_{\text{cap}} \approx \gamma e^2 \partial_x^3 h$, by considering that the dominant force is on the fluid between the meniscus and the wall, a space of typical lengthscale e.

Remark:

The dissipation, as written in the text, considers the main portion of the dissipation only which is around $x = 0$ where the fluid velocity is normal to the meniscus. There must be a transition between the flows normal to the advancing menisci in the neck and the flows parallel to the droplet interface in the gutters. We do not know what is the flow field distribution in the neck. However, we could defined an angle ϕ in the neck such that the meniscus dissipation would be moderated by the projection of the fluid velocity normal to the meniscus, see figure 68. In this case, the viscous drag per unit length of the dynamical meniscus would write $F_{\text{diss}} \approx \gamma(\cos\phi)^{2/3} Ca^{2/3}$, where ϕ is illustrated in figure 68. In the discussion, we only consider the section of the menisci where flows are normal to the interface and $F_{\text{diss}} \approx \gamma Ca^{2/3}$ per unit of length of meniscus.

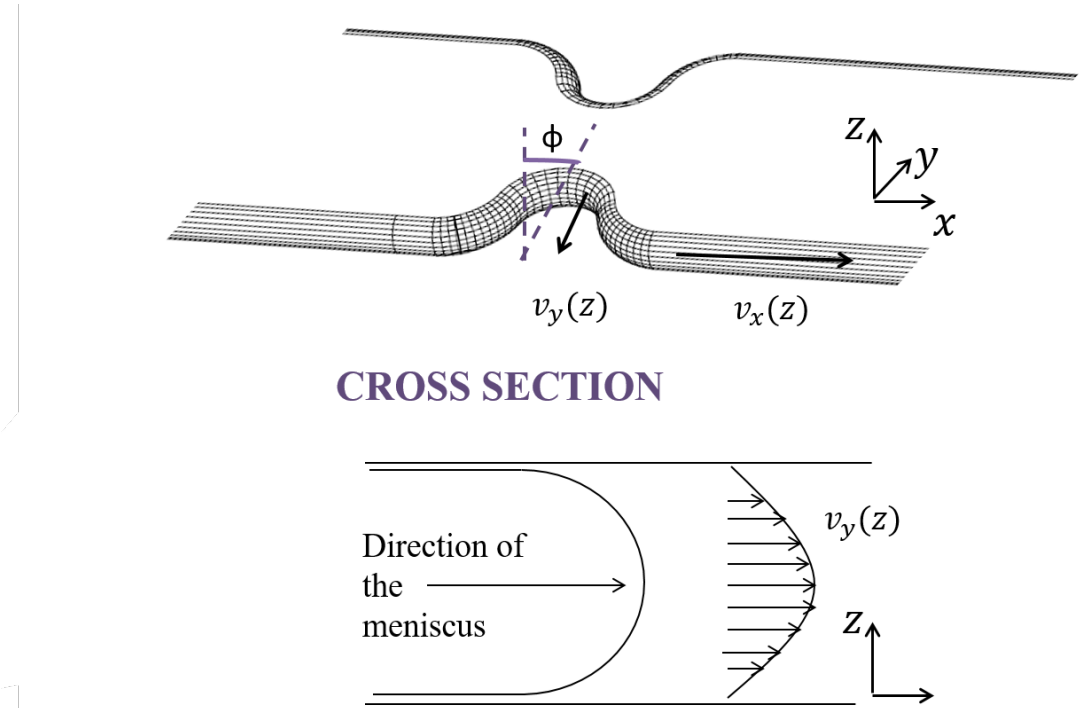

Figure 68: a) View of the advancing meniscus in the neck. Flows are normal to the interface at the center of the neck. The velocity fields write $v_y(z)$ while flows are parallel to the gutters, velocity fields then write $v_x(z)$. b) Cross-section of the advancing meniscus in the plane (y, z).

By balancing the driving and the dissipation forces, we find a relation between the temporal evolution of the profile and its current state:

$$\left(\frac{\eta}{\gamma}|\partial_t h|\right)^{2/3} \sim e^2 \partial_x^3 h \ . \tag{84}$$

According to the observed self-similarity, $h(x,t) = \tau^\alpha f\left(\frac{x}{\tau^\beta}\right)$, equation 84 becomes:

$$\left(\frac{\eta}{\gamma}\right)^{2/3} (-\alpha\tau^{\alpha-1} f + \beta u \tau^{\alpha-1} f')^{2/3} = e^2 \tau^{\alpha-3\beta} f'''. \tag{85}$$

For the equation to be true at all times,

$$\boxed{\alpha - 9\beta + 2 = 0} \tag{86}$$

In order to close the problem, we consider conservation of liquid volume flowing from the neck towards the droplet extremities through the gutters.

Volume conservation

The liquid that is expelled from the neck region during the relaxation process has to escape through the gutters by volume conservation. The volume $\Omega(t)$ of the external

phase in the neck writes

$$\Omega(t) = e \int_{-c}^{c} 2h(x,t)\mathrm{dx}. \tag{87}$$

The bounds of the integral are $-c$ and c and we take c, a constant that is larger than the maximum half-extent of the neck in the x-axis, see p. . Using the self-similar expression of $h(x,t)$, the volume of the external phase in the neck becomes

$$\Omega(x,t) = e \int_{-c}^{c} 2\tau^{\alpha} f\left(\frac{x}{\tau^{\beta}}\right) \mathrm{dx}. \tag{88}$$

Upon a change of variables in the integral, Ω is given by

$$\Omega(x,t) = 2e\tau^{\alpha+\beta} \int_{-c'}^{c'} f(u)\mathrm{du}. \tag{89}$$

We consider that the boundaries $[-c, c]$ are chosen such that $[-c', c']$ still cover the entire volume of the neck. We estimate that the volume lost per unit of time in the neck scales with the mean velocity v of the flow in the gutters times the typical cross-section of the gutters:

$$\frac{d\Omega}{dt} = \langle v \rangle e^2 \tag{90}$$

The mean velocity of the flow is estimated using the Stokes equation $\eta\Delta^2 v = -\partial_x P$. The flow is driven through the gutters by the over-pressure induced by the positive curvature at the center of the neck. As a result, the pressure drop is equal to the Laplace pressure gradient induced by the curvature of the neck $\partial_x P \sim \gamma\partial_x^2 h/L_g$ and established along the gutters length L_g through which the liquid flows. We consider that the flow in the gutters shears on the typical width of the gutters e. Given all these considerations, the mean velocity scales as:

$$\langle v \rangle = -\frac{\gamma\partial_x^2 h}{\eta L_g} e^2 \tag{91}$$

The volumetric flow rate in the gutters then scales as:

Consequently, equations (90) and (91) give:

$$\frac{d\Omega}{dt} = -\frac{\gamma\partial_x^2 h}{\eta L_g} e^4 \tag{92}$$

The second partial derivative of the expression of $h(x,t)$ is, according to the observed self-similarity:

$$\partial_x^2 h = \tau^{\alpha-2\beta} f''(u) \tag{93}$$

The curvature of the neck is considered at $x = 0$ (at the center of the droplet) where

$\partial_x^2 h = \tau^{\alpha-2\beta} f''(0)$. Using the expression (93), equation (92) then becomes:

$$\frac{d\Omega}{dt} = -\frac{\gamma \tau^{\alpha-2\beta} f''(0)}{\eta L_g} e^4. \tag{94}$$

Another expression of the volume lost in the neck per unit of time can be obtained by simply deriving equation (89),

$$\frac{d\Omega}{dt} = e(\alpha+\beta)\tau^{\alpha+\beta-1} \int_{c'}^{c'} f(u)\mathrm{du}. \tag{95}$$

where $\int f(u)du$ is a constant with time.
We balance equations (94) and (95) in order to find a constraint on the temporal self-similar exponents:

$$-\frac{\gamma \tau^{\alpha-2\beta} f''(0)}{\eta L g} e^4 = e(\alpha+\beta)\tau^{\alpha+\beta-1} \int_{c'}^{c'} f(u)\mathrm{du}. \tag{96}$$

Figure 69 displays the time evolution of the gutter length L_g. The latter expands of 25 µm which corresponds to only 2% of its mean length. In the following, we consider that L_g is constant over time.

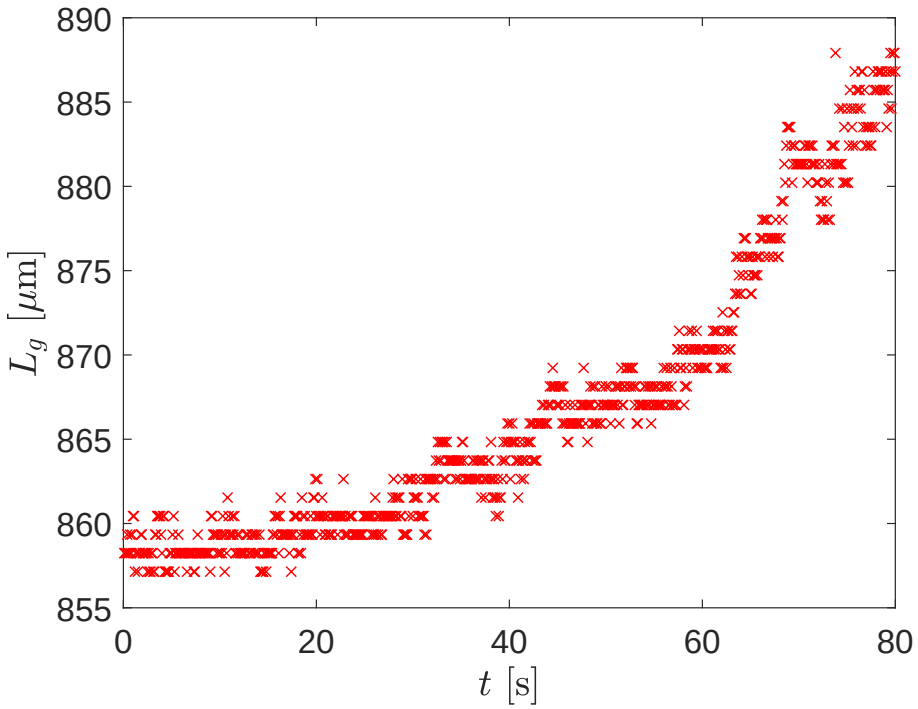

Figure 69: Time evolution of the gutter length for a 2100 µm long droplet in a 200 µm wide and a 30 µm high channel

In equation 96 all terms except from τ are independent on time. The exponents of τ must be equal:

$$\boxed{\alpha - 2\beta = \alpha + \beta - 1.} \tag{97}$$

Solutions for α and β

Equations 86 and 97 lead to the two values of self-similar exponents,

$$\boxed{\alpha = 1} \tag{98}$$

and

$$\boxed{\beta = 1/3} \tag{99}$$

consistent with the experimental data.

This agreement underlines the dominating effect of the menisci and gutters located at the confining walls on the drainage dynamics.

Characteristic drainage time

Finally, it is possible to define a characteristic drainage time to couple all of the experimental data $h_0(t)$. Further mass conservation consideration gives a relation between the velocity of the meniscus at the center of the neck and the mean velocity in the gutters $h\partial_t h \approx e\bar{v}$. As a result, the mean velocity of the neck meniscus can be written $\frac{h}{e}\frac{\Delta h}{\tau_\mathrm{d}} = -\gamma(\eta L_g)^{-1}e^2\partial_x^2 h$, where the time τ_d is the typical drainage time during which the neck size reaches the channel width $\Delta h \approx w$ with constant velocity. At first sight, from Figure 56, the curvature $\partial_x^2 h$ seems to be of the order of w^{-1}. In order to be more quantitative, figure 70 plots the curvature $\kappa = \partial_x^2 h(0,t)$ times w versus τ. It shows that κ is of the order of magnitude of w^{-1}.

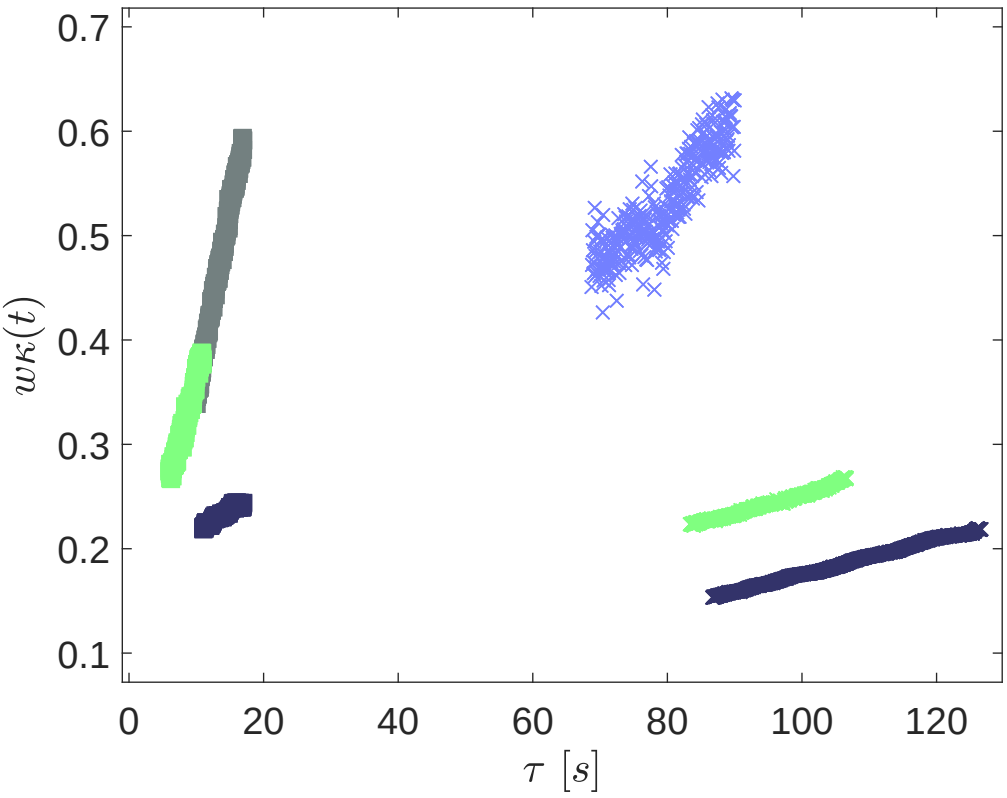

Figure 70: Plot of $w\kappa(t)$ versus τ for different datasets: (■) $L_g = 446\mu m$ $e = 30\mu m$ $w = 200\mu m$, (■)$L_g = 430\mu m$ $e = 30\mu m$ $w = 200\mu m$, (■)$L_g = 350\mu m$ $e = 30\mu m$ $w = 200\mu m$, (Λ)$L_g = 1000\mu m$ $e = 29\mu m$ $w = 400\mu m$, (Λ)$L_g = 850\mu m$ $e = 30\mu m$ $w = 400\mu m$, (Λ)$L_g = 950\mu m$ $e = 30\mu m$ $w = 400\mu m$.

We therefore define

$$\boxed{\tau_d = \frac{w\eta L_g}{\gamma e}.} \tag{100}$$

The time evolution of the neck height $h_0(\tau)$ can thus be represented using the dimensionless variables $\tilde{h}$ and $\tilde{\tau}$ with $\tau = \tau_d\tilde{\tau}$ and $h = e\tilde{h}$. These dimensionless variables are plotted on figure 71. Remarkably, all the data collapse onto a single linear curve, whatever the droplet length, channel width or cavity thickness. The collapse lies within an errorbar that is calculated in the Appendix 115. As such, the momentum conservation in the advancing neck coupled to a volume conservation in the gutters captures faithfully the experimental observations of the relaxation of the droplet for a wide range of length, channel height and width.

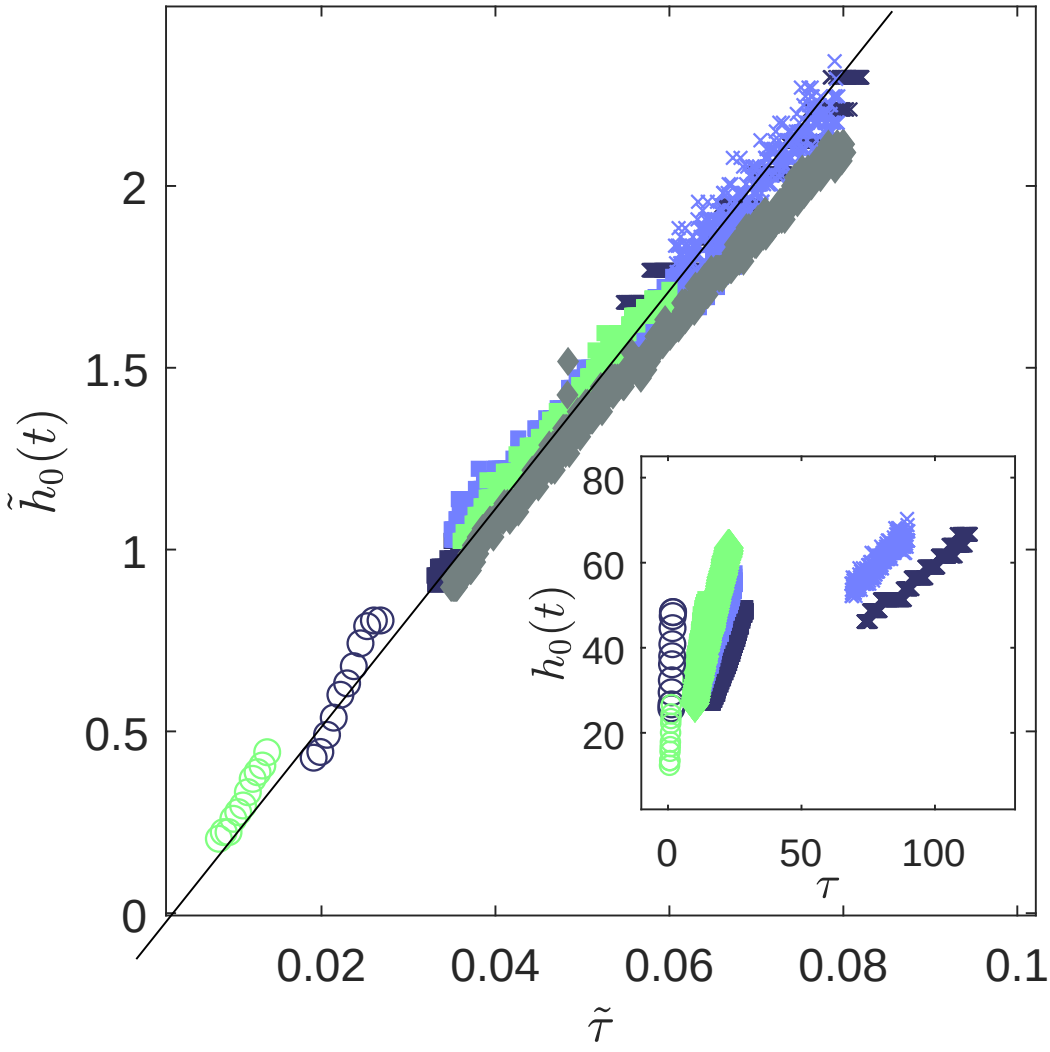

Figure 71: a) Plot of $h(0,t)$ versus τ b) Plot of dimensionless variables $\tilde{h}(0,t)$ versus $\tilde{\tau}$ for different sets of experiments: $*$ $L_{\mathrm{g}} = 1000\mu m$ $e = 29\mu m$ $w = 400\mu m$, $*L_{\mathrm{g}} = 850\mu m$ $e = 30\mu m$ $w = 400\mu m$, $\blacksquare L_{\mathrm{g}} = 750\mu m$ $e = 30\mu m$ $w = 200\mu m$, $\blacksquare L_{\mathrm{g}} = 549\mu m$ $e = 30\mu m$ $w = 200\mu m$, $\blacksquare L_{\mathrm{g}} = 350\mu m$ $e = 30\mu m$ $w = 200\mu m$, $\bullet L_{\mathrm{g}} = 260\mu m$ $e = 60\mu m$ $w = 200\mu m$, $\bullet L_{\mathrm{g}} = 360\mu m$ $e = 60\mu m$ $w = 200\mu m$.

23 Conclusion

To conclude, the 3D geometry of microfluidic droplets, shaped by the 2D confinement in height and in width gives rise to menisci and gutters of typical size imposed by the channel height. These objects play a major role in relaxation dynamics. Analytical descriptions based on the classical lubrication equations or Brinkman approximation do not achieve to recover the experimental observations. By contrast, we have predicted the relaxation dynamics with a scaling analysis considering capillary driving forces and viscous dissipation mainly in the gutters and menisci. Considering a resulting characteristic relaxation time of droplets depending on the physico-geometrical parameter of the channels, we fully collapse all the dynamics onto a single curve.

Summary

This chapter investigates the droplet relaxation to its plug-like equilibrium shape after the resistance is switched off.
We show that the thermal relaxation of the PDMS dilation occurs in a few hundreds of ms, much faster than the droplet relaxation that takes place over tens of seconds. The dynamics of the relaxation process is very different from the dynamics that we observe for the droplet deformation. Indeed, the rate of neck thickening is constant over time and the x-axis extent of the neck varies as $\tau^{1/3}$ where τ is the time distance from the end of the relaxation. The evolution of the droplet interface displays a self-simlar profile at early times.
The droplet relaxation is capillary-driven and is mediated by viscous dissipation. We write a scaling model that takes into account the Bretherton sublinear friction in the moving menisci of the droplet and the linear friction in the gutters. This model recovers the self-similar exponents of the interface profile.
Our study emphasizes the peculiar role of the droplet menisci in the dynamics of droplet relaxations and raises some questions:

- Why is the nonlinear friction in the moving meniscus evidenced in the droplet relaxation dynamics and not in the droplet deformation one ?
- Why does the x-axis extent of the neck varies with time in the relaxation process and not during the deformation process ?

Part V

Conclusion

In this manuscript, the response of a non-wetting droplet, confined in the rectangular section of a microfluidic channel, to a local variation of the channel topography has been investigated. The local confinement gradient, that can reversibly be induced in the channel with using a thermomechanical actuation, leads the droplet to deform. If the channel is deformed enough, the droplet can even break. The studied deformations are driven by capillary forces until the surface energy is minimized subject to the constraints imposed by the confining wall. This deformation is not instantaneous since it is mediated by the viscous dissipation that seems to be localized in the gutters at the four corners of the channel. A power balance equating the time derivative of the surface energy of the droplet and the viscous dissipation power manages to capture the time evolution of the droplet deformation. This model can be used to fit the experimental observation of the dynamics of the deformation process with the vertical and horizontal dilations of the channel as independent fitting parameters, with a micrometric resolution.

When the topography of the channel goes back to flat after the thermomechanical actuation is stopped, the droplet relaxes to its plug-like shape. Interestingly, the dynamics of this relaxation process is linear unlike the deformation process, the speed of which decreases over time. By coupling a force balance in the dynamical menisci of the relaxing droplet with a volume conservation of the external phase that has to flow through the gutters, we manage to recover the linear time evolution of the relaxation process. Lastly, a characteristic drainage time that depends on the physico-geometrical parameters of the system can be extracted from this study.

The relaxation dynamics of an initially out-of-equilibrium liquid/liquid interface has been studied for many decades[101, 91, 102]. Fundamentally in these studies, simply-modelled geometries lead to quantitative descriptions which can in turn lead to the revelation of molecular scale physics: disjoining pressure and slip length being examples [90, 89, 41]. In the geometrical configuration of this work, this small scale physics might not be revealed since flows occurrs mainly in the gutters that are tens of microns large. However, these two studies emphasize the dominating role of capillary forces at the micrometer scale that can even provoke droplet to break-up with a dilation of the channel height of just 15 %. They also emphasize the effects of the confinement on the droplet dynamics. For example, the role of the less viscous phase that has been demonstrated in plunging plates [96] or in bouncing and splashing droplets [103, 104, 105], wherein the less viscous phase is strongly confined, is one more time illustrated. Similarly, the importance of the dynamical menisci of the droplet [32], is once again evidenced.

As a perspective, since the boundary conditions at the droplet interface has been proven to modify the viscous friction force in these menisci [33], we might wonder if we would observe a change in the droplet relaxation dynamics if we rather added insoluble surfactants to the system. We might also wonder what flow patterns are induced by the thermal surface tension gradient at the droplet interface during the deformation process.

Appendix

Droplet deformation

Early times of the self-similar analysis

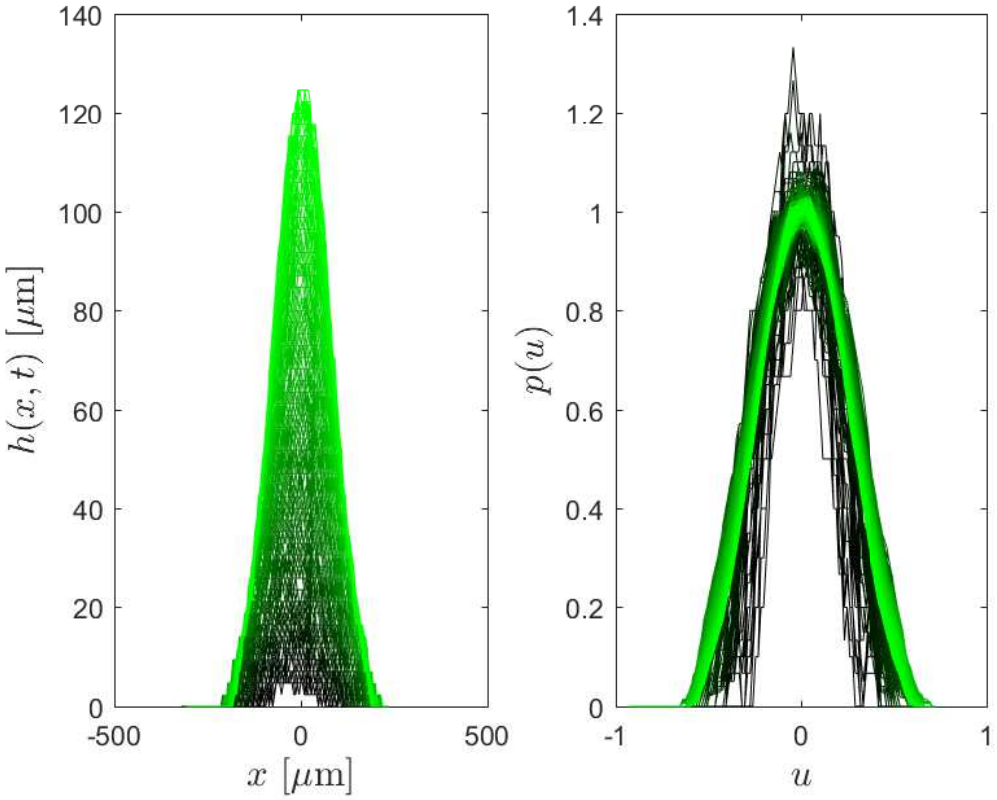

Figure 72: (a) Interface profile $h(x,t)$ at the level of the neck during the entire process of the droplet deformation. b) Associated self-similar functionp_r as a function of $u = x/b$.

Approximative estimation of the time of the droplet break-up in the case of a Marangoni effect

In the lubricating films (top, bottom, sides of the droplet), the length over which there is a flow shear is h_∞ (see the chapter Introduction). In the gutters, the distance over which flows shear is typically the size of the gutters that scales as e. In the droplet, at the level of the meniscus, flows also typically shear over the height of the cavity e. We can thus estimate the velocity of the Marangoni flow in each regions of the system. For the calculations, we take $e = 30$ µm and $h_\infty = 20$ nm. The viscosity of mineral oil is 25 mPa.s^{-1} and the viscosity of water is 1 mPa.s^{-1}.

- In the lubricating film

If we note V_{int} the velocity of the interface, the tangential stress continuity at the interface writes

$$\eta_o \frac{V_{int}}{e} - \eta_w \frac{V_{int}}{h_\infty} = \frac{d\gamma}{dx} \tag{101}$$

The ratio $\eta_o/e \sim 25{*}10^{-3}/(30{*}10^{-6}) \sim 10^3$ while the ratio $\eta_w/h_\infty \sim 10^{-3}/(20{*}10^{-9}) \sim 10^6$. We conclude that the velocity at the interface $V_{int} \sim d\gamma/dx * h_\infty/\eta_w \sim 10^{-7}$ m/s and that we can neglect the velocity of the Marangoni flows in the lubricating films.

- In the gutters

  The tangential stress continuity writes

$$\eta_o \frac{V_{int}}{e} - \eta_w \frac{V_{int}}{e} = \frac{d\gamma}{dx} \tag{102}$$

  The interface velocity is then $V_{int} = \frac{d\gamma}{dx}\frac{e}{\eta_o - \eta_w} \sim 30{*}10^{-6}/(24{*}10^{-3}) \sim 10^{-3} m/s$.

Figure 73 summarizes the distribution of the velocity at the droplet interface in a cross-section view. The figure illustrates that the velocity is nearly zero (see previous discussion) in the lubricating films and maximum in the gutters.

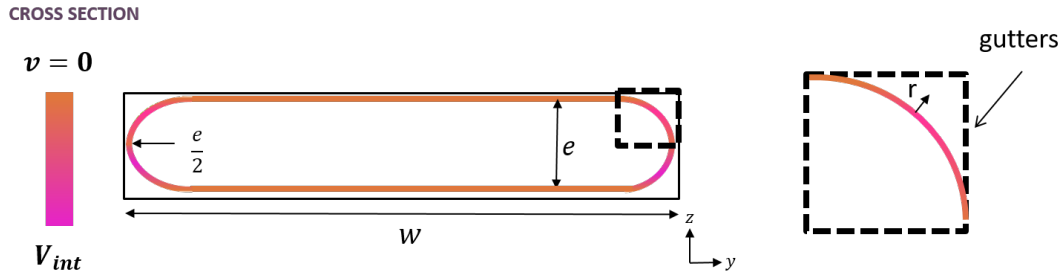

Figure 73: Scheme of the velocity distribution at the interface of the droplet in a cross-section view. The figure illustrates that the velocity is zero in the lubricating films and maximum in the gutters.

In order to estimate a time of break-up, we calculate the flow-rate of water in the gutters induced by the thermal Marangoni effect.

We define r as a radial coordinate that verifies $y^2 + z^2 = r^2$, see figure 73. r identifies the distance of a fluid element from the droplet interface in the diagonal of the gutter. The velocity field in the gutter that stems from the Marangoni effect derives from the integration of the boundary condition at the interface written in equation (102). We assume that the velocity filed in the gutter scales

$$v(r) \approx \frac{1}{\eta_o - \eta_w}\frac{d\gamma}{dx} r + A \tag{103}$$

A being a constant that must be determined by the boundary conditions.

At the droplet interface $v(0) = V_{int}$, at the walls, $v(e) = 0$. Therefore, the velocity field writes

$$v(r) \approx \frac{1}{\eta_o - \eta_w} \frac{d\gamma}{dx}(e - r) \tag{104}$$

The mean velocity in the gutter then scales as

$$\mathcal{V} \approx \frac{1}{e} \int_0^e \frac{1}{\eta_o - \eta_w} \frac{d\gamma}{dx}(e - r)dr \tag{105}$$

so

$$\mathcal{V} \approx \frac{1}{2e} \frac{1}{\eta_o - \eta_w} \frac{d\gamma}{dx} \tag{106}$$

Considering that the typical total section of the gutters is e^2, the flowrate of water that enters in the neck per unit of time scales as $\mathcal{Q} \sim \frac{e}{2} \frac{1}{\eta_w} \frac{d\gamma}{dx} \sim 10^{-5} * 10^2 * 0.2 \sim 10^{-4}\text{m}^3.\text{s}^{-1}$.

In particular, we note that equation (106) largely overestimates the mean velocity since it takes as a typical length scale the channel height, e, which is only true near the center of the gutter. In all other places, the gutter height is smaller. Indeed, in a rectangular channel cross-section, the interface velocity varies from the one given by eq. (102) down to the one given at the lubrication film which is set to zero. A way to take into account the complex contribution of these boundaries to the flow field is to define a permeability coefficient α. This coefficient is commonly defined in the studies that deal with flows in porous media []. The flow-rate is then amended by α and we have $\mathcal{Q} \sim \frac{\alpha e}{2} \frac{1}{\eta_o - \eta_w} \frac{d\gamma}{dx} \sim \alpha 10^{-3}$.

The volume of water in the neck is approximately $bwe \sim 10^{-12}$ µm^3. Therefore, we can define a time of break-up associated with the thermal Marangoni effect that is around

$$\frac{wbe}{\mathcal{Q}} \sim \alpha^{-1} 10^{-9} s \tag{107}$$

In order to recover the time of break-up that is observed in our experimental data, α should be of the order of magnitude 10^{-10}. This value is very far from the typical value of the permeability coefficient that is calculated in the literature for porous media -in foams this coefficient is of the order of magnitude 10^{-4} [106]. In addition, the fact that the droplet reaches an equilibrium state while the tangential stress $\frac{d\gamma}{dx}$ is maintained at the interface suggests that the Marangoni flow can hardly be the prevailing mechanism in the system. In the next section, we prove that the local channel dilation is the main motor of the droplet deformation.

Best fit of the droplet deformation dynamics data in the "resistance" system

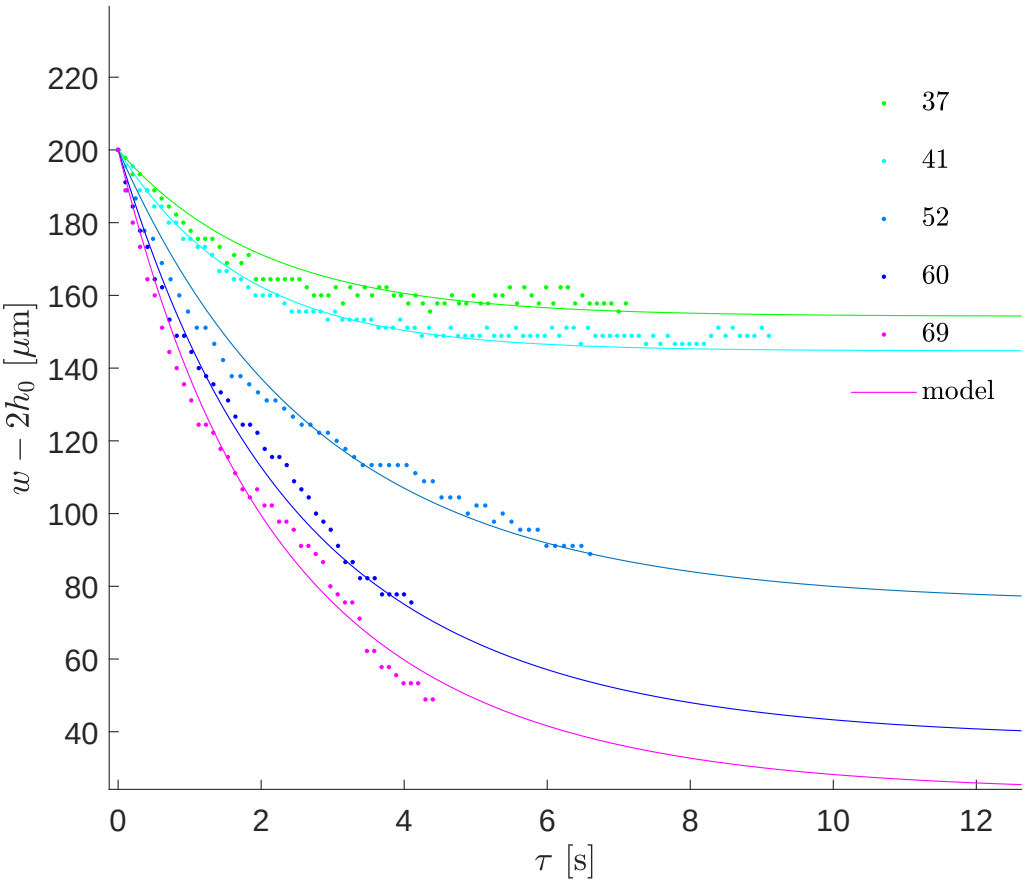

Figure 74: Comparison in between the time evolution of the neck width of a 800 µm long droplet deformed by different temperature increase in a 200 µm and 30 µm wide and high channel. The values of (d_x, d_z) that were implemented in the model to fit the experimental data minimize the error function N.

Viscous dissipation in the system

As described by Cantat [33], the viscous force associated equals to

$$f_{diss} = -\eta \int_{meniscus} \frac{\partial v}{\partial z}(y) dy. \tag{108}$$

The velocity expression and the related viscous force depend on the boundary condition that is set at the droplet interface. In the case of a stress free boundary condition, the viscous force per unit of interface length that is located in the dynamical meniscus and in the lubrication film scales as:

- for an advancing meniscus, $f^a_{diss} = 3.84\gamma C_a^{2/3}$
- for a receding meniscus, $f^r_{diss} = -1.1\gamma C_a^{2/3}$

Droplet relaxation

Late times

Figure 61(a) does not display the interface profile at late times which correspond to the last seconds of the relaxation process for the sake of clarity. However, they are shown on figure 75 that plots that the whole time evolution of $h(x,t)$. We notice that the late times profiles are noisier. This noise is amplified as the profiles are re-scaled for the self-similar analysis. Likely, this noise, comes from the image analysis of the experimental data that relies on the contrast between the inner phase and the outer phase. The quantity of external phase becoming smaller and smaller as the relaxation process ends, we expect the profiles to be harder to detect thanks to our image analysis technique.

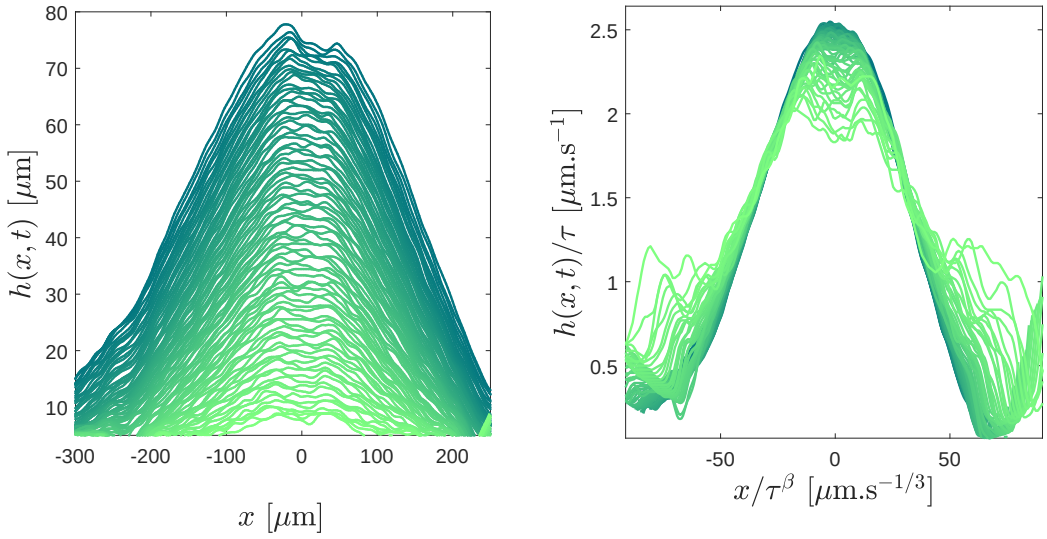

Figure 75: (a) Interface profile $h(x,t)$ at the level of the neck over 11 seconds, the duration of the relaxation process. (b) Self-similar profile of the interface after having rescaled the y-axis by $t_0 - t$ and the x-axis by $(t_0 - t)^{1/3}$.

Calculation of the errorbar on the characteric drainage time

To collapse perfectly the experimental data on a master line in figure 71, we add to adjust the values of w, e, l from the one measured thanks to an image processing by dw, de and dl.

$$\frac{\mathrm{d}\tau}{\tau} = \left(\left(\frac{2\mathrm{dw}}{w} \right)^2 + \left(\frac{2\mathrm{de}}{e} \right)^2 + \left(\frac{\mathrm{dl}}{l} \right)^2 \right)^{1/2} \tag{109}$$

On all the experimental images, the pixel size p is smaller than 5 µm. We do not consider the variation of w and e on a same microfluidic system induced by the microfabrication process. Then, we consider that de is zero and d$w = 2p \sim 10$ µm. The interface between the droplet and the side channel wall on experimental images is difficult to detect with our image processing since the presence of the menisci blurs the interface. This error is maximum on the datasets corresponding to $e = 60$ µm where the meniscus radius is $\frac{e}{2} \sim 30$ µm. Therefore, we can estimate that $dl \sim e$ All these limitations lead to $d\tau/\tau \sim 14\%$ superior to all our experimental data.

References

[1] A. Gurgel, M. C. P. A. Moura, T. N. C. Dantas, E. B. Neto, and A. D. Neto. A review on chemical flooding methods applied in enhanced oil recovery. *Brazilian journal of petroleum and gas*, 2(2), 2008.

[2] M. F. Nazar, S. S. Shah, and M. A. Khosa. Microemulsions in enhanced oil recovery: A review. *Petroleum Science and Technology*, 29(13):1353–1365, 2011.

[3] J. Avendano. Viscoélasticité et récupération assistée du pétrole. *Thesis*, 2012.

[4] A. Muggeridge, A. Cockin, K. Webb, H. Frampton, I. Collins, T. Moulds, and P. Salino. Recovery rates, enhanced oil recovery and technological limits. *Philosophical Transactions of the Royal Society of London A: Mathematical, Physical and Engineering Sciences*, 372(2006), 2014.

[5] P. G. Saffman and G. Taylor. uhdueh. *Proc. R. Soc. Lond.*, 245 (1242)(312–329), 1958.

[6] G. M. Homsy. Viscous fingering in porous media. *Annu. Rev. Fluid Mech.*, 19 (9)(271–311), 1987.

[7] A. Nishimura, A. Schmit, L. Salkin, L. Courbin, and Panizza P. Breakup of confined drops against a micro-obstacle: an analytical model for the drop size distribution. *Microfluidics and Nanofluidics*, 21:94, 05 2017.

[8] M. Jung, M. Brinkmann, R. Seeman, T. Hiller, M. Sanchez de, L. Lama, and S. Herminghaus. Wettability controls slow immiscible displacement through local interfacial instabilities. *Phys. Rev. Fluids*, 1(074202), 2016.

[9] T. T. Al-Housseiny, P. A. Tsai, and H. A. Stone. Control of interfacial instabilities using fow geometry. *Nat. Phys.*, 8 (10)(747–750), 2012.

[10] Keiser L., R. Herbaut, J. Bico, and E Reyssat. Washing wedges: capillary instability in a gradient of confinement. *J. Fluid Mech.*, 790(619–633), 2016.

[11] R. Dangla, S. Kayi, and C. Baroud. Droplet microfluidics driven by gradients of confinement. *Proc. Nat Acad. Sci. USA*, 110 (03)(853-858), 2013.

[12] C. Baroud, F. Gallaire, and R. Dangla. Dynamics of microfluidic droplets. *Lab on a Chip*, 10(2032-2045), 2010.

[13] R. Seeman, M. Brinkmann, T. Pfohl, and S. Herminghaus. Droplet based microfluidics. *Rep. Progr. Phys.*, 75(016601), 2012.

[14] E. Brouzes, M. Medkova, N. Savenelli, D. Marran, M. Twardowski, J. B. Hutchison, J. M. Rothberg, D. R. Link, N. Perrimon, and M. L. Samuels. Droplet microfluidic technology for single-cell high-throughput screening. 106(34):14195–14200, 2009.

[15] M. T. Guo, A. Rotem, J. A. Heyman, and D. A. Weitz. Droplet microfluidics for high-throughput biological assays. *Lab Chip*, 12:2146–2155, 2012.

[16] P. J. Hung, P. J. Lee, P. Sabounchi, R. Lin, and L. P. Lee. Continuous perfusion microfluidic cell culture array for high-throughput cell-based assays. *Biotechnology and Bioengineering*, 89(1):1–8, 2004.

[17] M. Nakano, J. Komatsu, S. Matsuura, K. Takashima, S. Katsura, and A. Mizuno. Single-molecule pcr using water-in-oil emulsion. *Journal of Biotechnology*, page 117–124, 2003.

[18] D.S. Tawfik and A.D. Griffiths. Man-made cell-like compartments for molecular evolution. *Nature biotechnology*, page 16(7):652–6, 1998.

[19] K. R. Oldenburg, J.-H. Zhang, T. Chen, A. Maffia, K. F. Blom, A. P. Combs, and T. D. Chung. Assay miniaturization for ultra-high throughput screening of combinatorial and discrete compound libraries: a 9600-well (0,2 microliter) assay system. *Journal of Biomolecular Screening*, page 3(1):55–62, 1998.

[20] A. D. Griffiths and D. S. Tawfik. Miniaturising the laboratory in emulsion droplets. *Trends in Biotechnology*, page 24(9):395–402, 2006.

[21] X. Jie and A. Daniel. Drop on demand in a microfluidic chip. *Journal of Micromechanics and Microengineering*, 18(6):065020, 2008.

[22] H. Song, D. L. Chen, and R. F. Ismagilov. Reactions in droplets in microfluidic channels. *Angewandte Chemie International Edition*, 45(44), 2006.

[23] H. Gu, M. H. G. Duits, and F. Mugele. Droplets formation and merging in two-phase flow microfluidics. *International Journal of Molecular Sciences*, 12(4):2572–2597, 2011.

[24] K. C. Sung, M. Hyejin, and K. Chang-Jin. Creating, transporting, cutting, and merging liquid droplets by electrowetting-based actuation for digital microfluidic circuits. *Journal of Microelectromechanical Systems*, 12(1):70–80, 2003.

[25] T. Thorsen, S. J. Maerkl, and S. R. Quake. Microfluidic large-scale integration. *Science*, 298(5593):580–584, 2002.

[26] V. Berejnov, N. Djilali, and D. Sinton. Lab-on-chip methodologies for the study of transport in porous media: energy applications. *Lab Chip*, 8:689–693, 2008.

[27] S. R. Hodges, O. E. Jensen, and J. M. Rallison. The motion of a viscous drop through a cylindrical tube. *J. Fluid Mech.*, 501(279-301), 2004.

[28] A. Huerre, O. Théodoly, A. M. Leshansky, M.-P. Valignat, I. Cantat, and M.-C. Jullien. Droplets in microchannels: dynamical properties of the lubrication film. *Phys. Rev. Lett.*, 115(064501), 2015.

[29] B. Reichert, A. Huerre, O. Théodoloy, M.-P. Valignat, I. Cantat, and M.-C. Jullien. Topography of the lubrication film under a pancake droplet travelling in a hele-shaw cell. *J. Fluid Mech.*, 2018.

[30] L. Zhu and F. Gallaire. A pancake droplet translating in a hele-shaw cell: lubrication film and flow field. *Journal of Fluid Mechanics*, 798:955–969, 2016.

[31] J. H. Snoeilher and B. Andreotti. Moving contact lines: scales, regimes, and dynamical transitions. *Annu. Rev. Fluid Mech.*, 45(269–292), 2013.

[32] F. P. Bretherton. The motion of long bubbles in tubes. *J. Fluid Mech.*, 10 (02)(166-188), 1961.

[33] I. Cantat. Liquid meniscus friction on a wet plate: bubbles, lamellae and foams. *Phys. Fluids.*, 25(031303), 2013.

[34] B. Selva, V. Miralles, I. Cantat, and M.-C. Jullien. Thermocapillary actuation by optimized resistor pattern: bubbles and droplets displacing switching and trapping. *Lab Chip*, 10:1835–1840, 2010.

[35] B. Dhananjay and K.-M. Chantal. Hydrophilization and hydrophobic recovery of pdms by oxygen plasma and chemical treatment—an sem investigation. *Sensors and Actuators B: Chemical*, 123(1):368 – 373, 2007.

[36] P.G. de Gennes, F. Brochard-Wyart, and D. Quere. *Gouttes, Perles et Ondes.* 2005.

[37] E. Guyon, J.P. Hulin, and L. Petit. *Hydrodynamique Physique.* 2012.

[38] J. Israechvili. Intermolecular and surface forces. *Intermolecular and Surface Forces, 3rd edn. Elsevier.*, 2011.

[39] M. S. Bakshi. Micelle formation by sodium dodecyl sulfate in water–additive systems. *Bulletin of the Chemical Society of Japan*, 69(10):2723–2729, 1996.

[40] S. Paula, W. Sues, J. Tuchtenhagen, and A. Blume. Thermodynamics of micelle formation as a function of temperature: A high sensitivity titration calorimetry study. *The Journal of Physical Chemistry*, 99(30):11742–11751, 1995.

[41] A. Huerre. *Migration de gouttes en microfluidique: caractérisation et applications.* 2015.

[42] M. Corti and V. Degiorgio. Quasi-elastic light scattering study of intermicellar interactions in aqueous sodium dodecyl sulfate solutions. *The Journal of Physical Chemistry*, 85(6):711–717, 1981.

[43]

[44] V. Miralles, A. Huerre, H. Williams, B. Fournié, and M.-C. Jullien. A versatile technology for droplet-based microfluidics: Thermomechanical actuation. *Lab Chip*, 15, 2015.

[45] R. Dangla. *2D droplet microfluidics driven by confinement gradients*. 2012.

[46] E. Villermaux and B. Bossa. Single-drop fragmentation determines size distribution of raindrops. *Nature Physics*, 5:697–702, 2009.

[47] E. Reyssat. *Gouttes, films et jets: quand les écoulements modèlent les interfaces*. 2007.

[48] B. Selva, I. Cantat, and M.-C. Jullien. Temperature-induced migration of a bubble in a soft microcavity. *Physics of Fluids*, 23(5):052002, 2011.

[49] Adsorption dynamics of surfactants at the air/water interface: a critical review of mathematical models, data, and mechanisms. *Colloids and Surfaces A: Physicochemical and Engineering Aspects*, 100:1 – 45, 1995.

[50] Y. Pawar and K. J. Stebe. Marangoni effects on drop deformation in an extensional flow: The role of surfactant physical chemistry. i. insoluble surfactants. *Physics of Fluids*, 8(7):1738–1751, 1996.

[51] C. Ybert and J.-M. di Meglio. Ascending air bubbles in solutions of surface-active molecules: Influence of desorption kinetics. *The European Physical Journal E*, 3, Oct 2000.

[52] B. Cuenot, J. Magnaudet, and B. Spennato. The effects of slightly soluble surfactants on the flow around a spherical bubble. *Journal of Fluid Mechanics*, 339:25–53, 1997.

[53] V. Miralles, E. Rio, I. Cantat, and M.-C. Jullien. Investigating the role of a poorly soluble surfactant in a thermally driven 2d microfoam. *Soft Matter*, 12:7056–7062, 2016.

[54] A. Manz, C.S. Effenhauser, N. Burggraf, D.J. Harrison, K. Seiler, and K. Fluri. Electroosmotic pumping and electrophoretic separations for miniaturized chemical analysis systems. *Journal of Micromechanics and Microengineering*, 4:257–265, December 1994.

[55] J Padovani, S. S. Jeffrey, and R. T. Howe. Electropermanent magnet actuation for droplet ferromicrofluidics. 4:1–10, 05 2016.

[56] Z. Z. Chong, S. H. Tan, A. M. Ganan-Calvo, S. B. Tor, N. H. Loh, and N.-T. Nguyen. Active droplet generation in microfluidics. *Lab Chip*, 16:35–58, 2016.

[57] R. H. Farahi, A. Passian, T. L. Ferrell, and T. Thundat. Microfluidic manipulation via marangoni forces. *Applied Physics Letters*, 85(18):4237–4239, 2004.

[58] C. N. Baroud, M. Robert de Saint Vincent, and J.-P. Delville. An optical toolbox for total control of droplet microfluidics. *Lab Chip*, 7:1029–1033, 2007.

[59] J. C. McDonald and G. M. Whitesides. Poly(dimethylsiloxane) as a material for fabricating microfluidic devices. *Accounts of Chemical Research*, 35(7):491–499, 2002.

[60] D. C. Duffy, J. C. McDonald, O. J. A. Schueller, and G. M. Whitesides. Rapid prototyping of microfluidic systems in poly(dimethylsiloxane). *Analytical Chemistry*, 70(23):4974–4984, 1998.

[61] Vivek Bakshi. *EUVlithography*. 2007.

[62] A. M. Leshansky, S. Afkhami, M.-C. Jullien, and P. Tabeling. Obstructed breakup of slender drops in a microfluidic t junction. *Phys. Rev. Lett.*, 108:264502, 2012.

[63] A. Huerre, V. Miralles, and M.-C. Jullien. Bubbles and foams in microfluidics. *Soft Matter*, 10:6888–6902, 2014.

[64] F. Becker and L. Zhao-Liang. Surface temperature and emissivity at various scales: Definition, measurement and related problems. *Remote Sensing Reviews*, 12(3-4):225–253, 1995.

[65] Z. Nadolny, G. Dombek, and P. Przybylek. Thermal properties of a mixture of mineral oil and synthetic ester in terms of its application in the transformer. pages 857–860, 2016.

[66] B. Kim, M. Park, Y. S. Kim, and U. Jeong. Thermal expansion and contraction of an elastomer stamp causes position-dependent polymer patterns in capillary force lithography. *ACS Applied Materials and Interfaces*, 3(12):4695–4702, 2011.

[67] K. A. Brown, D. J. Eichelsdoerfer, W. Shim, B. Rasin, B. Radha, X. Liao, A. L. Schmucker, G. Liu, and C. A. Mirkin. A cantilever-free approach to dot-matrix nanoprinting. *Proceedings of the National Academy of Sciences, supp. mat.*, 110(32):12921–12924, 2013.

[68] B. S Hardy, K. Uechi, J. Zhen, and H. Pirouz K. The deformation of flexible pdms microchannels under a pressure driven flow. 9:935–8, 05 2009.

[69] M. Serra, I. Pereiro, A. Yamada, J.-L. Viovy, S. Descroix, and D. Ferraro. A simple and low-cost chip bonding solution for high pressure, high temperature and biological applications. 17:1, 01 2017.

[70] R. Dangla, F. Gallaire, and C. N. Baroud. Microchannel deformations due to solvent-induced pdms swelling. *Lab Chip*, 10:2972–2978, 2010.

[71] J.D. Berry, M.J. Neeson, R.J. Dagastine, D.Y.C. Chan, and R.F. Tabor. Measurement of surface and interfacial tension using pendant drop tensiometry. *Journal of Colloid and Interface Science*, 454:226 – 237, 2015.

[72] P. J. A. Janssen and P. D. Anderson. Boundary-integral method for drop deformation between parallel plates. *Physics of Fluids*, 19(4):043602, 2007.

[73] H. A. Stone and L. G. Leal. Relaxation and breakup of an initially extended drop in an otherwise quiescent fluid. *Journal of Fluid Mechanics*, 198:399–427, 1989.

[74] H.A. Stone. Dynamics of drop deformation and breakup in viscous fluids. *Annual Review of Fluid Mechanics*, 26(1):65–102, 1994.

[75] A. Vananroye, P. Van Puyvelde, and P. Moldenaers. Effect of confinement on droplet breakup in sheared emulsions. *Langmuir*, 22(9):3972–3974, 2006.

[76] C. Ulloa, A. Ahumada, and M. Cordero. Effect of confinement on the deformation of microfluidic drops. *Phys. Rev. E*, 89:033004, Mar 2014.

[77] P. Guillot, A. Colin, and A. Ajdari. Stability of a jet in confined pressure-driven biphasic flows at low reynolds number in various geometries. *Phys. Rev. E*, 78:016307, Jul 2008.

[78] P. Guillot, A. Colin, A. S. Utada, and A. Ajdari. Stability of a jet in confined pressure-driven biphasic flows at low reynolds numbers. *Phys. Rev. Lett.*, 99:104502, Sep 2007.

[79] L. Yuehao, J. Mranal, M. Yongting, and N. Krishnaswamy. Control of the breakup process of viscous droplets by an external electric field inside a microfluidic device. *Soft Matter*, 11:3884–3899, 2015.

[80] M.-C. Jullien, M.-J. Tsang Mui Ching, C. Cohen, L. Menetrier, and P. Tabeling. Droplet breakup in microfluidic t-junctions at small capillary numbers. *Physics of Fluids*, 21(7):072001, 2009.

[81] M. De Menech. Modeling of droplet breakup in a microfluidic t-shaped junction with a phase-field model. *Phys. Rev. E*, 73:031505, 2006.

[82] A. M. Leshansky and L. M. Pismen. Breakup of drops in a microfluidic t junction. *Physics of Fluids*, 21(2):023303, 2009.

[83] D. R. Link, S. L. Anna, D. A. Weitz, and H. A. Stone. Geometrically mediated breakup of drops in microfluidic devices. *Phys. Rev. Lett.*, 92:054503, Feb 2004.

[84] T. Cubaud. Deformation and breakup of high-viscosity droplets with symmetric microfluidic cross flows. *Phys. Rev. E*, 80:026307, Aug 2009.

[85] Dangla R., Fradet E., Lopez Y., and Baroud C. The physical mechanisms of step emulsification. *Journal of Physics D: Applied Physics*, 46(11):114003, 2013.

[86] K.A. Brakke. The surface evolver. *Experimental mathematics*, 1(2):141–165, 1992.

[87] D. Dendukuri, S. S. Gu, D. C. Pregibon, T. A. Hatton, and P. S. Doyle. Stop-flow lithography in a microfluidic device. *Lab Chip*, 7:818–828, 2007.

[88] A. Aradian, E. Raphael, and P.-G. de Gennes. Marginal pinching in soap films. *EPL (Europhysics Letters)*, 55(6):834, 2001.

[89] J.D. McGraw, T. Salez, O. Baumchen, E. Raphael, and K. Dalnoki-Veress. Self-similarity and energy dissipation in stepped polymer films. *Phys. Rev. Lett.*, 109:128303, 2012.

[90] L. Bluteau, M. Bourrel, N. Passade-Boupat, L. Talini, E. Verneuil, and F. Lequeux. Water film squeezed between oil and solid: drainage towards stabilization by disjoining pressure. *Soft Matter*, 13:1384–1395, 2017.

[91] D. YC Chan, E. Klaseboer, and R. Manica. Film drainage and coalescence between deformable drops and bubbles. *Soft Matter*, 7(6):2235–2264, 2011.

[92] P Brun, M. Nagel, and F. Gallaire. 043009. *Phys.Rev.E*, page 88, 2013.

[93] P. Oswald and G. Poy. Droplet relaxation in hele-shaw geometry: Application to the measurement of the nematic-isotropic surface tension. *Phys. Rev. E*, 92:062512, Dec 2015.

[94] G.I. Barenblatt. *Scaling*. Cambridge University Press, 2003.

[95] J. Eggers and M. Fontelos. The role of self-similarity in singularities of partial differential equations. *Nonlinearity*, 22:R1, 2009.

[96] T.S. Chan, S. Srivastava, A. Marchand, B. Andreotti, L. Biferale, F. Toschi, and J.H. Snoeijer. Hydrodynamics of air entrainment by moving contact lines. *Journal of Fluid Mechanics*, 305:322, 1997.

[97] A. Oron, S.H. Davis, and S.G. Bankoff. Long-scale evolution of thin liquid films. *Reviews of Modern Physics*, 69:981, 1997.

[98] W. Boos and A. Thess. Thermocapillary flow in a hele-shaw cell. *Journal of Fluid Mechanics*, 352:305, 1997.

[99] H.C. Brinkman. A calculation of the viscous force exerted by a flowing fluid on a dense swarm of particles. *Applied Science Research*, 1:27, 1949.

[100] F. Viola, P.-T. Brun, B. Dollet, and F. Gallaire. Foam on troubled water: Capillary induced finite-time arrest of sloshing waves. *Physics Of Fluids*, 28(9):7. 091701, 2016.

[101] J. M. Rallison. The deformation of small viscous drops and bubbles in shear flows. *Annual Reviews of Fluid Mechanics*, 16:45, 1984.

[102] C. Josserand and S.T. Thorodssen. Drop impact on a solid surface. *Annu. Rev. Fluid Mech.*, 48:365, 2016.

[103] D. Richard, C. Clanet, and D. Quéré. Contact time of a bouncing drop.

[104] L. Xu, W. W. Zhang, and S. R. Nagel. Drop splashing on a dry smooth surface. *Physical Review Letters*, 94:184505, 2005.

[105] Jolet de Ruiter, Rudy Lagraauw, Dirk van den Ende, and Frieder Mugele. Wettability-independent bouncing on flat surfaces mediated by thin air films. *Nature Physics*, 11:48–53, 2014.

[106] V. Miralles. Migration of biphasic systems by thermal actuation in microconfinement. *thesis*, 2015.

Résumé

Cette thèse porte sur l'étude expérimentale de la déformation et de la relaxation d'une goutte, confinée dans un canal microscopique de section rectangulaire. Cette goutte est initialement déformée en forme de cacahuète grâce à un gradient de confinement induit de façon locale et réversible dans le canal. Lorsque que le gradient de confinement est désactivé, la goutte relaxe vers sa forme d'équilibre. Durant cette phase de relaxation, le liquide contenu dans le réservoir, formé au niveau de la déformation de la goutte, draine vers les extrémités de la goutte. Dans notre étude, la géométrie du système est complexe et ne présente pas d'axe de symétrie ni d'invariance. Pour décrire la dynamique de la déformation et de la relaxation de la goutte, les modèles classiques, qui reposent sur une approximation 2D de la goutte, ne peuvent pas être invoqués. Cependant, des lois d'échelles nous permettent de décrire la dynamique de la goutte. Elles mettent en évidence la contribution significative des ménisques à la dissipation visqueuse dans le système.

Mots-clés

Microfluidique digitale, gouttes, gradient de confinement, relaxation, auto-similarité

Abstract

We report an experimental study concerning the capillary deformation and relaxation of a relatively long droplet confined to a microscopic channel with rectangular cross-section. These droplets, found in numerous microfluidic applications, are centrally pinched into a peanut-like shape thanks to a localized, reversible deformation of the channel.
After the channel deformation is released, the droplet relaxes back to its plug-like shape minimizing its surface energy under the constraints imposed by the channel walls. During this relaxation, the liquid contained in the central neck drains towards the extremities of the droplet.
Classical models incorporating capillary driving with viscous dissipation employing geometrical invariance, whether translation or rotation cannot describe the deformation and relaxation in such intrinsically 3-dimensional geometries. By considering the 3D problem, scaling models incorporating dominant dissipation within the droplet menisci allows a full recovery of the droplet deformation and relaxation dynamics.

Keywords

Droplet-based microfluidics, droplet, confinement gradient, relaxation, self-similarity